Residual stress measurement in engineering materials and structures using neutron diffraction.

Thesis

UNRESTRICTED

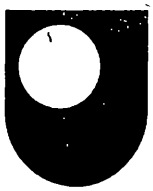

The Open University

Faculty of Technology

Department of Materials Engineering

RESIDUAL STRESS MEASUREMENT IN ENGINEERING MATERIALS AND STRUCTURES USING NEUTRON DIFFRACTION

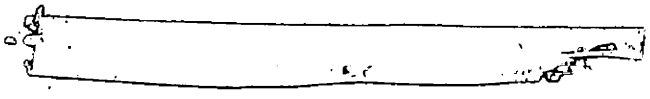

DATE OF SUBMISSION: 10 DECEMBER 1999
DATE OF AWARD: 12 JANUARY 2000

Monojit Dutta

December 1999

A thesis submitted in partial fulfilment of the requirements of the degree of Doctor of Philosophy

Monojit Dutta
The Open University

Ph. D. Thesis
December, 1999

Residual Stress Measurement in Engineering Materials and Structures using Neutron Diffraction

ABSTRACT

This thesis presents the determination and analysis of residual stresses, both at the macrolevel and microlevel, in different engineering materials using the neutron diffraction technique.

The macrostress studied is that produced by welding in stainless steel pipes used in power plants. The objective was to see the effect of a part-thickness repair weld on the pre-existing residual stress field generated from the original weld. The strain values were measured in the three principal directions through the pipe thickness both in the original and repair weld areas and the full stress tensors were calculated. The results show the presence of a large tensile hoop stress in the outer half thickness in and around the original weld with a peak value just below the last weld cap pass. The measured through-thickness stresses show an impressive agreement with finite element predictions. A sharp rise in the axial stress in the heat affected zone is produced by the repair treatment, particularly below the repair depth. The presence of a highly tensile axial membrane stress (~175 MPa) in the repaired area compared to a compressive one (–55 MPa) in the original weld region suggests that an overall bending has been caused in the pipe by the repair work. The through-thickness radial stress is always low with values close to zero in both the original and repair welds.

The microstress investigated is that created between the constituent phases of an Al-SiC_p metal matrix composite. This study can be divided into two parts. The effect of plasticity on the fatigue crack-tip stresses, particularly the microlevel misfit stresses has been studied in the first part. All the macro and micro stress components were separated from the total stress measured by neutron diffraction in a plastically deformed and fatigue cracked specimen, both unloaded and elastically loaded conditions and they were compared with those in an undeformed and cracked specimen. 1% plastic deformation has been found to reduce the misfit stresses to almost zero in both phases. No effect of fatigue cracking and elastic loading on misfit stresses has been observed in this study. In the second part of the study, changes in microstresses in bent specimens caused by different heat treatments have been investigated. A plastic deformation of about 0.33% has reduced the misfit stress by ~35% in both phases, which is regenerated by heat treatment. The amount of regeneration depends mainly on the treatment temperature and also time. A sub-zero treatment in liquid nitrogen however, has not made any significant change in the stress states in this study.

ACKNOWLEDGEMENTS

I would like to express my sincere gratitude to my supervisors, Dr Michael Fitzpatrick and Dr Lyndon Edwards for their encouragement, help and advice. Their continual support and prompt response during the writing of this dissertation enabled me to complete this work in just over three years.

I must acknowledge British Energy for the provision of the welded components used in this study and thank Dr P. J. Bouchard of British Energy for sharing his knowledge about welding and allowing me to present some of their finite element results for comparisons. Thanks are due to Dr Mark Daymond and John Wright at ISIS, Dr Ru Lin Peng at NFL, Studsvik and Dr Thilo Pirling at ILL, Grenoble for their help with the neutron experiments. I would also like to acknowledge Prof. Hans Georg Priesmeyer at GKSS, Germany.

I would like to thank all the members of the Fracture Research Group at the Department of Materials Engineering of The Open University, particularly Jim Moffatt and Peter Ledgard for the technical support, Dr Javier Santisteban and Dr Ahmed Bouzina for their warm friendship and occasional academic advice. Particular thanks are due to Dr Giovanni Bruno, an ex-member of this group (presently at HMI, Germany) for his assistance in experiments, valuable comments, many helpful discussions and above-all a true friendship. I am also grateful to all my friends who have given me, from far and near, a morale boost during my hard times.

I would like to acknowledge my employer, The Tata Iron and Steel Co. Ltd, India for the approval of the study leave which helped me accomplish my endeavour for the higher degree abroad.

Finally, my deepest thanks and regards go to my parents, brothers and all other family members and to my wife, Ronita. It is their invaluable love, support and encouragement that has enabled me to overcome all hurdles I have faced throughout the past three years. I entirely dedicate this thesis to them.

Monojit Dutta

December, 1999

PREFACE

This thesis is submitted for the degree of Doctor of Philosophy of The Open University. The work described in this dissertation was carried out in the Department of Materials Engineering of the Faculty of Technology, between December, 1996 and November, 1999, under the supervision of Dr M. E. Fitzpatrick and Dr L. Edwards. It is an original work of the author except where reference is made to the work of others. None of this work has been submitted, or is in the process of being submitted in whole or part for a degree at any other university. Some of the results of this work have been published in academic journal and conference proceedings as listed below:

1. M. Dutta, G. Bruno, L. Edwards and M. E. Fitzpatrick, *Internal Stress Changes Measured by Neutron Diffraction in a Metal Matrix Composite After Mechanical and Thermal Treatments*, in Proc. Sixth International Conference on Composite Engineering (ICCE/6), ed. D. Hui, Florida, USA, 1999, pp. 195-196.

2. L. Edwards, M. Dutta, M. E. Fitzpatrick, P. J. Bouchard, *Direct Measurement of Residual Stresses at a Repair Weld in an Austenitic Steel Tube*, in Proc. International Conference on Integrity of High-Temperature Welds, The Inst. of Mech. Engineers, 1998, pp. 181-191.

3. M. E. Fitzpatrick, M. Dutta and L. Edwards, *Determination by Neutron Diffraction of Effect of Plasticity on Crack Tip Strains in a Metal Matrix Composite*, Materials Science and Technology, Vol. 14, 1998, pp. 980-986.

4. M. E. Fitzpatrick, M. Dutta and L. Edwards, *Effect of Previous Plastic Deformation on Stresses after Fatigue on a Metal Matrix Composite*, in Proc. MAT-TEC 97, sub. ed. A. Lodini, IITT International, 1997, pp. 281-286.

5. L. Edwards, G. Bruno, M. Dutta, P. J. Bouchard, K. L. Abbott, R. L. Peng, *Validation of Residual Stress Predictions for a 19 mm Thick J Preparation Manual Metal Arc Stainless Steel Pipe Girth Weld using Neutron Diffraction*, accepted for oral presentation and to be published in Proc. Sixth International Conference on Residual Stresses (ICRS-6), Oxford, UK.

NOMENCLATURE

σ	general symbol for stress (Pa)
$\sigma_x(z)$	stress variation along the direction z; the subscript indicates the principal stress axis along which the stress is acting
σ_i^{Tot}	total stress (consisting of macro and micro stresses) in the i^{th} phase at a point of the composite specimen; $i=m$ for the matrix and $i=r$ for the reinforcement
σ^{Macro}	applied or residual macrostress at a point of the specimen
σ_i^{EM}	elastic mismatch stress in the i^{th} phase at a point of the composite specimen arising from the unequal distribution of the macrostress owing to the mismatch in elastic properties between the phases
σ_i^{SM}	shape misfit stress in the i^{th} phase at a point of the composite specimen arising from the shape misfits between the phases owing to the difference in coefficients of thermal expansion, and plastic deformation
ε	general symbol for strain with subscripts and superscripts used as for stress; dimensionless
λ	wavelength of neutrons (Å)
ν	Poisson's ratio; dimensionless
θ	Bragg scattering angle (degree)
a	lattice parameter (Å)
d	interplanar spacing (Å)
d_0	strain-free interplanar spacing (Å)
E	elastic modulus (Pa)

TABLE OF CONTENTS

CHAPTER 1: INTRODUCTION

1.1 INTRODUCTION

It is well established that practically no engineering materials or structures can be manufactured free of residual stresses. Residual stress can be generated in materials from any kind of thermal, mechanical or chemical treatment or a combination of them during manufacture. For the safe and reliable design of any engineering component or structure, these residual stresses must be considered since the service life may be greatly altered by the presence of such stresses.

The detrimental effects of residual stress can either be covered by a large safety factor in material selection and design, which may sometimes be too expensive to be a viable solution, or be minimised by a post-fabrication mechanical, thermal or thermo-mechanical treatment (*e.g.* shot peening, heat treatment etc.) of components; or they should be dealt with by regular and careful checking of the components combined with proper remedial action. Sometimes residual stresses are deliberately introduced into a component (*e.g.* shot peening, cold expansion of fastener holes) to exploit the beneficial effect of residual stress for improved service life. So, the prevention of the deleterious effects and an intelligent application of the beneficial effects of residual stress is always a challenge for materials engineers and scientists. For such a challenge, a thorough knowledge about the cause and effect of residual stress on the performance of all constituent materials is required. Although this area has been studied for decades, there is always a lack of reliable residual stress data. Some of the reasons for this are: (i) dependence of residual stress on fabrication parameters and process variables, (ii) development of new materials *e.g.* various alloys, metal and ceramic matrix composites etc. and (iii) limitations of measurement techniques.

Measurement of residual stress by a reliable technique and its analysis is therefore very important for any study, for example, the fatigue behaviour of an engineering component.

Out of the existing stress measurement techniques, which will be briefly discussed later in this Chapter, the neutron diffraction technique has emerged to be the only non-destructive method for measuring internal stresses deep within a material. The details of this relatively new technique will be given in the next Chapter. Based on the distance over which they act in a component, residual stresses can be divided into macrolevel residual stresses and microlevel residual stresses, as described in the next section. In this project, the neutron diffraction technique has been utilised to determine residual stresses at both the macrolevel and the microlevel. The macrostress investigated is that produced by welding. In particular, changes in the residual stress distribution with a stainless steel pipe butt weld due to the introduction of a short, part-thickness repair weld have been studied. The microstress investigated is that created between the constituent phases of a metal matrix composite (MMC) material. In particular, changes in microlevel stresses in both the matrix and the reinforcement phases around a fatigue crack tip, caused by a plastic deformation, and also changes in microstresses in bent MMC specimens caused by different heat treatments have been studied.

1.2 DIFFERENT TYPES OF RESIDUAL STRESS

1.2.1 Macrolevel Residual Stress

The overall residual stresses in any material can be categorised in terms of macrolevel and microlevel residual stresses, based on the distance over which they act. If they vary over a large area of the material, over several millimetres or even centimetres on a spatial scale, they are termed macrolevel residual stresses or type I residual stress [1]. Many of the thermal and mechanical sources *e.g.* welding, heat treatment, plastic bending, shot peening etc., as mentioned in Table 1.1, which cause relative deformation of different areas of the material, are sources of such macrostresses. Type I macrostresses are homogeneous over several grains and are equilibrated over the whole body.

1.2.2 Microlevel Residual Stress

Microlevel residual stresses vary over a much smaller scale (microscopic and sub-microscopic areas) than macro stresses. When these stresses are nearly homogeneous across one grain or less, or over the inter-particle spacing in a composite material [2] they are described as residual stress of type II and are equilibrated over a number of grains. They are caused by a mismatch in material properties *e.g.* mismatch in the coefficients of thermal expansion (CTE) or elastic modulus between different phases; anisotropy in plastic flow between different phases or even between different grains of the same phase. These microstresses are also termed as "pseudo-macrostresses" [3] since they can be detected by some strain measurement techniques such as X-ray diffraction, but remain undetected by sectioning techniques, such as hole drilling, because they sum to zero over any appreciable volume of the material. Another type of microlevel residual stress, which is inhomogeneous across submicroscopic areas *e.g.* several atomic distances within the grains, is classified as residual stress of type III. These microstresses come from lattice imperfections such as dislocations, inclusions etc. The overall stress field that exists at any point of the material is the sum of the macro and micro level stresses as shown in figure 1.1 [4].

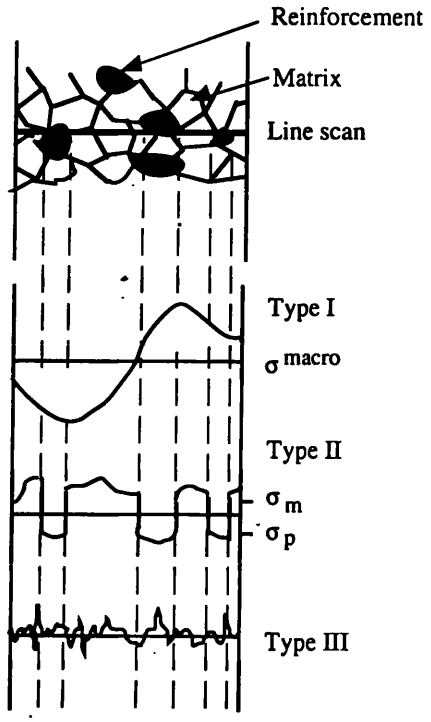

Figure 1.1: Variation in macro and micro stresses in a metal matrix composite [4].

1.3 ORIGIN OF RESIDUAL STRESS

Residual stress can be generated in a component almost at every step of its manufacture, starting from material synthesis to final fabrication. Most of the origins may be generalised as mechanical or thermal or a combination of two. In addition, anisotropy in yield strengths or difference in CTE between grains of different phases may be the main reason for microlevel residual stress development in composite materials. The common sources of residual stress in materials are tabulated in Table 1.1.

Type	Source
Thermal	• Joining *e.g.* welding, brazing, soldering etc. • Heat treatment *e.g.* quenching, surface hardening, phase transformation • casting
Mechanical	• Machining *e.g.* grinding, drilling, turning etc. • Forming *e.g.* rolling, forging, drawing, pressing, shot peening etc. • Loading *e.g.* tension, compression, bending, torsion etc.
Chemical	• Hydrogen diffusion
Material	• Anisotropy in yield strength • Multiphase material • Defects

Table 1.1: Common sources of residual stress in materials.

In this project, residual stresses from two such sources have been analysed: the most common thermal cause *i.e.* weld residual stress in an austenitic stainless steel pipe and a combination of mechanical (loading) and thermal (heat treatment) causes in an MMC. Welding is a complex phenomenon in terms of residual stress generation. Shrinkage and quenching effects after the intense local heating involved with a multipass weld are mainly

responsible for residual stress generation. The experimental details and the results of the macrolevel weld residual stresses are presented in Chapter 4.

During the study of microlevel residual stress in a 2124 Al matrix reinforced with SiC particles, the specimens were solution treated at 505°C followed by a quench in cold water, and then plastically deformed under tension and bending. Some were again heat treated at different temperatures. So there are various possible sources of residual stress in the specimens. First of all, the yield stress in a 2124 Al decreases sharply with an increase in temperature [5]. During quenching from 505°C the surface layer is first to cool and contract; the central part is still at high temperature and can accommodate this surface contraction by plastic flow. On subsequent cooling the centre also starts contracting; but cannot relax completely because of the cold and stiff surface. This leaves the surface in compression and the centre in tension. The CTEs and the yield strengths are also different between the two phases (Al alloy and SiC). The difference in these material properties between the phases causes microlevel residual stress in the specimens. In addition, plastic deformation *e.g.* stretching and bending generates both the macrolevel and the microlevel residual stresses in the specimens, which will be discussed in the next Chapter. Various heat treatments could then alter these stresses to different amount. Experimental results obtained from the MMC for both the macro and micro scale residual stresses are presented in Chapter 5.

1.4 STRESS MEASUREMENT TECHNIQUES

A number of techniques are available to determine the stress state in a component and most rely on the measurement of strain. Depending on the necessity of the component to be reusable after strain measurement, the techniques are classified as destructive or non-destructive.

1.4.1 Destructive Techniques

The main basis of these techniques is to measure the macrostrain released after incremental removal of stressed material from the component by various mechanical or etching treatments, or to measure the shape changes due to cutting of stressed material. Destructive methods can detect only the macrostress, as the microstresses equilibrate to zero over any appreciable volume of material, [3]. Some advantages of these mechanical methods are their simple applicability, low cost and fast results. Some of these destructive techniques are briefly described below.

Hole drilling is a widely used method, proposed more than six decades ago [6]. A hole to a depth of 1.5 times its diameter is drilled [7] and the strain relaxation is measured by three strain gauges in a rosette, placed around the hole. The increment of hole depth mainly depends on the accuracy of the cutting tool and stresses can be measured from a minimum depth, equal to the hole diameter [8] to a maximum of about eight millimetres [9].

Ring coring [10] is a similar method where annular slots, instead of holes, are cut around a strain gauge fixed on the surface. The residual stress distribution on and beneath the surface can be calculated from the measured values. General limitations for both hole drilling and ring core techniques are [8]: (i) areas of high stress gradients should be avoided since the stress gradient is assumed to be constant across the hole or core diameter; (ii) the thickness of the test specimen must be at least four times the hole or core diameter; (iii) results with stresses greater than one-third the yield strength of the material may be erroneous due to the generation of local plastic strain during metal removal; (iv) the space between two holes or cores must be at least eight times their diameter.

The **Sachs boring** technique [11] is also based on the same principle of measuring the relaxed strain after removal of concentric layers of material. An axial hole is drilled first and the strain is measured for every incremental increase of hole diameter with the help of a pair of strain gauges fixed at the surface. The difficulty of determination of stresses near the outer surface by this technique is overcome by turning off the outer diameter and the strain

relaxation can be measured by strain gauges fixed at the inner surface of the hollow tube as suggested by Bühler [12]. It is strictly applicable only to specimens possessing cylindrical symmetry.

A fast but approximate idea about the residual stress along any particular direction at the surface of the component is given by the **deflection** method. This involves mechanical slitting of the specimen and measurement of the consequent deflection of the slit element.

1.4.2 Non-Destructive Techniques

Non-destructive techniques are based on the measurement of either the lattice strain distribution (in X-ray and neutron diffraction techniques) or the effects on some distinct physical properties of the material (in Moiré fringe, ultrasonic and magnetic methods). Some of these non-destructive techniques are briefly discussed below.

Moiré interferometry is an optical method which makes use of two grids of high density (or closely spaced) lines. One grid is fixed on a transparent plate whereas the other is placed on the surface of the specimen and suffers a distortion due to residual stress along with the specimen. Fringe patterns are formed when the distorted grid is superimposed on the undistorted grid either directly or with the help of a camera. The strain can be calculated from the knowledge of line density (1200 lines/mm in a routine practice [13]) and distance between pairs of fringes or directly from the fringe inclination with the co-ordinate axes. This technique measures the surface strains only.

Ultrasonic techniques can give information about the macrostress in the near surface region and also in the interior of the component. These techniques are based on the acoustoelastic effect by which the speed of sound waves (v) is influenced approximately linearly by the internal stresses (σ) within the material as described by the following relation.

$$v = v_0 + K\sigma \qquad \text{(Equation 1.1)}$$

where v_0 is the wave speed in unstressed material and K is the acousto-elastic constant which is a material property. A longitudinal wave travels faster in most materials under compression than under tension and the acoustic constant is negative. Sources other than the stress-induced elastic strain, that influence the velocity of sound wave, should be identified first and very precise measurements of time and path lengths are necessary because the shift in velocity is only about 0.1% [14]. A sound wave from less than one to several megahertz is induced into the material and the stress value can finally be obtained from a knowledge of time of flight or some other velocity related parameter. Some advantages of this technique are that the instrument is less expensive, portable, radiation-free and quick to set up. But the competing effects of other material characteristics such as grain size, texture, dislocation density and temperature on ultrasound wave propagation, as well as a low spatial resolution and the necessity for very precise time measurements are the negative points.

Magnetic methods of stress determination are based on the solid state property that the magnetic hysteresis curve in a ferrous material changes its size under the influence of any stress field. Many stress sensitive parameters of macromagnetic (hysteresis in the set-up techniques, eddy current etc.) and micromagnetic (magnetic Barkhausen, acoustic Barkhausen, reversible or incremental permeability, dynamic magnetostriction etc.) natures have been derived from this property to measure stresses in ferrous materials. Based on the published literature, between 1976 and 1996, it has been observed that the most frequently (~75%) investigated micromagnetic techniques are derived from Barkhausen signal parameters [15]. This is concerned with measuring the number and magnitude of abrupt magnetic reorientations made by the magnetic domains and observed as pulses of random amplitude and duration [8]. The advantage of this method is its ability to separate out the effect of residual stress from other superimposing factors like microstructural or texture effects by using different magnetic parameters that are sensitive to either stress, microstructure or texture. But the condition that the material must be ferromagnetic limits its applicability.

Diffraction techniques can be applied only to crystalline materials. When such a material is under stress, applied or residual, a change in its interplanar atomic spacing is caused by the resulting elastic strain. This interplanar spacing is used as an "atomic" strain gauge by both X-ray and neutron diffraction techniques. Usually a monochromatic beam (white beam in spallation neutron sources) having a wavelength similar in magnitude to the atomic spacing is incident on the material (generally polycrystalline) under study. Scattering occurs from different families of crystallographic planes. The interplanar atomic spacing of suitably oriented planes can be calculated from the Bragg reflection. Any shift in the Bragg peak from a particular plane *(h k l)* in the spectra between a strained and an unstrained material gives the elastic strain. The engineering stress values can be obtained from these strains if the crystallographic elastic constants of the material are known. There is an electromagnetic interaction between X-rays and the electron cloud around the atoms of a material and they are highly absorbed after penetrating up to 100 microns in most materials. Conventional X-ray diffraction is therefore limited to near-surface measurements. On the other hand, the flight of uncharged neutrons is affected primarily by nuclear collisions; but not by the electron cloud. This results in higher penetrability of neutrons, up to few centimetres in most materials (as can be seen in table 1.2 [16]); so that bulk strain measurement is possible by neutron diffraction.

	Fe	Ni	Ti	Al
Neutrons	5.8 mm	3.9 mm	13.9 mm	69.3 mm
X-rays	10.9 μm	8.2 μm	82 μm	136 μm

Table 1.2: Penetration distances in common engineering materials for 50% absorption of neutrons and X-rays [16].

However, limited source, high cost, comparatively low speed and difficulties in near surface strain measurement with neutrons encourages the use of X-rays, wherever possible. Therefore, X-ray and neutron diffraction techniques of stress analysis should not be considered as competing, but complementary to each other [17]. Furthermore, the

development of synchrotron X-ray sources can provide high energy beams with much increased penetration in light materials. However, the low wavelengths may lead to small scattering angles in most metals; so full stress tensor measurements are still difficult to make. A more detailed description of the neutron diffraction technique is given in the next Chapter.

1.5 REFERENCES

1. E. Macherauch and K. H. Kloos, *Origin, Measurement and Evaluation of Residual Stresses*, in Proc. Residual Stress in Science and Technology, eds. E. Macherauch and V. Hauk, DGM Informationsgesellschaft, 1987, Verlag, Germany, pp. 3-26.

2. R. J. Arsenault and M. Taya, *Thermal Residual Stress in Metal Matrix Composite*, Acta Metall., 35 (3), 1987, pp. 651-659.

3. B. D. Cullity, *Some Problems in X-ray Stress Measurements*, Adv. in X-ray Anal., 20, 1977, pp. 259-271.

4. M. E. Fitzpatrick, M. T. Hutchings and P. J. Withers, *Separation of Macroscopic, Elastic Mismatch and Thermal Expansion Misfit Stresses in Metal Matrix Quenched Plates from Neutron Diffraction Measurements*, Acta Mater., 45 (12), 1997, pp. 4867-4876.

5. *Metals Handbook*, 10th edn., ASM International, 1990.

6. J. Mathar, *Determination of Initial Stresses by Measuring the Deformation Around Drilled Holes*, Arch. Eisenhuttenwesen, 6, 1934, pp. 277-281 and Trans. ASME, 56 (4), 1934, pp. 249-254.

7. A. Nikulari, J. Lu, J. F. Flavenot, *Measurement of Residual Stress Distribution by the Incremental Hole Drilling Method*, J. of Mech. Working Tech., 11(2), 1985, pp. 167-188.

8. C. O. Rudd, *A Review of Nondestructive Methods for Residual Stress Measurement*, J. of Metals, 33 (7), 1981, pp. 35-40.

9. V. Hauk, *Structural and Residual Stress Analysis by Nondestructive Methods*, Elsevier (Amsterdam), 1997, p. 15.

10. H. Wolf, W. Böhm, Arch. Eisenhüttenwes, 42, 1971, p. 175.

11. V. G. Sachs, Zeitschrift für Metalkunde, 19, 1927, p. 352.

12. H. Bühler, Zeitschrift für Metalkunde, 19, 1952, p. 388.

13. Z. Wu, J. Lu and P. Joulaud, *Study of Residual Stress Distribution by Moiré interferometry Incremental Hole Drilling Method*, in Proc. Fifth International Conference on Residual Stresses (ICRS-5), eds. T. Ericsson, M. Odén and A. Andersson, Linköping University, Sweden, pp. 804-808.

14. R. B. Thompson, *An overview of Ultrasonic Measurement Techniques*, in Proc. of the Fourth International Conference on Residual Stresses (ICRS 4), Baltimore, MA, Society for Experimental Mechanics, 1994, pp. 97-111.

15. W. A. Thüner, *Micromagnetic Techniques*, in ref. 9, pp. 97-111.

16. M. E. Fitzpatrick, Ph. D. Thesis, Dept. of Materials Science and Metallurgy, University of Cambridge, 1995.

17. L. Pintschovius, *Neutrons Versus X-rays*, in Measurement of Residual and Applied Stress Using Neutron Diffraction, eds. M. T. Hutchings and A. D. Krawitz, Kluwer Academic, London, 1992, pp. 577-580.

CHAPTER 2: STRESS MEASUREMENT BY NEUTRON DIFFRACTION

2.1 INTRODUCTION

There has long been a demand from design and production engineers for a suitable probe or technique for measuring the magnitude of residual stresses deep inside engineering components. Such a technique would help them estimate the maximum loading and service life for critical components. The neutron diffraction technique for stress measurement is perhaps the closest answer to the engineers' prayer [1]. The technique was first developed at Harwell, UK, at the beginning of the 1980's [2] with parallel work elsewhere, which strengthened the feasibility of the technique to measure bulk stresses in different materials *e.g.* aluminium [3, 4], zircaloy [5] and steel [6]. Over the years, many more neutron sources have been made available throughout the world for research purposes and the technique is now considered to be one of the most powerful and useful techniques due to its following advantages over conventional strain measurement techniques:

- it is a non-destructive technique applicable to most crystalline materials;
- it can generate subsurface (up to 50 mm) information which cannot be obtained by other non-destructive methods;
- since this technique does not disturb the stress state within the specimen during measurement, complicated data corrections are not required;
- the strain in each component of a composite material can be measured simultaneously;
- it can provide accurate experimental data to validate finite element models.

This Chapter describes different types of neutron sources and the principle of stress measurement by this technique - from neutron scattering to separation of different stress components.

2.2 SUITABILITY OF NEUTRONS FOR STRAIN MEASUREMENT

Neutrons are chargeless subatomic particles having wave properties and virtually the same mass as protons. According to the principles of strain measurement by diffraction, which will be discussed in detail in the following section, strain values are calculated from the distortion of the crystalline solid due to any residual or applied load. To determine such a change in atomic arrangement, it is necessary for the neutrons to have a wavelength of the same order as the interatomic distances.

From the wave-particle duality of neutrons, the equivalent wavelength λ of a neutron of mass m and velocity v can be obtained from the equation

$$\lambda = \frac{h}{m\mathrm{v}} \qquad \text{(Equation 2.1)}$$

where h is Planck's constant. Neutrons generated by either fission reactions or spallation are very fast and so are allowed to make numerous collisions with light atoms in a moderator such as heavy water, liquid methane or graphite, where they lose energy and come to thermal equilibrium with the moderator. The kinetic energy of such thermalised neutrons is given by

$$\frac{1}{2}m\mathrm{v}^2 = \frac{3}{2}kT_m \qquad \text{(Equation 2.2)}$$

where k is Boltzmann's constant and T_m is the moderator temperature. For the value of T_m within a range of a few hundred degrees Kelvin, the moderated neutron energies are in the range of millielectron volts (meV) [7]. The wavelength of a neutron beam can be determined by combining equations 2.1 and 2.2

$$\lambda = \frac{h}{\sqrt{3mkT_m}} \qquad \text{(Equation 2.3)}$$

For a moderator temperature of a few hundred degrees Kelvin, the wavelength of the moderated neutrons is around 1Å, which is fortunately just the magnitude desired in diffraction studies of crystalline solids.

2.3 NEUTRON SOURCES

There are two types of sources for the production of high intensity neutron beams: reactor sources, and the accelerator based spallation sources. Since the first installation of a neutron spectrometer at the Argonne National Laboratory in the USA in 1945, several other spectrometers were commissioned within a decade in different parts of the world, and over the years, nuclear reactors have been the major source of neutrons for scientific research [8]. In reactors, neutrons are generated by fission of uranium nuclei. A more recent development in high intensity neutrons is the spallation source where high energy protons (600 - 1000 MeV) are bombarded into heavy nuclei of tungsten, uranium, tantalum etc. to generate neutrons. Reactor and spallation sources will be discussed in the next two sections with specific details of the sources which were used for this work: NFL at Studsvik, Sweden and ILL, Grenoble, France as reactor sources and ISIS at Didcot, UK as a spallation source.

2.3.1 Reactor Sources

Neutrons from fission reactors are of high intensity, in the order of 10^{14}-10^{15} neutrons $cm^{-2}s^{-1}$ and are too energetic to be used in diffraction studies. So they are slowed down by passing them through a moderator, made of light elements such as light water, heavy water, graphite, liquid methane etc. They lose energy after a number of collisions with light atoms to come to an equilibrium with the moderator temperature and thus the wavelength distribution of the neutrons is altered. These thermalised white neutrons are then transmitted to the monochromator usually via a guide tube using total internal reflection. The guide tubes are made of borated glass with a nickel coating inside and have sometimes a slight curvature to remove any fast neutrons, X-rays or γ-rays from the beam that reach the sample. From these polychromatic or white neutrons in the guide, a single wavelength must be separated out for strain measurement, which is done by a monochromator, placed at an angle with the beam in the neutron guide. Monochromators are single crystals of a suitable material, *e.g.* graphite or germanium, and scatter neutrons with a particular wavelength

satisfying the condition for Bragg diffraction, out of the guide tube to the spectrometer proper. Different wavelengths can be selected by fixing the monochromator crystal at different angles with the neutron beam in the guide tube. A typical diagram of a spectrometer layout at a reactor neutron source is shown in figure 2.1.

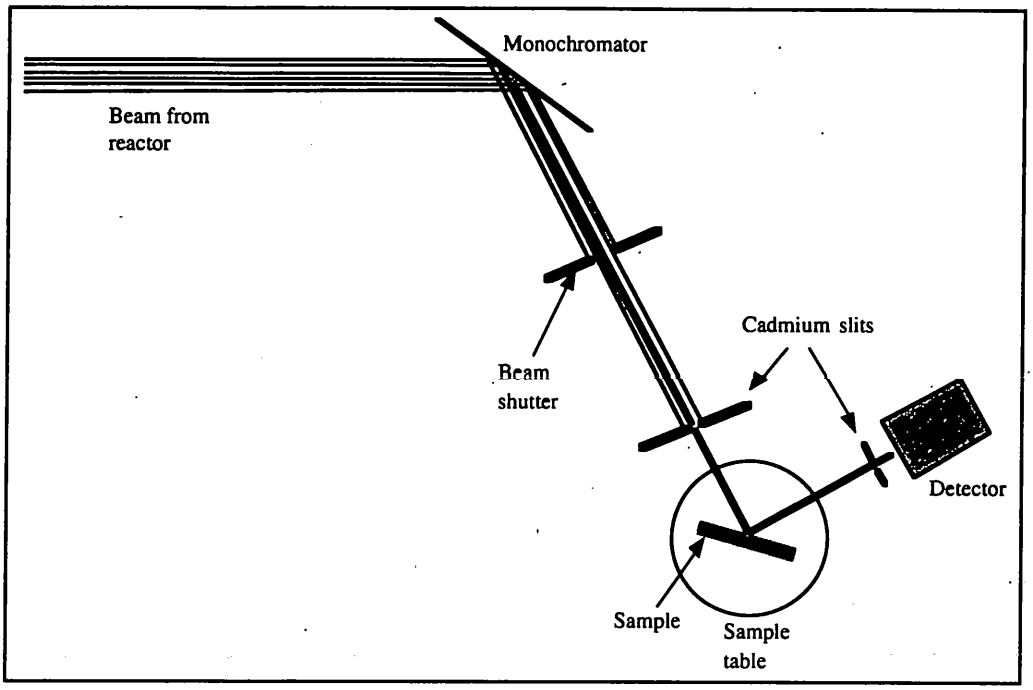

Figure 2.1: Schematic diagram of the spectrometer arrangement at a reactor source.

The monochromated neutron beam passes through a beam shutter which can be operated to close the beam when required. Beam shutters are made of strong neutron absorbing materials, such as resin-bound boron carbide (B_4C). The beam is then collimated in the incident beam guide to reduce its angular spread and passed through cadmium slits to restrict its dimension. The specimen is mounted on a sample table which, in modern spectrometers, has motor-driven and often programmable movements in x (longitudinal), y (transverse), z (vertical) and θ (rotational) directions. This is very important for accuracy and reproducibility of the sampling position. Generally, the diffracted beam is also passed through a collimator and/or slit. The slits on the incident and diffracted beam path define the gauge volume of the specimen to be examined, as will be explained in section 2.4.

Some specific details about the reactors and the spectrometers at ILL, Grenoble, France and NFL, Studsvik, Sweden which were used in this work are given in Table 2.1. Experimental set up will be discussed for individual sets of experiments in later Chapters.

Parameters	**ILL, Grenoble**	**NFL, Studsvik**
Thermal power, MW	58.4	50
Thermal flux in beam tube, $nm^{-2}s^{-1}$	1.2×10^{19}	2.4×10^{18}
Moderator	Heavy water	Water
Monochromator	30 Ge crystals	Double focusing Si (331)
Take-off angle	122°	84°-90°
Wavelength, Å	1.390 - 2.994	1.66 – 1.76
Flux at sample, n cm^{-2} s^{-1}	2×10^{6}	1.3×10^{6}
Beam size, mm^2	20 x 30	30 x 40
Resolution	FWHM at 2θ 0.50° 30° 0.41° 60° 0.32° 90° 0.33° 120° 0.97° 150°	FWHM = 0.18° at 90° (measured with silicon powder)
Angular range	$6°<2\theta<160°$ $0°<\omega<360°$	$-140°<2\theta<140°$
Detector	25 ^{3}He counters at 5 atm and a 2D PSD with 128 elements	100 mm Ordela ^{3}He PSD

Table 2.1: Some specific details of the reactors and spectrometers at ILL, Grenoble and NFL, Studsvik.

2.3.2 Spallation Sources

One of the main problems in conventional fission reactors is the generation of intense (tens of MW) heat within the reactor core. In spallation sources where heat generation is not a problem, diffraction data can be obtained very fast with simultaneous generation of many peaks in the same spectrum. Neutrons are produced here in a different manner, by bombarding high energy particles from a powerful accelerator on a heavy metal target. Many experiments in this work were carried out at one well known spallation source *i.e.* ISIS facility of the Rutherford Appleton Laboratory, UK.

At ISIS, negatively charged hydrogen ions are produced first in an ion source and they are accelerated up to 70 MeV in several steps. Protons are then produced in the synchrotron by passing these high energy H^- ions through a very thin (0.3 μm) alumina foil. In the synchrotron protons make approximately 10,000 revolutions and are accelerated to 800 MeV before they are diverted and fired fifty times a second, towards a target which is made from a heavy metal such as tantalum. After bombardment with high energy protons, about 15 neutrons are generated from the target metal by each proton. Neutrons produced in this process generally have high energy and they are slowed down, like at reactor sources, by passing through a moderator. The spectral distribution of neutrons is determined by the moderator temperature, which is adjusted for different types of experiments. Various options for moderators such as water at ambient temperature (316 K), liquid methane (100 K) and liquid hydrogen (20 K) exist at ISIS; generally liquid methane is used. A schematic diagram of the ENGIN spectrometer is shown in figure 2.2 in the next page.

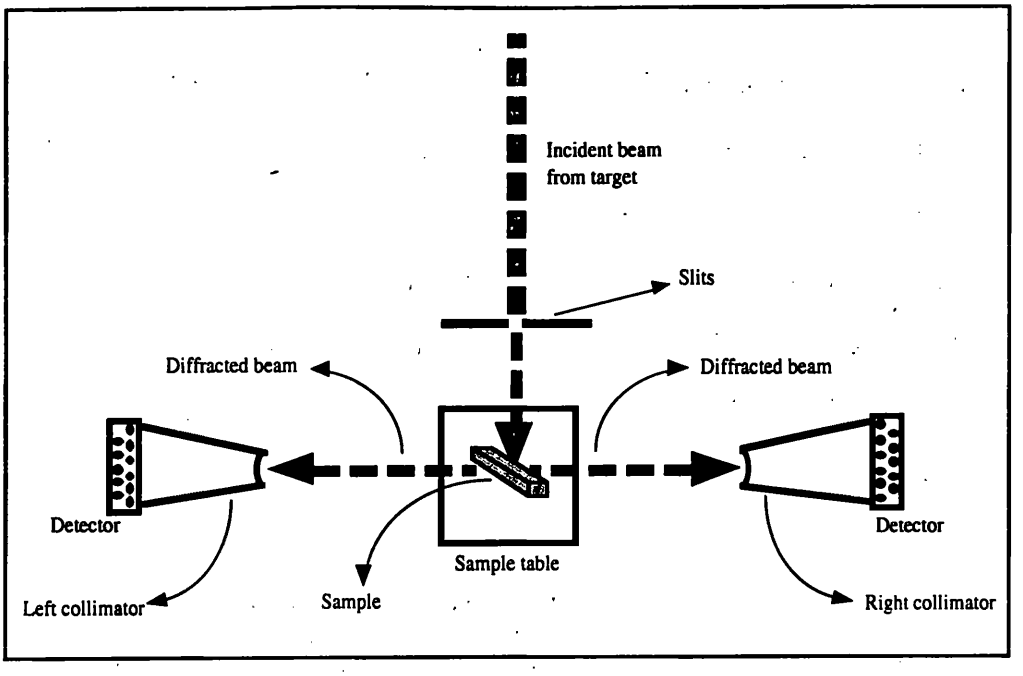

Figure 2.2: Schematic diagram of the ENGIN spectrometer at ISIS, Rutherford Appleton Laboratory, UK.

The incident beam collimation is provided by a pair of orthogonally mounted slits made from sintered boron carbide (B_4C). A wide range of square or rectangular beam sizes is possible by a combination of two such slits of various dimensions (0.5, 1, 1.5, 2, 3, 4, 5, 10 and 25 mm wide, each 30 mm long). The sample positioner is motorised and programmable for its x, y, z or θ movements and can hold samples up to 250 kg in weight. The use of two large radial collimators, together with their associated detector banks each centred at a scattering angle (2θ) of $\pm 90°$, makes it possible to measure strain in two perpendicular directions simultaneously. The radial collimators are made from gadolinium oxide coated mylar. Detector banks cover an angular range of $81.4° < 2\theta < 98.6°$ on each side of the incident neutron beam. Each detector element therefore collects neutrons from a slightly different scattering angle. The focusing routine that adds together the data from individual detectors, accounts for the slight difference in path length for each detector compared to the precise scattering angle of 90°. Detector banks have three horizontal rows each having 45 elements, giving 135 elements per bank. Thus there are 270 detectors altogether for the two banks [9]. The neutrons in each pulse from the moderator have a band of energy and so a band of wavelengths which is about 0.1 to 4 Å. Neutrons with the

highest energy (or velocity) will take the smallest time to arrive at the sample and subsequently after scattering, at the detector, followed by those with progressively less energy (or velocity). A number of diffraction peaks are thus generated from the planes satisfying the Bragg's law (to be discussed in section 2.5) in the above mentioned range of wavelengths, with a decreasing order of Miller indices for each phase. A typical spectrum from the composite studied at ISIS is shown in figure 2.3 which shows all useful peaks for both phases with a fit to the aluminium peaks.

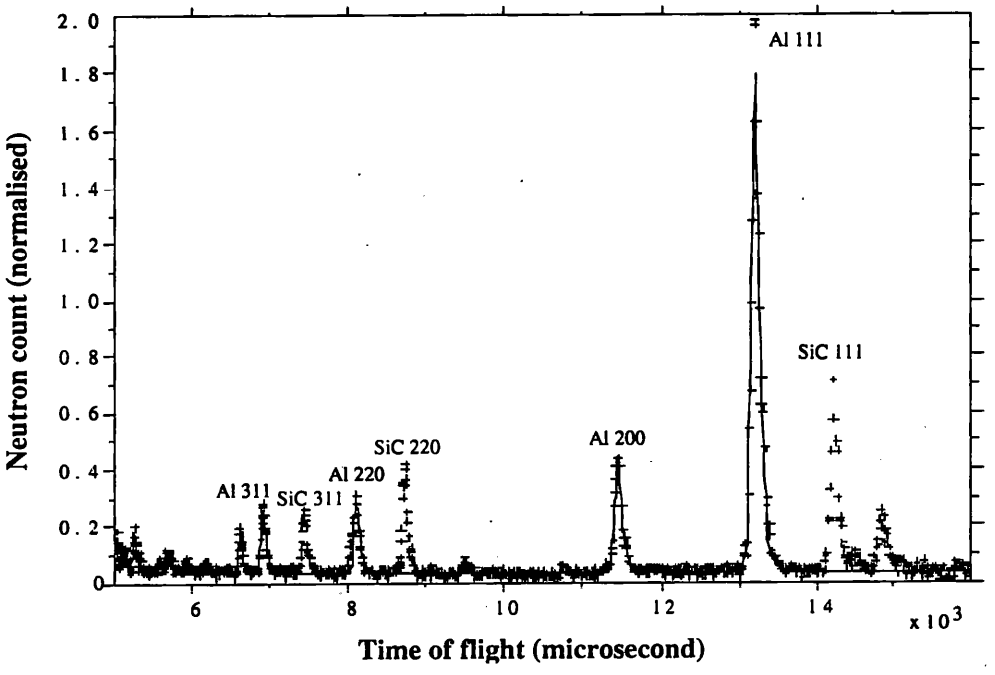

Figure 2.3: Time-of-flight neutron diffraction spectrum obtained from the composite material at ISIS, UK, showing a modified Pawley fit to the aluminium peaks.

The ability of a spallation source to generate many peaks simultaneously, even for different phases, is one of the prime advantages over a reactor source. To determine the lattice parameter, either a single peak is analysed or more often, all the peaks of a particular phase are considered in an advanced fitting technique such as the Rietveld method [10].

2.4 GAUGE VOLUME DEFINITION

The gauge volume or measurement volume is an important factor in neutron strain measurements. This may be defined by the intersection of the incident neutron beam and the volume viewed by the detector. For better accuracy of the measured strain values, the gauge volume should be as small as possible within the specimen, particularly for those having a high stress gradient. This is obtained by the proper selection of neutron masks or slits on the incident beam and also on the diffracted beam where no collimator is used in front of the detector (*e.g.* in NFL, Studsvik), as shown in figure 2.4 and in figure 2.5 where a collimator is used (*e.g.* ILL, Grenoble or ISIS, Didcot).

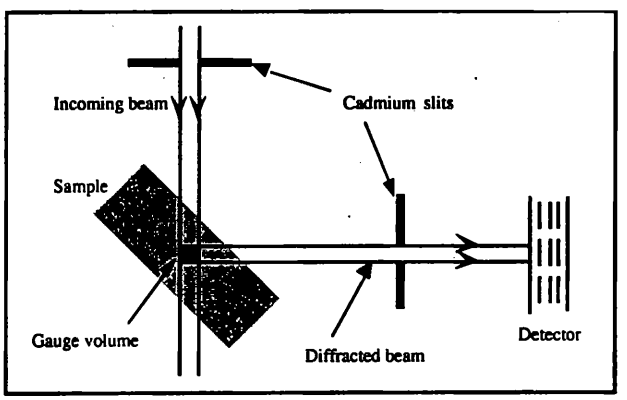

Figure 2.4: Small gauge produced by slits in incident and diffracted beams.

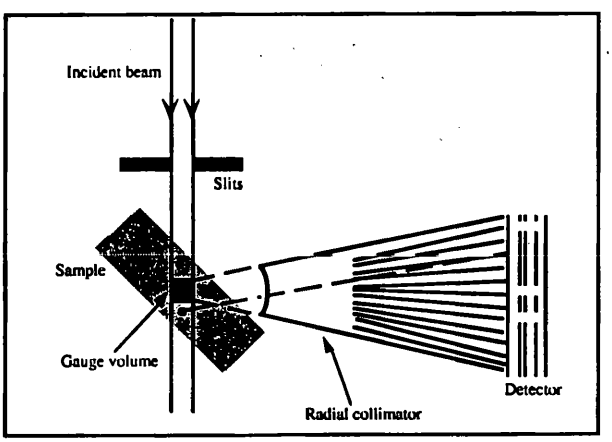

Figure 2.5: Small gauge volume produced by a combination of slits and collimator.

The best definition of gauge volume is obtained at a scattering angle of 90°. As mentioned earlier, the internal structure of radial collimators is made up from sheets of neutron

absorbing materials. This arrangement does not allow the transmission of any diffracted neutron that is within the incident beam line but outside the focusing area of the collimator, by absorbing it within the collimator, as illustrated in figure 2.5. At the D1A spectrometer of ILL, the collimator is 450 mm long and has 22 channels, each having an input aperture of 0.42 mm and the gauge volume can be defined with a variable depth of focus (along the beam) between 0.5 and 1.1 mm by installing different slit masks in between the collimator and the detector [11]. On the other hand, at the ENGIN spectrometer of ISIS, both collimators have 40 vanes with an input area of 46 mm wide by 60 mm high and a detector face area of 230 mm by 300 mm [9]. This collects scattered neutrons from a distance of about 1.6 mm along the beam direction. So if primary slits of 2 mm width and 3 mm height are used for the incoming beam, the gauge volume will be $2 \times 3 \times 1.6\ mm^3$ for the ENGIN spectrometer and $2 \times 3 \times 1.1\ mm^3$ at the D1A if no mask is used in between the collimator and the detector.

Though it is convenient to consider the gauge volume as a perfect cuboid with sharp edges, this is rarely true in reality. Considering a collimation system as a simple combination of two slits as shown in the diagram (figure 2.6), a significant number of neutrons apart from the central region (dark shaded) can reach the detector from the penumbra (shaded) surrounding the central region [9].

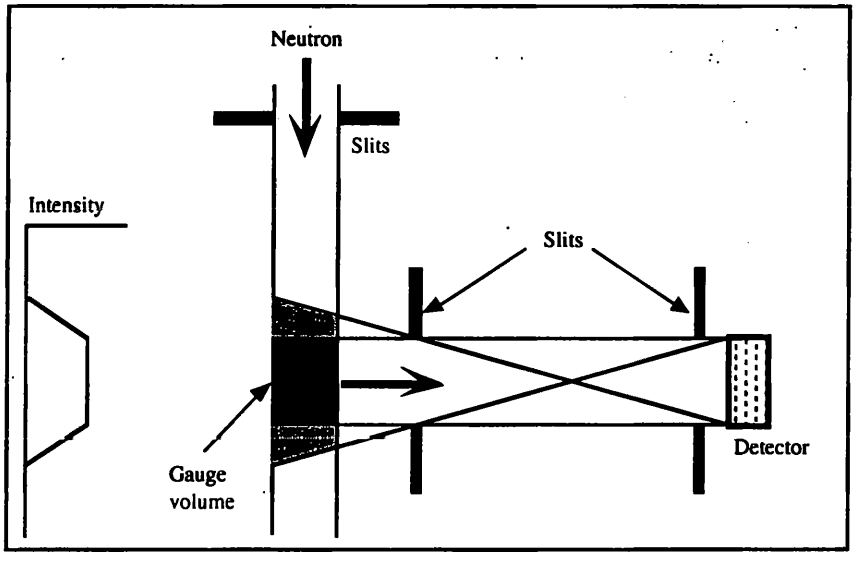

Figure 2.6: Deviation from a cuboidal gauge volume with the formation of regions of penumbra (shaded area) [9].

This makes a three dimensional function for the collection efficiency of collimation and detection, termed the spatial resolution, which depends on the specimen shape, position and material and is not an instrumental constant. This is very important, particularly when near-surface strain measurement is carried out.

2.5 PRINCIPLE OF STRAIN MEASUREMENT BY NEUTRON DIFFRACTION

The basic principle of strain measurement by neutron diffraction is similar to that by conventional X-ray diffraction, which is based on Bragg's law of diffraction. During scattering of neutrons or any other wave by a set of atomic planes in a crystalline solid (as shown in figure 2.7), there is a great deal of interference among the similarly scattered waves. Diffraction or constructive interference occurs only when the path difference of identical diffracted waves is an integral multiple of wavelengths, so that the waves are in phase.

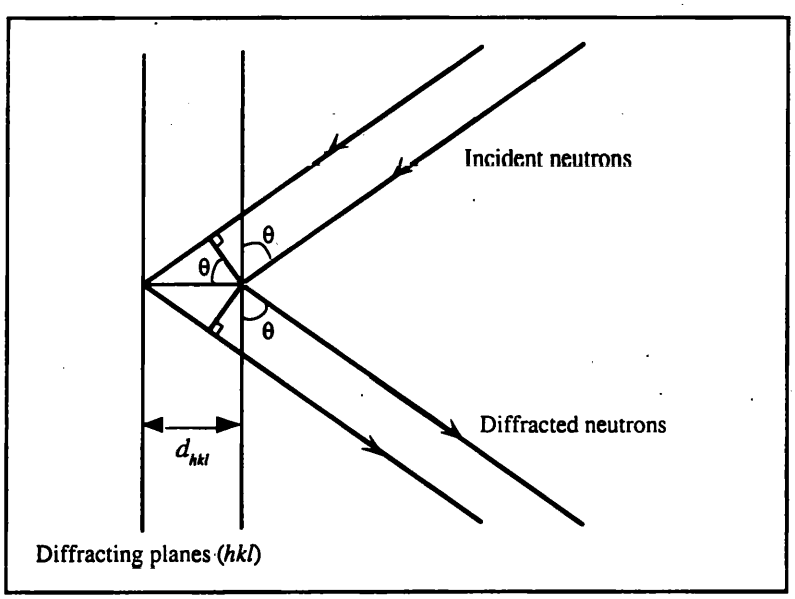

Figure 2.7: Diffraction of two neutron waves from a set of planes with Miller Indices ($h\,k\,l$) with an interplanar distance d. The path difference between the waves is $2\,d\sin\theta$.

As shown in figure 2.7, the total path difference between the two diffracted neutron waves is $2d_{hkl}\sin\theta$; so the condition for diffraction is described here by the equation which is known as Bragg's law:

$$n\lambda = 2d_{hkl}\sin\theta \qquad \text{(Equation 2.4)}$$

where n is an integer (n=1 for the first order reflection), λ is the wavelength, d_{hkl} is the lattice plane spacing for the Bragg reflection ($h\,k\,l$) and 2θ is the scattering angle. It can be stated that λ, d and θ must have values to yield an integral value for n, in order to observe a diffraction peak. The lattice spacing is altered by any elastic strain acting on the material: a tensile stress will increase the spacing along the direction of the stress whereas a compressive stress will reduce it. For a constant wavelength λ in the Bragg equation (equation 2.4), this means a tensile stress will decrease the scattering angle 2θ, whereas a compressive stress will increase it from a value of unstrained specimen. This shift in diffraction peak, which may be ~1°, is large enough to be detected.

By differentiating Bragg's equation for a constant wavelength λ:

$$0 = 2d\cos\theta\,\Delta\theta + 2\sin\theta\,\Delta d \qquad \text{(Equation 2.5)}$$

and by rearranging equation 2.5:

$$\frac{\Delta d}{d_0} = -\cot\theta_0\Delta\theta \qquad \text{(Equation 2.6)}$$

where d_0 and θ_0 stand for the lattice spacing and scattering angle respectively, for the ($h\,k\,l$) planes of the unstrained material. The left side of equation 2.6 is simply the strain which can thus be determined from the shift in scattering angle.

In a spectrometer at a spallation source, pulsed neutron beams having a range of wavelengths, incident on the specimen. The detectors are at a fixed scattering angle and the scattered neutrons reach the detectors as a function of their time-of-flight for each pulse; this is related to the neutron velocity v which is given by:

$$v = \frac{L}{t} \qquad \text{(Equation 2.7)}$$

where L is the flight path length of neutrons *i.e.* the distance from neutron source to the detector and t is time-of-flight. From wave-particle duality of neutrons (equation 2.1) this velocity is equivalent to $\frac{h}{m\lambda}$. The time-of-flight is therefore inversely proportional to neutron velocity and directly proportional to the wavelength. According to Bragg's law, the detector receives the scattered neutrons from a set of lattice planes with particular wavelengths in that range that satisfy equation 2.4. Since the scattering angle is fixed, any change in lattice spacing due to a residual or applied load, will require a wavelength slightly different from the one required for an unstrained material, to satisfy Bragg's law. This slight shift in wavelength will be reflected in the time-of-flight for which a peak is detected. The strain can easily be determined from this change, since the lattice spacing can be calculated if the flight path length is known accurately. The expression may be obtained by combining equations 2.1, 2.4 and 2.7:

$$d_{hkl} = \frac{ht}{2mL\sin\theta} \qquad \text{(Equation 2.8)}$$

Thus the strain ε in time-of-flight measurement can be expressed as:

$$\varepsilon = \frac{\Delta d_{hkl}}{d_0} = \frac{\Delta \lambda_{hkl}}{\lambda_0} = \frac{\Delta t_{hkl}}{t_0} \qquad \text{(Equation 2.9)}$$

2.6 CONVERTING STRAIN TO STRESS

If a component is subject to a multiaxial stress state, the total strain in any direction is given by the sum of all strains resulting from all normal and shear stresses. For an isotropic material, this can be written in a compact form:

$$\varepsilon_{ij} = \frac{1+\nu}{E}\sigma_{ij} - \delta_{ij}\frac{\nu}{E}\sigma_{kk} \qquad \text{(Equation 2.10)}$$

where k is a dummy suffix summing over all k (*i.e.* $\sigma_{kk} = \sigma_{11} + \sigma_{22} + \sigma_{33}$) and δ_{ij} is Kronecker's delta function, which is defined as:

$$\delta_{ij} = \begin{cases} 1, & i = j \\ 0, & i \neq j \end{cases}$$

For i = j = 1, equation 2.10 for a tri-axial stress state becomes:

$$\varepsilon_{11} = \frac{1+\nu}{E}\sigma_{11} - \frac{\nu}{E}(\sigma_{11} + \sigma_{22} + \sigma_{33}) \qquad \text{(Equation 2.11)}$$

The stress values can be expressed in terms of strains by inverting equation 2.10 and summing for i = j = 1, 2 and 3

$$\sigma_{11} + \sigma_{22} + \sigma_{33} = \frac{E}{(1-2\nu)}(\varepsilon_{11} + \varepsilon_{22} + \varepsilon_{33}) \qquad \text{(Equation 2.12)}$$

By substituting any two stresses in terms of ε_{ij} from equation 2.11 or similar to that in equation 2.12, the third stress can be obtained. This can be written in general form as

$$\sigma_{ij} = \frac{E}{(1+\nu)}\varepsilon_{ij} + \frac{\nu E}{(1+\nu)(1-2\nu)}\delta_{ij}\varepsilon_{kk} \qquad \text{(Equation 2.13)}$$

where δ_{ij} and k are same as in equation 2.10.

In most cases, the principal strain directions within a specimen are known from the specimen geometry and/or the loading geometry. It is therefore possible to determine the mean phase principal stresses from three measured principal strains. It has been shown that the strain calculated from a Rietveld refinement is a good approximation to the engineering strain in the component and is not significantly affected by either elastic or plastic anisotropy present in the material [12, 13].

2.7 STRESS COMPONENTS AND THEIR SEPARATION

As mentioned in Chapter 1, residual stresses in a component may be comprised of macrostresses arising from any mechanical or/and thermally induced load, and microlevel stresses (commonly found in a two phase or multiphase material) generated from any anisotropy in the material; for example, due to a difference in CTE or elastic modulus between phases or from lattice imperfections such as dislocations, inclusions etc. The macrostress is the same in both phases in a two phase material and microstresses in any phase at a point are the difference between the total stress at that point and the macrostress value. For a proper understanding about the behaviour and performance of a component, a detailed knowledge about both macrolevel and microlevel residual stresses is required and

this is possible by separating them from the total stress that is measured by diffraction techniques. A detailed study on microlevel residual stresses has been done in this work on a two phase material, an Al alloy matrix reinforced with SiC particles. Various components of residual stress that exist in such a metal matrix composite and the separation technique that was used in this study are discussed in the following section.

2.7.1 Stress Components in an MMC

Stresses are almost never uniformly distributed in a composite material due to its inhomogeneous nature. This gives rise to the formation of macro and micro stresses within the material. The macroscopic stress field or the type I stress as mentioned in Chapter 1, which may be thermally induced or mechanically applied, varies smoothly over the composite and at any point it is same in both phases. In the MMC studied here, the elastic modulus (E) is six times more for the reinforcement than the matrix (~450 GPa for SiC and 72 GPa for Al) whereas the CTE is almost five times less (~4.5 x 10^{-6} K^{-1} for SiC and 23.4 x 10^{-6} K^{-1} for Al) [14, 15, 16]. Any macrostress, applied or residual, will therefore be distributed unevenly with a higher share to the stiffer reinforcement generating elastic mismatch microstresses in the composite.

A commonly found type II stress found in the MMCs is the shape misfit stress. As the name suggests, shape misfit stresses are generated from any unequal shape changes between the phases. The main source of this is the unequal contraction during cooling from a high temperature. On cooling from the processing temperature of the composite or after a quench as carried out in this study, the difference in CTE will produce a net tensile stress in the Al matrix and a net compressive stress in the SiC reinforcement; the matrix is constrained from relaxing completely to its stress-free condition by the reinforcement which has a lower CTE. This part of the shape misfit stress is better known as the thermal misfit stress. However, another part of the shape misfit stress, the plastic misfit term, arising from any plastic deformation must be added [17]. During any small plastic deformation, such as pre-straining or stretching, only the matrix deforms plastically because of its much

lower yield strength compared to the brittle reinforcement. On relaxation of the external tensile load, the matrix contracts less than the reinforcement and goes into compression; whereas a remnant tensile stress still exists in the reinforcement. Therefore the plastic misfit stresses in Al and SiC caused by a tensile plastic loading are of opposite natures to thermal misfit stresses generated by cooling.

2.7.2 Separation of Stress Components

A typical gauge volume used in neutron diffraction measurements is many times the reinforcement spacing in the composite and so it is almost impossible to obtain point-to-point variation in microstresses from such a measurement. These microstresses do not sum to zero in individual phases and therefore contribute to the shift in the Bragg peak and hence, to the average strains measured in each phase. However, they balance to zero when both phases are considered over any appreciable volume such as the gauge volume. Any stress obtained by using equation 2.13 from the measured total average principal strains at a point in a composite by diffraction techniques, is thus comprised of mainly three contributions: the macrostress σ^{Macro}, which is same in both phases and could be measured directly by any destructive mechanical method; the elastic mismatch stress σ^{EM}, due to the difference in elastic stiffness between phases, which is proportional to the macrostress; and the shape misfit contribution σ^{SM} which is independent of any applied load. Thus the average total stress σ_x^{Tot} in any particular direction x, calculated from the measured principal strains can be written for the matrix (m) and the reinforcement (r) as:

$$\sigma_{x,m}^{Tot} = \sigma_x^{Macro} + \sigma_{x,m}^{EM} + \sigma_{x,m}^{SM} \qquad \text{(Equation 2.14)}$$

and

$$\sigma_{x,r}^{Tot} = \sigma_x^{Macro} + \sigma_{x,r}^{EM} + \sigma_{x,r}^{SM} \qquad \text{(Equation 2.15)}$$

Several authors have discussed such stress components and their separation techniques; such as Hauk with other references in [18], Noyan [19], Winholtz [20] and Fitzpatrick *et al.* [21]. But most of them have dealt with the separation between macrostress and overall microstresses. A technique for the separation of all the components used in equations 2.14

and 2.15, has been described by Fitzpatrick *et al.* [21]. The same technique has been used in this study to separate out the microstress components of the residual stress in MMCs and it is interesting to note the effect of different mechanical loading and heat treatment on the misfit stresses, which will be illustrated in Chapter 5. This technique is an extension of the traditional method [19] of separating macrostress and microstress with the application of an Eshelby based model to distinguish between the elastic mismatch stresses and shape misfit contributions.

In diffraction measurements, as mentioned earlier, the sampling volume is generally much more than the spacing between particles in an MMC. The equilibrium conditions of the overall microstresses over any appreciable volume in the composite, *e.g.* the sampling volume gives:

$$f\sigma_{x,r}^{EM} + (1-f)\sigma_{x,m}^{EM} = 0 \qquad \text{(Equation 2.16)}$$

and

$$f\sigma_{x,r}^{SM} + (1-f)\sigma_{x,m}^{SM} = 0 \qquad \text{(Equation 2.17)}$$

where f is the volume fraction of the reinforcement phase in the MMC.

Now, as indicated by Noyan and Cohen [22], the macrostress can be calculated by multiplying equation 2.14 by (1-f) and equation 2.15 by f and then summing them using the relations in equations 2.16 and 2.17:

$$\sigma_x^{Macro} = f\sigma_{x,r}^{Tot} + (1-f)\sigma_{x,m}^{Tot} \qquad \text{(Equation 2.18)}$$

Due to the mismatch in elastic modulus between the phases, this macrostress is redistributed unevenly, more to the stiffer reinforcement and a lesser amount to the compliant matrix. This is counted by the elastic mismatch term which depends on the macroscopic stress and can be expressed as [21]:

$$\sigma_m^{EM} = \beta_m \sigma^{Macro} \qquad \text{(Equation 2.19)}$$

for the matrix, and

$$\sigma_r^{EM} = \beta_r \sigma^{Macro} \qquad \text{(Equation 2.20)}$$

for the reinforcement where β is a tensor accounting for the unequal partitioning of the macrostress and depends on the reinforcement shape (mainly the aspect ratio), volume fraction (f) and the elastic constants of two phases. The appropriate values of β for the matrix and the reinforcement can be calculated using a model such as Eshelby's equivalent homogeneous inclusion approach [16, 23].

For the composites examined in this study, the SiC particles have a low aspect ratio and no preferred orientation and so they are assumed to be spherical. For the MMC with 17 vol.% SiC, this gives the values of β_{xx} to be –0.10 for the matrix and 0.487 for the reinforcement, for a uniaxial load along the x-direction; and β_{xy} equal to 0.0265 for the matrix and –0.129 for the reinforcement, for a uniaxial load along the y-direction where y is perpendicular to x [21]. For the MMC with 22 vol.% SiC, these values are –0.125 and 0.443 respectively for β_{xx} and 0.0326 and –0.115 respectively for β_{xy}.

Once these elastic mismatch components are known, the shape misfit stress components σ_x^{SM} can be calculated simply by subtracting σ_x^{Macro} and σ_x^{EM} from the measured total stress σ_x^{Tot}. In Chapter 5, the results *i.e.*, the separated stress components will be discussed in detail.

2.8 REFERENCES

1. M. T. Hutchings, *Neutron Diffraction Measurement of Residual Stress Fields - the Answer to the Engineers' Prayer ?*, Nondestr. Test Eval., 5, 1990, pp. 395-413.

2. A. J. Allen, C. Andreani, M. T. Hutchings and C. G. Windsor, *Measurement of Internal Stress Within Bulk Materials Using Neutron Diffraction*, NDT Int., 14, 1981, p. 249.

3. M. J. Schmank and A. D. Krawitz, *Measurement of a Stress Gradient Through the Bulk of an Aluminium Alloy Using Neutrons*, Metall. Trans.-A, 13 (1982), pp. 1069-1076.

4. A. D. Krawitz, J. E. Brune and M. J. Schmank, in *Residual Stress and Stress Relaxation*, eds. E. Kula and V. Weiss, 1982, Plenum Press, New York and London, p. 139.

5. S. R. MacEwen, J. Faber Jr and A. P. L. Turner, *The Use of Time-of-Flight Neutron Diffraction to Study Grain Interaction Stresses*, Acta Metall., 31 (5), 1983, pp. 657-676.

6. L. Pintschovius, V. Jung, E. Macherauch and O. Vöhringer, *Residual Stress Measurements by Means of Neutron Diffraction*, Mater. Sci. Engng., 61, 1983, pp. 43-50.

7. I. C. Noyan, J. B. Cohen, *Residual Stress – Measurement by Diffraction and Interpretation*, Springer-Verlag, 1987, p. 111.

8. G. E. Bacon, *Neutron Diffraction*, 2nd edn., Oxford University Press, 1962.

9. *The Precise Measurement of Internal Stress Within Materials Using Pulsed Neutrons*, PREMIS, Final Technical Report, RAL-TR-96-068, Rutherford Appleton Laboratory, UK.

10. H. M. Rietveld, *A Profile Refinement Method for Nuclear and Magnetic Structures*, J. Appl. Cryst., 2, 1969, pp. 65-71.

11. T. Pirling and R. C. Wimpory, *Stress Measurement on D1A: A New High Precision Strain-Scanner*, ILL Annual Report 97, (1998), pp. 87-89.

12. D. Q. Wang, Ph. D. Thesis, Dept. of Materials Engineering, The Open University, 1996.

13. M. R. Daymond, M. A. M. Bourke, R. B. Von Dreele, B. Clausen and T. Lorentzen, *Use of Rietveld Refinement for Elastic Macrostrain Determination and for Evaluation of Plastic Strain History from Diffraction Spectra*, J. Appl. Phys., 82 (4), 1997, pp. 1554-1562.

14. *Engineered Materials Handbook, Vol. 4: Ceramics and Glasses*, ASM International, 1991.

15. *Metals Handbook*, 10th edn., ASM International, 1990.

16. T. W. Clyne and P. J. Withers, *An Introduction to Metal Matrix Composites*, Cambridge Solid State Science Series, Cambridge University Press, 1993.

17. P. J. Withers, W. M. Stobbs and O. B. Pedersen, *The Application of the Eshelby Method of Internal Stress Determination to Short Fibre Metal Matrix Composites*, Acta Metall., 37 (11), 1989, pp. 3061-3084.

18. V. Hauk, *Structural and Residual Stress Analysis by Nondestructive Methods*, Elsevier (Amsterdam), 1997.

19. I. C. Noyan, *Equilibrium Conditions for the Average Stresses Measured by X-rays*, Metall. Trans.-A, 14, 1983, pp. 1907-1914.

20. R. A. Winholtz, *Separation of Microstresses and Macrostresses*, in Measurement of Residual and Applied Stress Using Neutron Diffraction, eds. M. T. Hutchings and A. D. Krawitz, Kluwer Academic, London, 1992, pp.131-145.

21. M. E. Fitzpatrick, M. T. Hutchings and P. J. Withers, *Separation of Macroscopic, Elastic Mismatch and Thermal Expansion Misfit Stresses in Metal Matrix Quenched Plates from Neutron Diffraction Measurements*, Acta Mater., 45 (12), 1997, pp. 4867-4876.

22. I. C. Noyan and J. B. Cohen, *An X-ray Diffraction Study of the Residual Stress-Strain Distributions in Shot-peened Two-phase Brass*, Mater. Sci. Engng., 75, 1985, pp. 179-193.

23. J. D. Eshelby, *The Determination of the Elastic Field of an Ellipsoidal Inclusion and Related Problems*, in Proc. Roy. Soc., A241, 1957, pp. 376-396.

CHAPTER 3: EFFECT OF RESIDUAL STRESS ON MATERIAL PERFORMANCE

3.1 INTRODUCTION

The fatigue resistance of a component can be altered by the presence of any residual stress within it. The effect can either be detrimental or beneficial. Generally, tensile residual stresses promote premature or unexpected failure; whereas the fatigue life is enhanced by the presence of a compressive stress [1]. In most material failures, the fatigue cracks first initiate from the surface roughness and near-surface defects, which then grow rapidly to final failure. If the material is free from any pre-existing defects, up to 90% of the total fatigue life can be spent on the initiation of a fatigue crack under controlled amplitudes of cyclic stress or strain [2, 3]. It is thus highly desirable to delay the nucleation of any microcrack by introducing a compressive residual stress at the surface and just below the surface of the component; shot peening being an example of a common practice in manufacturing to achieve this. The harmful influence of tensile residual stresses for a premature failure of any component, particularly high risk components like aircraft and automobile parts, always justifies the importance of analysing the internal stresses, in order to obtain a better prediction of their performance. In this Chapter, a review of existing literature will be presented on the effect of residual stresses on material performance, for both particulate reinforced MMCs and welded steel components. But first, various stages in materials failure and their special features with regard to particulate reinforced MMCs will be discussed in the next section.

3.2 THREE STAGES IN MATERIALS FAILURE

The fatigue life of a component can be subdivided in three different stages: crack initiation, crack propagation and final fracture as described in figure 3.1.

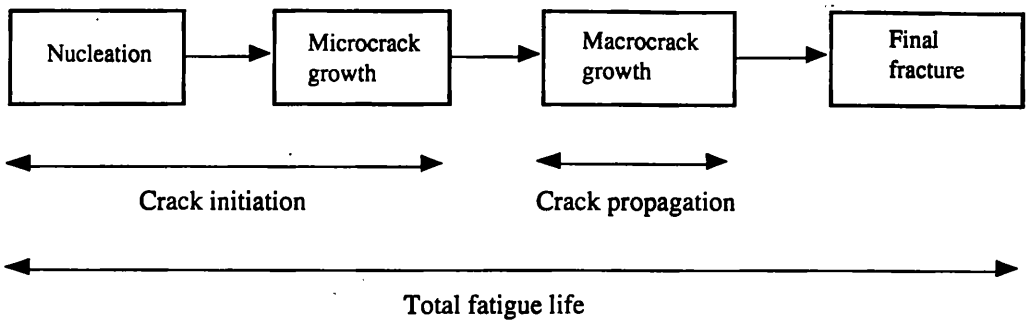

Figure 3.1: Three stages of materials fatigue life: crack initiation, crack propagation and final fracture.

It is difficult to make a precise definition of the start and the end of each phase except the last one. The final fracture occurs very fast during the last stress cycle of the fatigue life. Microscopic studies have revealed that the nucleation of cracks starts in the early phase of fatigue life and even the lack of proper demarcation between any two steps in figure 3.1 practically does not give any difficulty in terms of fatigue life estimation. The simplified definition of the fatigue life is then:

fatigue life = [crack initiation period] + [crack propagation period]

3.2.1 Crack Initiation

Typical nucleation sites for a fatigue crack may be pre-existing defects like pores and inclusions in the microstructure, or they may be generated during repeated cyclic straining. Controlled processing of materials (*e.g.* vacuum melting of steel, degassing etc.) is practised to minimise the pre-existing flaws and thus the fatigue life can be substantially improved. In the absence of any such defects, fatigue cracks in high purity metallic materials generally start at the surface as first proposed by Wood [4]. During cyclic straining, microscopic peaks (extrusions) and troughs (intrusions) are produced at the surface from the irreversible shear displacements along the slip bands, which result in surface 'roughening'. A staircase type surface offset is created in case of a monotonic straining. These intrusions act as micronotches and the effect of stress concentration at the root of the troughs enhances further slip and the initiation of a fatigue crack is promoted.

The fatigue life is improved if such offsets are removed by periodic surface polishing [5]. Initiation of fatigue cracks is also affected by the environmental conditions, such as temperature, humidity etc. Residual stresses also contribute; but not necessarily in an unfavourable way (*e.g.* shot peening, cold expansion of holes etc.). In engineering components made of commercial materials, fatigue can start both at the near surface region and in the interior, from various nucleation sites *e.g.* inclusions, voids or gas entrapments. Dents and scratches, macroscopic stress concentration or regions of chemical and microstructural inhomogeneity can also initiate the cracks.

In particulate reinforced MMCs, failure starts with the formation of micro-damage or voids caused by cracking of reinforcement particles or matrix and/or debonding at matrix-particle interfaces. The main factors favouring the formation of voids in such MMC are large reinforcement size, high matrix flow stress, particle clustering, large plastic strain, large particle surface normal to load, high particle aspect ratio etc. [6]. In a recent study on 2024 aluminium alloy reinforced with 10% (weight) silicon carbide particles, Tokaji *et al.* [7] observed the fatigue crack initiation from different sources *e.g.* surface defects, inclusions and particle-matrix interfaces, and they found that the particle size had a considerable influence on crack initiation. Srivatsan [8] noticed crack initiations by interfacial debonding or by cracking of individual or clusters of particles in an Al-Al_2O_3 MMC. Interfacial debonding was found to happen more frequently than particle cracking in [9]. During low cycle fatigue of an AA6061 alloy with 15 vol% SiC particles, Levin and Karlsson [10] found that cracks were initiated very early in the fatigue life, either near the particle-matrix interfaces in regions of SiC clusters or by the fracture of individual particles. Similar observation of void nucleation by the fracture or by debonding of reinforcement particles was made by Leggoe *et al.* [11]. A shift from the cracking of matrix adjacent to SiC particles to particle cracking was found by Ma *et al.* [12] when the size of SiC particles was increased from 3.5 μm to 20 μm. Fracture of large particles was also observed by others [13-16].

3.2.2 *Crack Propagation*

Once a crack is initiated in a material, it has to grow up to a critical dimension during the cyclic loading before catastrophic fracture occurs. Since most engineering structures are inherently flawed, their useful fatigue life may be considered as the crack propagation period only. Until the early 1960s, the rate of fatigue crack propagation, defined as the incremental change in crack length (a) per loading cycle (N), da/dN, used to be correlated with applied stress (σ) and crack length, by expressions of the form:

$$\frac{da}{dN} \propto \sigma^m a^n \qquad \text{(Equation 3.1)}$$

where m and n are empirical constants (m=2-7 and n=1-2). In 1961, Paris, Gomez and Anderson [17] suggested that the fatigue crack growth rate should be expressed in terms of stress intensity factor range ΔK which is defined as:

$$\Delta K = K_{max} - K_{min} \qquad \text{(Equation 3.2)}$$

K_{max} and K_{min} are the maximum and the minimum amounts, respectively, of stress intensity factors at the crack tip during the loading cycle and for a tensile opening mode of loading, they can be written as:

$$K_{max} = f\left(\frac{a}{W}\right)\sigma_{max}\sqrt{\pi a} \qquad \text{(Equation 3.3(a))}$$

$$K_{min} = f\left(\frac{a}{W}\right)\sigma_{min}\sqrt{\pi a} \qquad \text{(Equation 3.3(b))}$$

where $f\left(\frac{a}{W}\right)$ is a geometrical factor depending on the ratio of crack length (a) to the sample width (W), and σ_{max} and σ_{min} are, respectively, the maximum and the minimum values of the fatigue stress cycle. They proposed a relation of the form:

$$\frac{da}{dN} = A(\Delta K)^m \qquad \text{(Equation 3.4)}$$

where A and m are constants, influenced by material variables, test environment, temperature, load ratio R ($=K_{min}/K_{max}$) and frequency.

From the sigmoidal nature of the plot of log d*a*/d*N* with log ΔK, the general behaviour of a fatigue crack propagation can be subdivided into three different regions, as illustrated in figure 3.2.

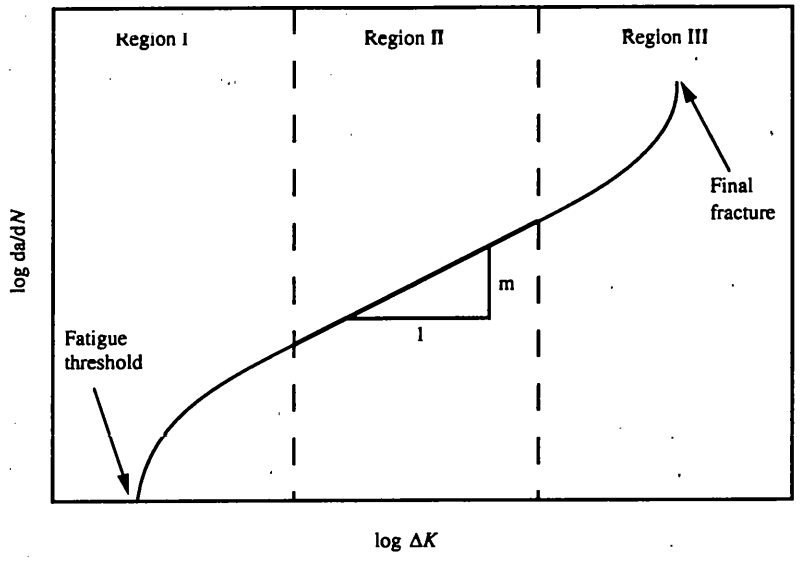

Figure 3.2: The three stages in fatigue crack growth.

The crack growth in Region I or the 'near-threshold' region is very slow (less than 10^{-6} mm per loading cycle). The stress intensity factor range in this region is just above its threshold value, ΔK_{th}, below which cracks do not grow. A steep rise in crack growth rate with ΔK is observed above the threshold. The slope of the curve then reduces to a constant value in Region II, with a linear variation of log d*a*/d*N* with log ΔK. This is also known as the Paris régime, after Paris *et al.* [17]. This intermediate region of crack growth in various engineering alloys has been the subject of most research for the last few decades. The crack growth rate in this region is influenced by many factors like microstructure, environment, load variables and the effects of crack closure. The value of the Paris slope *m* in most engineering alloys lies between 2 and 4 [3]. In Region III, the crack growth rates accelerate rapidly at high values of ΔK leading to catastrophic failure. Microstructures, the nature of the applied stress and the load ratio play important roles for crack growth in this region.

In composites, after the nucleation of voids, the fracture process continues with the growth and coalescence or linking up of those voids during the crack propagation stage. The effect of the reinforcement on the fatigue response of Al-SiC_p MMCs can be explained by figure

3.3, a plot of the crack propagation rate da/dN, with the range of stress intensity factor ΔK [6].

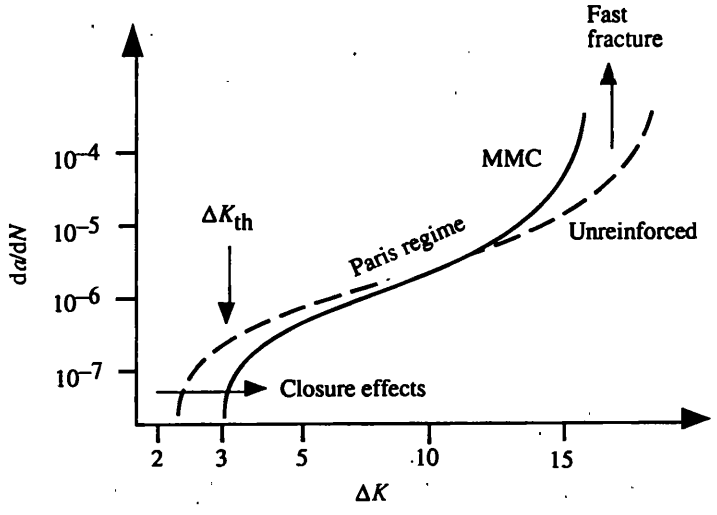

Figure 3.3: Schematic depiction of the effect of reinforcement on the fatigue response. The crack growth rate as a function of applied stress intensity factor for a typical discontinuous MMC can be compared with that of an unreinforced alloy [6].

In the near threshold region, Al-SiC_p composites exhibit higher fatigue thresholds (ΔK_{th}) than the unreinforced alloy, mentioned in some articles [18-21]. Various reasons can be attributed for this enhanced threshold *e.g.* deflection of fatigue cracks by the reinforcement [22]; a decrease in favoured crack paths by the reduction in slip band formation due to the particles [23]; lower crack tip opening displacements in the stiffer composite [24] and enhanced crack closure and crack trapping [25]. The Paris régime in composites is usually short, owing to their lower fracture toughness, with a higher Paris slope compared to the unreinforced alloy as illustrated in figure 3.3. This leads to the beginning of final fracture at a lower value of ΔK.

3.2.3 Final Fracture

At high values of the stress intensity factor range ΔK, the fatigue crack growth rate increases rapidly with ΔK (figure 3.2). The fatigue life of a component comes to an abrupt end with a catastrophic failure when the applied K_{max} reaches the critical value of tensile

mode stress intensity factor K_{Ic}, known as the plane strain fracture toughness of the material. In the case of particulate reinforced MMCs, at high ΔK, cracking of a large number of particles, present in the highly stressed plastic zone ahead of the crack, results in a fast failure mode and this effect is reflected in their inferior fracture toughness compared to that of an unreinforced alloy (figure 3.3) [6].

3.3 EFFECT OF RESIDUAL STRESSES ON FATIGUE OF MATERIALS

Since the importance of residual stress in materials performance was established, much research has been carried out on this subject in the last few decades. Numerous research articles on various types of residual stress fields and their effects in different material systems can be found (for example, references [26-40]). In this section, some general aspects of the effects of residual stresses will be discussed. Residual stresses and their effects in similar systems that were used in this study, *i.e.* in weldments and particulate reinforced MMCs, will be elaborated in the next section.

Generally, residual stresses arising from fabrication or surface and heat treatments influence the fatigue behaviour of the material in a similar fashion to a static mechanical load superimposed on a cyclic fatigue load. They alter the mean stress level of a fatigue cycle, and so they are advantageous, if compressive and deleterious, if tensile [3]. The general beneficial effects of compressive residual stresses have been studied by many researchers, and are reported in several conference proceedings, such as the proceedings mentioned in references [26, 34 and 38]. The generation of compressive residual stresses on the surfaces of engineering components is often practised to improve their fatigue performances. Berns and Weber [27] noted that the compressive residual stress at the surface delays crack initiation, whereas that beneath the surface acts like a mean stress and reduces the fatigue loading stress and consequently, the crack growth rate. The crack growth accelerates, once these compressive stresses decay out with the increase in depth leading to an increase in stress intensity. However, some tensile residual stresses are always generated beneath the

surface to counterbalance the compressive surface residual stresses. This area of tensile residual stress may initiate cracks [26] or increase the crack growth compared to a material without any residual stresses [37, 41], and even can convert an applied cyclic compressive stress to a tensile one and cause crack growth [28, 42]. The role of residual stresses induced by shot peening may also be affected by the presence of sub-surface crack sources [34] and a high dislocation density, leading to the negative effect that dominates over the beneficial effects of shot peening at higher temperatures [30].

When a crack grows through a residual stress field, the situation is complex. Wilks *et al.* [37] considered it important to estimate the stress intensity factor (K) correctly, taking the appropriate influence of the residual stresses into account; underestimating the value of K by 10% leads to a 40% underestimation of the crack growth rate which is usually approximately proportional to ΔK^4. They also concluded that the crack response was identical for both externally induced or self equilibrated residual stresses. For a proper estimation of K at the crack tip during crack growth through a residual stress field, two important factors must be considered; they are the crack closure effect and the effects of crack growth on the residual stress field. Closure of cracks may happen due to many reasons and it is termed accordingly, *e.g.* plasticity-induced, roughness-induced, oxide-induced, phase transformation-induced etc., details of which can be found in [3]. The complementary effects of a residual stress field and a growing crack on each other, and the redistribution of the residual stress field around the crack tip have been investigated by many researchers, for example references [29, 43-47]. There was a better correlation with the experimental data by the approach which accounted for additional stress effects generated from fatigue crack growth, and stress redistribution than one which did not [29, 44, 46, 47] or one which considered only the crack closure concept [46]. It is therefore imperative that the residual stresses in the crack wake and at the crack tip be considered in crack propagation models, since both will influence the crack growth behaviour [43]. Many articles can be found on modelling of the residual stress distribution in the presence of a fatigue crack, and for the prediction of fatigue life, for example, references [47-54]. Although the results of a few theoretical models are available [47-49], the finite element method is a common tool for such modelling [50-54]. Based on dislocation mechanics,

Tirosh and Ladelski [48] established the connection between the crack closure phenomena and residual stresses arising from fatigue cracks, along with an estimation of the "residual stress intensity factor", K_{IR}. The residual stress on the fracture surface was found by Rubiolo *et al.* [50] to increase initially with the increase in ΔK, up to a maximum value and then decrease; the levels of stress being influenced by the applied stress ratio and the hardening rate. Compressive residual stresses may also act as an external mechanism for crack closure [51]. They reduce the stress intensity factor for a crack under applied load, after cold expansion of a fastener hole [52] and thus increase the fatigue life of the cold worked specimens compared to non-cold worked ones [54]. A good agreement between the results for cracks in residual stress fields, produced by two techniques, *i.e.* dislocation density and finite element, was modelled by Wilks *et al.* [47].

3.4 RESIDUAL STRESSES IN WELDMENTS AND METAL MATRIX COMPOSITES

The term, 'residual stresses in weldments' is very general and may include different areas *e.g.* their origin, measurement, prediction, effects etc. and all of these for various kinds of welds. Similarly, residual stresses in MMCs will be different depending on the nature of matrix and reinforcement materials, state of the reinforcement (*i.e.* continuous fibre, whisker or particulate) etc. This part of the review will focus on similar materials, conditions and measurement techniques to those used in this study. Residual stress states and their effects in multipass welds (mainly in steels) and in particulate reinforced MMCs with Al alloy matrix will be discussed. The reported results of residual stresses in these materials, measured by diffraction techniques will also be reviewed.

3.4.1 Residual Stresses and Their Effects in Weldments

The repeated application of heat during multipass welding makes the process very complicated in terms of residual stress generation. A typical welding pass may act as a post-weld heat treatment for the initial pass(es) and as a preheat treatment for subsequent passes. So the residual stresses initially produced at the root of the weld in a multipass welded plate can be reduced by subsequent weld passes. An investigation of the residual stresses around a multipass weld in stainless steel pipes, like the one studied here, is very interesting from a practical point of view, as components in a power generation plant can suffer from reheat cracking in the heat affected zone (HAZ) of non-stress relieved weldments [55-57]; also tensile residual stresses at the inner side of the pipe may cause stress corrosion cracking (SCC). In a recent study on failure analysis and prevention in SCC, Komai [58] found that 60% of SCC failures occur in stainless steels, and identified residual stresses arising from welding as one of the most important factors for SCC in stainless steels.

The maximum residual stress that can be generated from welding in an austenitic stainless steel, is of yield magnitude. Generally, a high level of tensile residual stress along the longitudinal direction is generated throughout the thickness of a multipass butt weld in a flat plate; whereas a typical tension-compression-tension pattern is developed in the transverse direction [59]. The axial residual stress at a circumferential butt weld in an austenitic stainless steel pipe may be compressive at the outer surface and tensile at the inner one or a z-pattern of compression-tension-compression-tension through the thickness [59]; and along the axis, it is tensile at the weld and nearby HAZ, then gradually becomes compressive towards the parent metal [60]. The axis definitions which are generally used for residual stress analysis in welds in a plate and a pipe are shown in figure 3.4. Several other examples of residual stress states in multipass welds in plates and pipes can be found in references [59-63] and in conference proceedings as mentioned in [34] and [38]. Residual stresses measured by the diffraction techniques will be discussed in the next section.

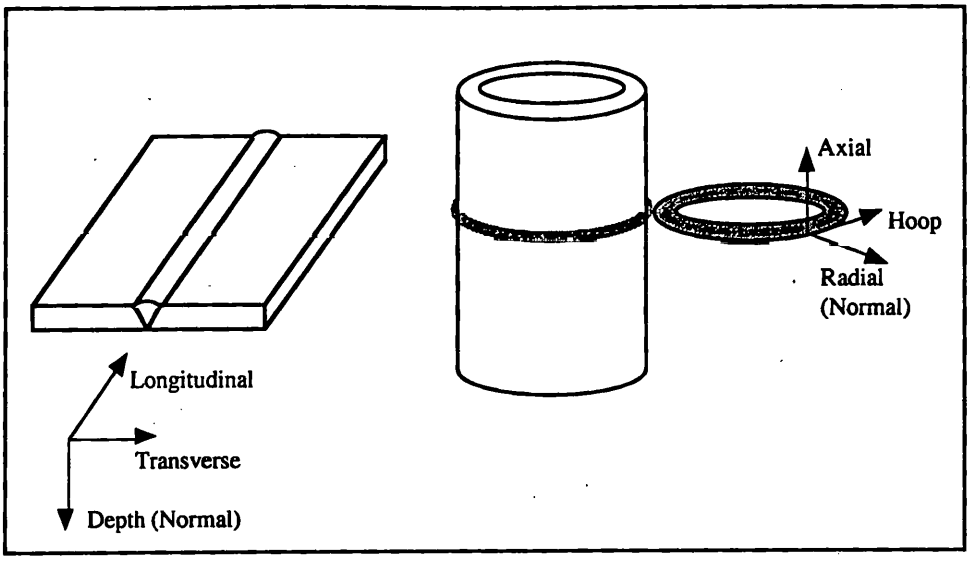

Figure 3.4: A general schematic diagram of multipass welds in plate and pipe and the axis definition.

Over the last 20 years, finite element analysis procedures have been applied increasingly to simulate residual stress fields associated with multipass weldments, mainly using two-dimensional models [64-67] but also some three dimensional ones[66-68]. Residual stress states in multipass welds in plate [64, 67], pipes [65, 68] and a combination of a cylinder and stiffening ring [66] have been studied. The 2-D model predictions generally match the experimentally measured values quite well; but sometimes may overestimate the residual stresses [67]. However, 3-D models are essential in predicting welding distortions in large structures [66].

In general, residual stresses induced by welding can increase the chance of SCC, cold cracking, brittle fracture and buckling of the component. They can also improve or degrade the fatigue strength depending on the compressive or tensile nature of the stress generated at the points critical for fatigue fracture. In a 316H austenitic stainless steel weld, an acceleration in crack growth rate was linked to the presence of tensile residual stresses by Spindler and Cotton [69]. A reduction in crack growth rate due to the presence of compressive residual stresses was observed by Itatani *et al.* [70] in the HAZ of a 304 stainless steel under simulated conditions of a boiling-water reactor environment. The residual stress in small diameter socket welded pipe joints was found to be compressive at

the toe and tensile at the root of the weld, which would influence the initiation of a crack from the root [71]. The effect of plate thickness on fatigue strength in welding has been studied by different researchers. The thickness effect was actually attributed to the residual stress [72] or to a combination of stress concentration factor and residual stress [73]. Post weld heat treatments or surface treatments are sometimes used to improve the fatigue strength of components. Takahasi *et al.* [73] observed almost complete removal of residual stresses after such heat treatments and thus a significant improvement in strength. However, the improvement in fatigue life in butt joints after different peening treatments has been explained by Nguyen and Wahab [74] by the fact that short cracks at the early stage of crack propagation cannot penetrate the region of compressive stress produced by peening.

3.4.2 A Review on Measurement of Residual Stresses in Weldments by Neutron Diffraction

During the last two decades, the neutron diffraction technique has been applied extensively to measure residual stresses in welded plates [75-87], blocks [88] and pipes [89-93] of different materials, and even in railway rails [94]. Welded components in a wide range of materials, such as aluminium alloys [81, 84, 85], ferritic [77, 80, 88] and austenitic [75, 76, 78, 83, 93] steels, and nickel-based superalloy [86] have been studied.

Generally high tensile stresses, particularly in the longitudinal direction, are developed at the weld centre and its nearby HAZ, and balancing compressive ones in the HAZ away from weld and in the parent metal [75-78, 81, 86]. A marked increase in longitudinal tensile stress after the second weld pass in a ferritic steel plate was observed by Prask *et al.* [80]. However, contradictory results of compressive stresses at the weld centre and a maximum tensile stress approaching the yield value near the surface just outside the weld zone in a single V-joint in austenitic steel plate [83] and in a double V-joint in aluminium alloy plates [84] have also been reported.

Different trends in through thickness variation of weld residual stresses were observed in different studies with various types of welds and different constraints during welding. In one of the earliest measurements in a double V-butt welded C-Mn steel plate, compressive stresses close to the yield value (~350 MPa) were found near the middle of the weld and tensile stresses of similar magnitude towards the surfaces, as can be seen in figure 3.5 [87].

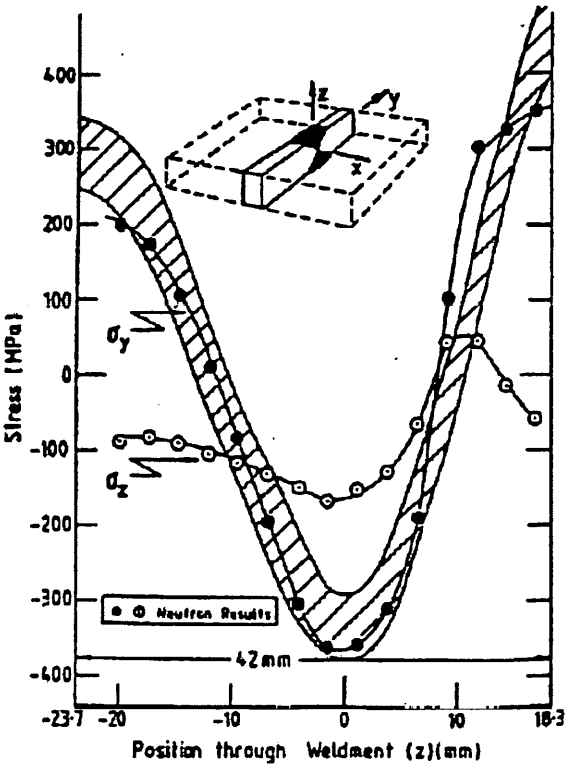

Figure 3.5: Variation of residual stress through a double V-weld sample, cut as shown in the inset. The points are neutron diffraction results and the shaded area denotes the range of strain gauge measurements [87].

Spooner *et al.* [75] noticed high tensile stresses (~400 MPa) at the bottom of a single V-butt weld and near-weld HAZ in a 304 stainless steel plate (25 mm thick) and at the mid-thickness, stresses were found to be less tensile than those at the bottom and top. The contour maps reported from another study on a similar weld plate of 12.7 mm thickness by Spooner *et al.* [76] show the maximum longitudinal stress (~400 MPa) at the top in the weld and HAZ, which decreased gradually towards the bottom. Since, in both cases the plates were restrained similarly during welding, this difference in behaviour might be attributed to the difference in plate thickness. In a plasma arc welded Al alloy plate, Albertini *et al.* [81] suggested a parabolic nature of stress variation through the thickness: they noticed a tensile

(~60 MPa) bulk and compressive (~–40 MPa) surfaces in the weld, whereas a compressive (~–150 MPa) bulk and tensile (~80 MPa) surfaces in the HAZ. The through thickness stress variation at the base metal plate is small [75, 77, 83]. In welded cylinders, highest tensile stresses were obtained mostly in the hoop direction and at the middle of wall thickness, either in the fusion zone [92, 93], or around the edges of the cap-pass heat-affected zone [91]. These high tensile stresses significantly decreased as the distance from the weld centre increased in the HAZ and parent metal [91-93], and towards the inner surface [91]. The residual stresses obtained from neutron measurements were compared with the calculated values from finite element analysis in a number of studies [89, 90, 93, 95, 96] and good agreements between the two were mentioned.

3.4.3 Neutron Diffraction Studies of Residual Stress and Its Effects in Particulate Reinforced MMCs – A Review

As described in Chapter 2, residual stresses are generated in MMCs when they are cooled down from a high temperature after fabrication or heat treatment. Development of high tensile residual stress in the matrix and compression in the reinforcement has been reported in many articles [97-101]. In a quenched and naturally aged plate of similar material, *i.e.* 2124 Al alloy reinforced with SiC particulates to that studied here, Fitzpatrick [102] reported a parabolic variation of strains through the thickness in the matrix phase; the surfaces being in compression and the centre in tension. Since mechanical loading, pre-straining and heat treatment are involved in the present work, it is worth reviewing literature in these areas that have been studied in particulate reinforced MMCs with neutron strain measurements.

Under uniaxial tensile loading, the longitudinal strain in the Al matrix of an Al/SiC_p composite, as measured by Akiniwa *et al.* [103], increased proportionally with applied stress whilst the transverse strain decreased. In another study on the phase stress partition during uniaxial tensile loading of a 2219 Al/15 vol.% TiC_p composite, a deviation from the linearity in the relationship between the phase stresses and the applied load was observed during the micro-yielding of the matrix, well before the nominal 0.2% proof stress [104].

When the tensile loading crosses the elastic limit, plastic deformation occurs only in the matrix, which will then contract less than the reinforcement on unloading. Therefore compressive residual stresses will develop in the matrix and the reinforcement will contain the remnant tensile strains and will be in a state of tensile residual stress. Thus there will be a redistribution of the thermal residual stress states in both phases in a quenched MMC following a plastic deformation. For a proper understanding of the observed lattice strains during tensile loading experiments, two more important factors, in addition to the elastic transfer of load arising from the higher stiffness of the reinforcement, are the plastically induced stresses in the composite when the applied load approaches the nominal 0.2% yield stress, and the stress relaxation mechanisms [105]. Creep relaxation as observed in 6061Al/15% SiC_p composite at 110°C [106] and particle cracking as evidenced in an Al/ZrO_2 particulate composite [107] can be different load transfer mechanisms. In the case of particle cracking and debonding of the particle-matrix interface, the transfer of load from matrix to reinforcement may reduce significantly [108].

The change in lattice spacing arising from different times of ageing at 230°C for a range of SiC volume fraction in Al-3.5wt.% Cu alloy/SiC_p composite was monitored by Hermann *et al.* [109]. They observed a rapid change in *d*-spacing in the SiC phase within the first 15 minutes, which could be interpreted in terms of thermal misfit stress, and the final strains were larger in specimens with a higher volume fraction of SiC. But the changes in matrix lattice parameter took place over a longer period of time, with a higher rate for higher SiC volume fraction owing to increased age hardening (precipitation of Al_2Cu or θ' phase). Lorentzen and Clarke [110] measured the residual lattice strains in both phases in an Al-20% SiC_p composite to study the effects of uniaxial plastic deformation at room temperature and elevated temperature. They found a close agreement between the temperature dependence of the separation of matrix yield strains in tension and in compression and the temperature dependence of macroscopic flow stress. In several studies, Fitzpatrick has separated the macro and the micro stress components in Al/SiC_p composites after measuring the residual strain profile in specimens from a quenched plate [111, 112] and around fatigue cracks in specimens with different levels of initial residual stresses, set up by previous heat treatments

[113]. The same technique for the separation of stress components has been used here, as described in the previous Chapter.

The effects of any residual stress field on fatigue in an MMC are similar to those seen in other metallic materials: tensile stresses increase the crack growth rate whereas compressive ones reduce it. This may cause severe bowing of the fatigue crack front [114] in a quenched MMC plate, owing to the compressive stresses at the surfaces and tension at the centre. The effects of residual stress and crack closure on the crack growth rate in quenched Al/SiC_p composite plates have been the subject of some study [114-118]. The rate of crack growth increases as the crack grows through the thickness, *i.e.* as it proceeds from the compressive surface zone to a tensile centre region [115]. Experimental evidence suggests high levels of crack closure owing to compressive residual stresses at and near the surface of quenched MMC plates [115-118]. This closure effect will be much less if the residual stress is relieved by either stretching [116] or overageing and annealing heat treatments [115, 117, 118]. With the help of three dimensional elastic-plastic finite element analyses, Davis and Allison [119] found a significant influence of residual stress-induced matrix plasticity near the particles on the overall elastic and plastic properties of the composite; whereas Ho and Saigal [120] reported that the presence of thermally-induced residual stress in an Al/SiC_p composite might improve its yield strength and decrease the elastic modulus. Finite element models were also used in references [104, 118] to calculate the internal strain development, showing good agreements with the experimental results.

3.5 REFERENCES

1. E. S. Rowland, *Effect of Residual Stress on Fatigue*, in Proc. 10th Sagamore Army Materials Research Conference, eds. J. J. Burke *et al.*, Sagamore Conference Centre, New York, Syracuse University Press, 1963, pp. 229-244.

2. J. Schijve, *Four Lectures on Fatigue Crack Growth*, Engng. Fract. Mech., 11, 1979, pp. 167-221.

3. S. Suresh, *Fatigue of Materials*, Cambridge Solid State Science Series, Cambridge University Press, 1991.

4. W. A. Wood, *Formation of Fatigue Cracks*, Phil. Mag., 3, 1958, pp. 692-699.

5. T. H. Alden and W. A. Backofen, *The Formation of Fatigue Cracks in Aluminium Single Crystals*, Acta Metall., 9, 1961, pp. 352-366.

6. T. W. Clyne, P. J. Withers, *An Introduction to Metal Matrix Composites*, Cambridge Solid State Science Series, Cambridge University Press, 1993.

7. K. Tokaji, H. Shiota, K. Kobayashi, *Effect of Particle Size on Fatigue Behaviour in SiC Particulate-Reinforced Aluminium Alloy Composite*, Fatigue Fract. Engng. Mater. Struct., 22 (4), 1999, pp. 281-288.

8. T. S. Srivatsan, *Microstructure, Tensile Properties and Fracture Behaviour of Al_2O_3 Particulate-Reinforced Aluminium Alloy Metal Matrix Composites*, J. Mater. Sci., 31 (5), 1996, pp. 1375-1388.

9. Z. Wang and R. J. Zhang, *Microscopic Characteristics of Fatigue Crack Propagation in Aluminium Alloy Based Particulate Reinforced Metal Matrix Composites*, Acta Metall. Mater., 42 (4), 1994, pp. 1433-1445.

10. M. Levin and B. Karlsson, *Crack Initiation and Growth during Low-Cycle Fatigue of Discontinuously Reinforced Metal-Matrix Composites*, Int. J. Fatigue, 15 (5), 1993, pp. 377-387.

11. J. W. Leggoe, X. Z. Hu, M. B. Bush, *Crack Tip Damage Development and Crack Growth Resistance in Particulate Reinforced Metal Matrix Composites*, Engng. Fract. Mech., 53 (6), 1996, pp. 873-895.

12. Z. Y. Ma, J. Bi, Y. X. Lu, M. Luo, Y. X. Gao, *Effect of SiC Particulate Size on Properties and Fracture Behaviour of SiC_p/2024Al Composites*, in Proc. Ninth Int. Conf. on Composite Materials (ICCM-9), ed. A. Miravete, Madrid, Spain, University of Zaragoza/Woodhead Publishing Ltd., Vol. 1, 1993, pp. 448-453.

13. D. Lloyd, *Aspects of Particle Fracture in Particulate Reinforced MMCs*, Acta Metall. Mater., 39, 1991, pp. 59-72.

14. M. Manoharan and J. J. Lewandowski, *Crack Initiation and Growth Toughness of an Al MMC*, Acta Metall. Mater., 38, 1990, pp. 489-496.

15. J. N. Hall, J. W. Jones, A. K. Sachdev, *Particle Size, Volume Fraction and Matrix Strength Effects on Fatigue Behaviour and Particle Fracture in 2124 Aluminium-SiC_p Composite*, Mater. Sci. Engng.-A, 183, 1994, pp. 69-80.

16. J. K. Shang, W. Yu and R. O. Ritchie, *Role of Silicon Carbide Particles in Fatigue Crack Growth in SiC-Particulate-Reinforced Aluminium Alloy Composites*, Mater. Sci. Engng.-A, 102, 1988, pp. 181-192.

17. P. C. Paris, M. P. Gomez and W. P. Anderson, *A Rational Analytic Theory of Fatigue*, The Trend in Engng., 13, 1961, pp. 9-14.

18. T. Christman and S. Suresh, *Effects of SiC Reinforcement and Aging Treatment on Fatigue Crack Growth in an Al-SiC Composite*, Mater. Sci. Engng.-A, 102, 1988, pp. 211-216.

19. D. L. Davidson, *The Growth of Fatigue of Cracks Through Particulate SiC Reinforced Aluminium Alloys*, in Proc. Int. Conf. on Fracture (ICF7), eds. K. Salama, K. Ravichandar, D. M. R. Taplin and P. R. Rao, Texas, Pergamon Press, 1989, pp. 3021-3028.

20. D. L. Davidson, *The Effect of Particulate SiC on Fatigue Crack Growth in a Cast Extruded Aluminium Alloy Composite*, Metall. Trans.-A, 22, 1991, pp. 97-112.

21. R. J. Arsenault, S. Fishman and M. Taya, *Deformation and Fracture Behavior of Metal-Ceramic Matrix Composite Materials*, Progress in Mater. Sci., 38, 1994, pp. 1-157.

22. A. J. Padkin, M. F. Brereton and W. J. Plumbridge, *Fatigue Crack Growth in Two-Phase Alloys*, Mater. Sci. Tech., 3, 1987, pp. 217-223.

23. D. R. Williams and M. E. Fine, *Quantitative Determination of Fatigue Microcrack Growth in SiC_w Reinforced 2124 Al Alloy Composite*, in Proc. Fifth Int. Conf. on Composite Materials (ICCM V), San Diego, eds. W. C. Harrigan, J. Strife and A. Dhingra, TMS-AIME, pp. 639-670.

24. J. K. Shang and R. O. Ritchie, *Crack Bridging by Uncracked Ligaments During Fatigue-Crack Growth in SiC-Reinforced Aluminium-Alloy Composites*, Metall. Trans.-A, 20, 1989, pp. 897-908.

25. J. K. Shang and R. O. Ritchie, *On the Particle-Size Dependence of Fatigue-Crack Propagation Thresholds in SiC-Particulate-Reinforced Aluminium-Alloy Composites: Role of Crack Closure and Crack Trapping*, Acta Metall. 37 (8), 1989, pp. 2267-2278.

26. J. Broichhausen, W. Calles, *Effect of Residual Stresses on the Fatigue Behaviour, Crack Origin and Growth Velocity of Cold-Worked Ti-6Al-4V*, in Proc. Residual Stress in Science and Technology, eds. E. Macherauch and V. Hauk, DGM Informationsgesellschaft, 1987, Verlag, Germany, pp. 729-734.

27. H. Berns and L. Weber, *Fatigue Crack Growth in the Presence of Residual Stresses*, *ibid*, pp. 751-758.

28. R. Hermann and C. N. Reid, *Slow Crack Growth in the Presence of Residual Stresses*, *ibid*, pp. 759-766.

29. E. Welsch, D. Eifler, B. Scholtes and E. Macherauch, *Inhomogeneous Plastic Deformations and Residual Stress Distributions in the Crack Tip Region of Fatigued 42CrMo4 (SAE4140) and Their Consequences on Fatigue Crack Propagation*, *ibid*, pp. 785-792.

30. H. Gray, L. Wagner and Gütjering, *Influence of Residual Stresses on Fatigue Crack Propagation of Small Surface Cracks*, *ibid*, pp. 815-822.

31. U. Selvadurai-Lassl, H. -A. Crostack, W. Reimers, T. Vogt, G. Eckold, *Deformation Analysis in Mixed Composites*, in Proc. Measurement of Residual and Applied

Stress Using Neutron Diffraction, eds. M. T. Hutchings and A. D. Krawitz, Kluwer Academic Publishers, 1992, pp. 451-459.

32. M. A. M. Bourke, H. J. MacGillivray, G. A. Webster and P. J. Webster, *Residual Stress Distribution in Cracked Autofrettaged Tubing*, *ibid*, pp. 481-492.

33. A. N. Ezeilo, P. S. Webster, G. A. Webster and P. J. Webster, *Development of the Neutron Development Technique for the Determination of Near Surface Residual Stresses in Critical Gas Turbine Components*, *ibid*, pp. 535-543.

34. L. Jinkui, S. Peige, W. Shengping, Y. Mei, W. Renzhi and L. Xiangvin, *An Understanding of the Effect of Residual Stress Induced by Shot Peening on Fatigue Strength*, in Proc. of the Fourth International Conference on Residual Stresses (ICRS 4), Baltimore, MA, Society for Experimental Mechanics, 1994, pp. 1002-1007.

35. P. Holdway, R. Cook and A. W. Bowen, *Residual Stress Distribution and Fatigue Properties of Aluminium-Lithium 8090 5mm Plate Containing Plain and Cold-Expanded Fastener Holes*, *ibid*, pp. 1046-1054.

36. M. Ceretti, H. Michaud, M. Perrin, A. Lodini, *Residual Stress Measurement in a Plasma Semi-Transferred Arc (PTA) Coating by Neutron and X-ray Diffraction*, *ibid*, pp. 1055-1061.

37. M. D. B. Wilks, D. Nowell and D. A. Hills, *The Influence of Residual Stress in Crack Growth Rate*, *ibid*, pp.1238-1245.

38. J. D. Almer, J. B. Cohen, K. R. McCallum, R. A. Winholtz, *X-ray Diffraction and Finite Element Study of Residual Stress Effects on Fatigue Crack Growth*, in Proc. Fifth International Conference on Residual Stresses (ICRS-5), eds. T. Ericsson, M. Odén and A. Andersson, Linköping University, Sweden, 1997, pp. 1072-1077.

39. S. Jägg and B. Scholtes, *Crack Propagation and Crack Tip Residual Stresses after Different Loading Histories of Steel S690QL1*, *ibid*, pp. 1078-1083.

40. S. Ohya, Y. Yoshioka, K. Watanuki, *The Estimation of Range of Stress Intensity Factor ΔK by Residual Stress Distribution, ibid*, pp. 1096-1101.

41. W. Elber, *Effects of Shot-Peening Residual Stresses on the Fracture and Crack Growth Properties of D6AC Steel*, in Fracture Toughness and Slow-Stable cracking, ASTM STP 559, ASTM, pp. 45-58.

42. K. Kasaba, T. Sano, S. Kudo, T. Shoji, K. Katagiri, T. Sato, *Fatigue Crack Growth Under Compressive Loading*, J. Nuclear Mater., 263 (B), 1998, pp. 2059-2063.

43. W. Sun and H. Sehitoglu, *Residual Stress Fields During Fatigue Crack Growth*, Fatigue Fract. Engng. Mater. Struct. 15 (2), 1992, pp. 115-128.

44. Y. C. Lam and K. S. Lian, *The Effect of Residual Stress and Its Redistribution on Fatigue Crack Growth*, Theoret. Appl. Fract. Mech., 12, 1989, pp. 59-66.

45. M. E. Fitzpatrick and L. Edwards, *Fatigue Crack Residual Stress Field Interactions and Their Implications for Damage-Tolerant Design*, J. Mater. Engng. Perf., 7 (2), 1998, pp.190-198.

46. Y. B. Lee, C. S. Chung, Y. K. Park, H. K. Kim, *Effects of Redistributing Residual Stress on the Fatigue Behavior of SS330 Weldment*, Int. J. Fatigue, 20 (8), 1998, pp. 565-573.

47. M. D. B. Wilks, D. Nowell, D. A. Hills, *The Evaluation of Stress Intensity Factors for Plane Cracks in Residual Stress Fields*, J. Strain Anal., 28 (3), 1993, pp. 145-152.

48. J. Tirosh and A. Ladelski, *Note on Residual Stresses Induced by Fatigue Cracking*, Engng. Fract. Mech., 13, 1980, pp. 453-461.

49. V. M. A. Leitao, M. H. Aliabadi, D. P. Rooke, R. Cook, *Boundary Element Methods for the Analysis of Crack Growth in the Presence of Residual Stress Fields*, J. Mater. Engng. Perf., 7 (3), 1998, pp. 352-360.

50. G. H. Rubiolo, J. C. Rios and P. Gargano, *A Finite-Element Analysis of the Residual Stress Distribution in the Vicinity of a Fatigue Fractured Surface*, Engng. Fract. Mech., 60 (4), 1998, pp. 447-455.

51. M. A. Moshier and B. M. Hillberry, *The Inclusion of Compressive Residual Stress Effects in Crack Growth Modelling*, Fatigue Fract. Engng. Mater. Struct., 22, 1999, pp. 519-526.

52. M. J. Pavier, C. G. C. Ponssard, D. J. Smith, *Finite Element Modelling of the Interaction of Residual Stress with Mechanical Load for a Crack Emanating from a Cold Worked Fastener Hole*, J. Strn. Anal. Engng. Design, 33 (4), 1998, pp. 275-289.

53. M. Guagliano, *A Numerical Model to Investigate the Role of Residual Stresses on the Mechanical Behaviour of Al/Al_2O_3 Particulate Composites*, J. Mater. Engng. Perf., 7 (2), 1998, pp. 183-189.

54. M. Toparli, A. Ozel, T. Aksoy, *Effect of Residual Stresses on the Fatigue Crack Growth Behaviour at Fastener Holes*, Mater. Sci. Engng.-A, 225 (1-2), 1997, pp. 196-203.

55. A. Dhooge and A. Vinckier, *Reheat Cracking – a Review of Recent Studies*, Int. J. of Pressure Vessels and Piping, 27(4), 1987, pp.239-269.

56. H. Kanbach, K. Detert and A. Rukwied, *Effect of Weld Heat Input and Creep Strain on the Elevated Temperature and Crack Growth Properties of Austenitic Steels*, Steel Research , 60(7), 1989, pp. 329-335.

57. C. Picker and A. S. Fraser, *Experience of Cracking in Austenitic Stainless Components of the UK Prototype Fast Reactor*, Int. J. of Pressure Vessels and Piping, 65 (3), 1996, pp. 283-293.

58. K. Komai, *Failure Analysis and Prevention in SCC and Corrosion Fatigue Cases*, Int. J. Fatigue, 20 (2), 1998, pp. 145-154.

59. R. H. Leggatt, *Welding Residual Stresses*, in Proc. Fifth International Conference on Residual Stresses (ICRS-5), eds. T. Ericsson, M. Odén and A. Andersson, Linköping University, Sweden, 1997, pp. 12-25.

60. H. Wohlfahrt, *Residual Stresses due to Welding: Their Origin, Calculation and Evaluation*, in Residual Stresses, eds. E. Macherauch and V. Hauk, DGM Informationsgesellschaft, Verlag, 1986, pp. 81-112.

61. F. Eichhorn, R. Poje, G. Hofer, R. Scrödrer, B. Scholtes, H. D. Steffens, H. Kern, H. Wohlfahrt, J. Heeschen, *Residual Stresses in Welded Joints and Sprayed Coatings*, in Proc. Residual Stress in Science and Technology, eds. E. Macherauch and V. Hauk, DGM Informationsgesellschaft, 1987, Verlag, Germany, pp. 977-987.

62. R. H. Leggatt, *Residual Stress and Distortion in Multipass Butt Welded Joints in Type 316 Stainless Steel, ibid*, pp. 997-1004.

63. A. Joseph, P. Palanichamy, S. K. Rai, T. Jayakumar, B. Raj, *Non-Destructive Measurement of Residual Stresses in Carbon Steel Weld Joints*, Sci. Tech. of Welding and Joining, 3 (6), 1998, pp. 267-271.

64. E. F. Rybicki. J. R. Shadley, A. S. Sandhu, R. B. Stonesifer, *Experimental and Computational Residual-Stress Evaluation of a Weld Clad Plate and Machined Test Specimens*, Trans. ASME- J. Engng. Mater. Tech., 110 (4), 1988, pp. 297-304.

65. J. K. Hong, C. L. Tsai, P. Dong, *Assessment of Numerical Procedures for Residual Stress Analysis of Multipass Welds*, Welding J., 77 (9), 1998, pp. S372-S382.

66. S. Brown and H. Song, *Finite-Element Simulation of Welding of Large Structures*, Trans. ASME- J. Engng. for Industry, 114 (4), 1992, pp. 441-451.

67. J. M. J. McDill, A. S. Oddy and J. A. Goldak, *Comparing 2-D Plane Strain and 3-D Analyses of Residual Stresses in Welds*, in Proc. International Trends in Welding Science and Technology, eds. S.A. David and J. M. Vitek, ASM International, Materials Park, OH, 1993, pp. 105-108.

68. Y. Dong, J. K. Hong, C. L. Tsai, P. Dong, *Finite Element Modeling of Residual Stresses in Austenitic Stainless Steel Pipe Girth Welds*, Welding J., 76 (10), 1997, pp. S442-S449.

69. M. W. Spindler, C. C. Cotton, *Creep-Fatigue Crack Growth in Type 316h Stainless Steel Through a Zone of Tensile Residual Stress*, Mater. at High Temp., 15 (2), 1998, pp. 117-121.

70. M. Itatani, J. Fukakura, M. Asano, M. Kikuchi, N. Chujo, *Fatigue Crack Growth Behaviour of Weld Heat-Affected Zone of Type-304 Stainless Steel in High Temperature Water*, Nuclear Engng. Design, 153 (1), 1994, pp. 27-34.

71. T. Yamashita, T. Hattori, K. Iida, T. Nomoto, M. Sato, *Effects of Residual Stress on Fatigue Strength of Small –Diameter Welded Pipe Joint*, Trans. ASME- J. Press. Vessel Tech., 119 (4), 1997, pp. 428-434.

72. A. Ohta, T. Mawari, N. Suzuki, *Evaluation of Effect of Plate Thickness on Fatigue Strength of Butt Welded-Joints by a Test Maintaining Maximum Stress at Yield Strength*, Engng. Fract. Mech., 37 (5), 1990, pp. 987-993.

73. I. Takahasi, T. Yoshit, H. Iidaka, E. Fujii, K. Matsuoka, *Fatigue Strength of Non-Load-Carrying Fillet Welded Joints – Effects of Weld Residual-Stresses and Stress-Concentration*, Fatigue Fract. Engng. Mater. Struct., 16 (1), 1993, pp. 37-51.

74. T. N. Nguyen and M. A. Wahab, *The Effect of Residual Stresses on Fatigue of Butt Joints*, Welding J., 75 (2), 1996, pp. S55-S61.

75. S. Spooner, J. A. Fernandez Baca, S. A. David, C. R. Hubbard, T. M. Holden and J. H. Root, *Investigation of Residual Stresses in a Multipass Weld in 1" Stainless Steel Plate*, in Proc. of the Fourth International Conference on Residual Stresses (ICRS 4), Baltimore, MA, Society for Experimental Mechanics, 1994, pp. 1205-1209.

76. S. Spooner, X. L. Wang, C. R. Hubbard and S. A. David, *Residual Stresses in a Multipass Weld in an Austenitic Stainless Steel Before and After Thermal Stress Relief*, *ibid*, pp. 964-969.

77. J. H. Root, T. M. Holden, J. Schroder, C. R. Hubbard, S. Spooner, T. A. Dodson and S. A. David, *Residual Stress Mapping in Mutipass Ferritic Steel Weld*, Mater. Sci. Tech., 9 (9), 1993, pp. 754-759.

78. P. J. Webster, G. Mills, X. D. Wang, W. P. Kang and T. M. Holden, *Neutron Strain Scanning of a Small Welded Austenitic Stainless Steel Plate*, J. Strain Anal. for Engng. Design, 30 (1), 1995, pp. 35-43.

79. G. Albertini, F. M. Cernuschi, G. Cicognani, S. Ghia, T. Lorentzen and F. Rustichelli, *Residual Strain Measurements in Welded Steel Fe510D*, in Proc. of the Fourth International Conference on Residual Stresses (ICRS 4), Baltimore, MA, Society for Experimental Mechanics, 1994, pp. 959-963.

80. H. J. Prask, R. J. Fields, P. C. Brand and J. M. Blackburn, *Evolution of Residual Stresses Around a V-Notch Weldment*, *ibid*, pp. 1198-1204.

81. G. Albertini, G. Bruno, B. D. Dunn, F. Fiori, W. Reimers and J. S. Wright, *Comparative Neutron and X-ray Residual Stress Measurements on Al-2219 Welded Plate*, Mater. Sci. Engng.-A, 224, 1997, pp. 157-165.

82. T. Lorentzen and J. B. Ibsø, *Neutron Diffraction Measurements of Residual Strains in Offshore Welds*, Mater. Sci. Engng.-A, 197, 1995, pp. 209-214.

83. S. Spooner, S. A. David, J. H. Root, T. M. Holden, M. A. M. Bourke and J. A. Goldstone, *Residual Stress and Strain Measurements in an Austenitic Steel Plate Containing a Multipass Weld*, in Proc. International Trends in Welding Science and Technology, eds. S.A. David and J. M. Vitek, ASM International, Materials Park, OH, 1993, pp. 139-143.

84. P. J. Webster, *Welding Applications of Neutron Strain Scanning*, *ibid*, pp. 95-98.

85. D. J. Smith, R. H. Leggatt, G. A. Webster, H. J. MacGillivary, P. J. Webster, G. Mills, *Neutron Diffraction Measurements of Residual-Stress and Plastic-Deformation in an Aluminium-Alloy Weld*, J. Strain Anal. Engng. Design, 23 (4), 1988, pp. 201-211.

86. H. J. Stone, P. J. Withers, T. M. Holden, S. M. Roberts, R. C. Reed, *Comparison of Three Different Techniques for Measuring the Residual Stresses in an Electron Beam Welded Plate of WASPALOY*, Metall. Mater. Tans.-A, 30 (7), 1999, pp. 1797-1808.

87. A. J. Allen, M. T. Hutchings, C. G. Windsor and C. Andreani, *Neutron Diffraction Methods for the Study of Residual Stress Fields*, Adv. in Physics, 34 (4), 1985, pp. 445-473.

88. A. J. Allen, R. Coppola, M. T. Hutchings, M. Valli and C. G. Windsor, *Study of Residual Stress in a Ferritic Steel Electron Beam Test Weldment Using Neutron Diffraction*, Mater. Letters, 23 (1995), pp. 265-268.

89. M. Nasstrom, P. J. Webster and J. Wang, *Residual Stresses and Deformations due to Longitudinal Welding of Pipes*, in Proc. International Trends in Welding Science and Technology, eds. S.A. David and J. M. Vitek, ASM International, Materials Park, OH, 1993, pp. 109-115.

90. X. L. Wang, E. A. Payzant, B. Taljat, C. R. Hubbard, J. R. Keiser and M. J. Jirinec, *Experimental Determination of the Residual Stresses in a Spiral Weld Overlay Tube*, Mater. Sci. Engng.-A, 232, 1997, pp. 31-38.

91. R. A. Winholtz and A. D. Krawitz, *The Relaxation of Residual-Stresses with Postweld Heat-Treatment in a High Performance Weld Measured with Neutron Diffraction*, Metall. Mater. Trans.-A, 26 (5), 1995, pp. 1287-1295.

92. J. H. Root, C. E. Coleman, J. W. Bowden and M. Hayashi, *Residual Stresses in Steel and Zirconium Weldments*, Trans. ASME- J. Press. Vessel Tech., 119 (2), 1997, pp. 137-141.

93. H. Runnemalm, R Lin, *Investigation of Residual Stresses in a Laser Welded Pipe by Finite Element Simulations and Neutron Diffraction Measurements*, in Proc. Fifth International Conference on Residual Stresses (ICRS-5), eds. T. Ericsson, M. Odén and A. Andersson, Linköping University, Sweden, 1997, pp.183-188.

94. P. J. Webster, G. Mills, X. D. Wang, W. P. Kang, T. M. Holden, *Residual Stresses in Alumino-Thermic Welded Rails*, J. Strain Anal. Engng. Design, 32 (6), 1997, pp. 389-400.

95. K. W. Mahin, W. Winters, T. M. Holden, R. R. Hosbons and S. R. MacEwen, *Prediction and Measurement of Residual Elastic Strain Distributions in Gas Tungsten Arc Welds*, Welding J., 70 (9), 1991, pp. s245-s260.

96. L. Wikander, L. Karlsson, M. Nasstrom and P. Webster, *Finite Element Simulation and Measurement of Welding Residual Stresses*, Modelling and Simulation in Mater. Sci. and Engng., 2 (4), 1994, pp. 845-864.

97. H. M. Ledbetter and M. W. Austin, *Thermal Stress in a Silicon-Carbide/Aluminium Composite*, in Proc. Residual Stress in Science and Technology, eds. E. Macherauch and V. Hauk, DGM Informationsgesellschaft, 1987, Verlag, Germany, pp. 517-521.

98. Z. M. Sun, J. B. Li, Z. G. Wang and W. J. Li, *Residual Stresses in Silicon Carbide Particulate Reinforced Aluminium Composites*, Acta Metall. Mater., 40 (11), 1992, pp. 2961-2966.

99. K. Maeda, K. Wakashima, M. Ono, *Stress States in Quenched SiC/Al Particulate Composites Examined by Neutron Diffraction*, Scripta Mater., 36 (3), 1997, pp. 335-340.

100. M. Ceretti, C. Braham, J. L. Lebrun, J. P. Bonnafe, M. Perrin, A. Lodini, *Residual Stress Analysis by Neutron and X-ray Diffraction Applied to the Study of Two Phases Materials: Metal Matrix Composites*, in Proc. of the Fourth International Conference on Residual Stresses (ICRS 4), Baltimore, MA, Society for Experimental Mechanics, 1994, pp. 32-39.

101. L. F. Smith, A. D. Krawitz, P. Clarke, S. Saimoto, N. Shi and R. J. Arsenault, *Residual Stresses in Discontinuous Metal Matrix Composites*, Mater. Sci. Engng.-A, 159, 1992, pp. L13-L15.

102. M. E. Fitzpatrick, Ph. D. Thesis, Department of Materials Science and Metallurgy, University of Cambridge, 1995.

103. Y. Akiniwa, K. Tanaka, T. Takezono, N. Minakawa and Y. Morii, *Neutron and X-ray Diffraction Study of Phase Stresses in SiC Particulate Reinforced Aluminium Alloy*, in Proc. Fifth International Conference on Residual Stresses (ICRS-5), eds. T. Ericsson, M. Odén and A. Andersson, Linköping University, Sweden, 1997, pp. 982-987.

104. N. Shi, M. A. M. Bourke, J. A. Roberts, J. E. Allison, *Phase-Stress Partition during Uniaxial Tensile Loading of a TiC-Particulate–Reinforced Al Composite*, Metall. Mater. Trans.-A, 28 (12), 1997, pp. 2741-2753.

105. A. J. Allen, M. A. M. Bourke, S. Dawes, M. T. Hutchings, P. J. Withers, *The Analysis of Internal Strains Measured by Neutron Diffraction in Al-SiC Metal Matrix Composites*, Acta Metall. Mater., 40 (9), 1992, pp. 2361-2373.

106. M. A. M. Bourke, J. A. Goldstone, N. Shi, G. T. Gray, M. R. James, R. I. Todd, *The Use of Pulsed Neutron Diffraction to Measure Strain in Composites*, in Proc. of the Fourth International Conference on Residual Stresses (ICRS 4), Baltimore, MA, Society for Experimental Mechanics, 1994, pp. 539-548.

107. C. A. Lewis, P. J. Withers, *Weibull Modeling of Particle Cracking in Metal-Matrix Composites*, Acta Metall. Mater., 43 (10), 1995, pp. 3685-3699.

108. C. A. Lewis, W. M. Stobbs, P. J. Withers, *Internal-Stress Induced Debonding in a Zirconia-Reinforced 6061 Aluminium-Alloy Composite*, Mater. Sci. Engng.-A, 171 (1-2), 1993, pp. 1-11.

109. R. Hermann, D. Q. Wang, M. A. Tomlinson and L. Edwards, *Measurements of Residual Stresses in Metal-Matrix Composites During Heat-Treatment Using Neutron*

Diffraction Technique, in Proc. of the Fourth International Conference on Residual Stresses (ICRS 4), Baltimore, MA, Society for Experimental Mechanics, 1994, pp. 549-558.

110. T. Lorentzen and A. P. Clarke, *Thermomechanically Induced Residual Strains in Al/SiC$_p$ Metal-Matrix Composites*, Composite Sci. Tech., 58 (3-4), 1998, pp. 345-353.

111. M. E. Fitzpatrick, M. T. Hutchings, P. J. Withers, *The Determination of the Profile of Macrostress and Thermal Mismatch Stress Through an Al/SiC$_p$ Composite Plate from the Average Residual Strains Measured in Each Phase*, Physica B, 213, 1995, pp. 790-792.

112. M. E. Fitzpatrick, M. T. Hutchings, P. J. Withers, *Separation of Macroscopic, Elastic Mismatch and Thermal Expansion Misfit Stresses in Metal Matrix Composite Quenched Plates from Neutron Diffraction Measurements*, Acta Mater., 45 (12), 1997, pp. 4867-4876.

113. M. E. Fitzpatrick, M. T. Hutchings, P. J. Withers, *Separation of Measured Fatigue Crack Stress Fields in a Metal Matrix Composite Material*, Acta Mater., 47 (2), 1999, pp. 585-593.

114. D. M. Knowles and J. E. King, *Influence of Macroscopic Residual Stress Fields on Fatigue Crack Growth Measurement in SiC Particulate Reinforced 8090 Aluminium Alloy*, Mater. Sci. Tech., 7, 1991, pp. 1015-1020.

115. M. E. Fitzpatrick, T. J. Downes, M. T. Hutchings, D. M. Knowles, J. E. King, P. J. Withers, *The Effect of Long-Range Thermal Residual Stress Fields on Fatigue Crack Growth in Al/SiC$_p$ Metal Matrix Composite Materials and Their Measurement by Neutron Diffraction*, in Proc. of the Fourth International Conference on Residual Stresses (ICRS 4), Baltimore, MA, Society for Experimental Mechanics, 1994, pp. 559-568.

116. D. M. Knowles, T. J. Downes and J. E. King, *Crack Closure and Residual Stress Effects in Fatigue of a Particle-Reinforced Metal Matrix Composite*, Acta Metall. Mater., 41 (4), 1993, pp. 1189-1196.

117. M. E. Fitzpatrick, M. T. Hutchings, J. E. King, D. M. Knowles, P. J. Withers, *Effect of Thermal Residual Stresses on Fatigue Crack Opening and Propagation Behavior in an Al/SiC$_p$ Metal Matrix Composite*, Metall. Mater. Trans.-A, 26 (12), 1995, pp. 3191-3198.

118. A. M. Korsunsky and P. J. Withers, *Investigation of Residual Stress Induced Crack Closure and Its Effects on Fatigue in Metal Matrix Composites*, Key Engng. Mater., 127 (1 & 2), 1997, pp. 1183-1190.

119. L. C. Davis and J. E. Allison, *Residual Stresses and Their Effects on Deformation in Particle-Reinforced Metal-Matrix Composites*, Metall. Trans.-A, 24 (11), 1993, pp. 2487-2496.

120. S. Ho and A. Saigal, *3-Dimensional Modeling of Thermal Residual Stresses and Mechanical Behavior of Cast SiC/Al Particulate Composites*, Acta Metall. Mater., 42(10), 1994, pp. 3253-3262.

CHAPTER 4: DETERMINATION OF RESIDUAL STRESSES AT THE MACROLEVEL

4.1 INTRODUCTION

In Chapter 1, it was mentioned that macrolevel residual stresses can be generated by many thermal and mechanical causes such as welding, heat treatment, plastic bending etc. One common practical problem is the deleterious effects of welding residual stresses in engineering components; for example, an occurrence of stress corrosion cracking in welded pipes or reheat cracking in the HAZ of non-stress relieved welded components in power plants, as mentioned in the previous Chapter. Reheat cracking is caused predominately by the relaxation of welding residual stress, and therefore can initiate during service if creep temperatures prevail. The presence of tri-axial stresses can substantially affect creep relaxation, void growth and the creep ductility of the material [1]. Hence a knowledge of the full residual stress tensor is essential to predict the kinetics of creep damage leading to reheat cracking. The study of macrolevel residual stresses was carried out on this interesting problem with welding residual stress.

A repair weld is frequently used to remedy weld defects found during inspection. However, repairs tend to increase the magnitude and tri-axial nature of the weld residual stress field, and therefore may increase the component's susceptibility to reheat cracking and other degradation mechanisms. The characteristic surface stress pattern induced by a short linear repair in a plate can be indicated from recent finite element studies, supported by surface measurements by Dong *et al.* [2, 3] and classical results for full depth repair welds in 19 mm thick flat plate specimens [4]. These studies show that in the longitudinal direction, tensile stresses of weld yield magnitude can be induced in the repair metal, falling sharply into compression in adjacent base material. This distribution is maintained over the whole length of the repair, but falls to near zero past the ends. Transverse stresses can also achieve tensile near-yield magnitude in the repair and have a large area of influence up to the

base material normal to the weld line. The long range tensile transverse stresses are equilibrated by pools of compression beyond each end of the repair. The through-thickness range of the transverse tensile stress field in a thick component was found by Leggatt to depend on the repair depth, repair length, and structural restraint [5]. However, yielding of parent material adjacent to the repair fusion boundary was not included in Leggatt's model. This can be important for shallow repairs where tensile stresses penetrate more than the repair depth [6] and also for thin section components. In the latter case, fully through-wall tensile transverse stresses can be induced if the repair weld heat input is sufficient to induce reverse yielding of the base metal ligament. For moderately thick structures, significant through-wall stresses are also expected [6], but this component of stress is rarely reported in the literature because of the difficulties of through-wall stress measurement in thick structures. In this study, an attempt has been made to compare the through thickness residual stress tensor in an original and a repaired girth weld in an AISI 316 stainless steel pipe using the neutron diffraction technique. The results of actual measurements have been compared with predictions of a finite element model from Nuclear Electric (now British Energy, supplier of the test components), which will also be described in this Chapter.

After the successful measurements with the 170 mm diameter pipe, a large welded component (432 mm diameter) from an ex-service pipeline in a nuclear power plant was studied at the original weld region. The results of this interesting measurement will also be presented here. But at first, details of these experiments are discussed.

4.2 EXPERIMENTAL DETAILS

4.2.1 Welded Test Components

The 170 mm Diameter Pipe

The welded test component (supplied by British Energy) was fabricated from two Sandvik SANMA316L austenitic stainless steel pipes (conforming to X2CRNIMO18143, which is equivalent to BS 3605 316S14 steel). A V-weld preparation was used and the pipes were

locally counterbored to a thickness of 20 mm. Following machining, they were solution heat treated for one hour at 1050°C and then air cooled. The pipes were welded together using a Tungsten Inert Gas (TIG) root pass and a typical Manual Metal Arc (MMA) procedure with Mitsui Babcock S3 electrodes (conforming to BS 2926 17.8.2BR). For the first four passes, 2.4 mm diameter electrodes were employed with an average heat input of 1.0 kJ/mm, followed by eight passes of 3.2 mm diameter electrodes with an average heat input of 1.9 kJ/mm. On completion of the girth weld, a cavity of 11 mm depth and 16 mm width was excavated centrally within the original weld. The excavation was 60 mm long at its deepest point and 120 mm long at the outer circumference. A total of eight passes of 2.4 mm and 3.2 mm diameter electrodes were used to fill the repair cavity. The test component geometry along with the axis definitions is shown schematically in figure 4.1.

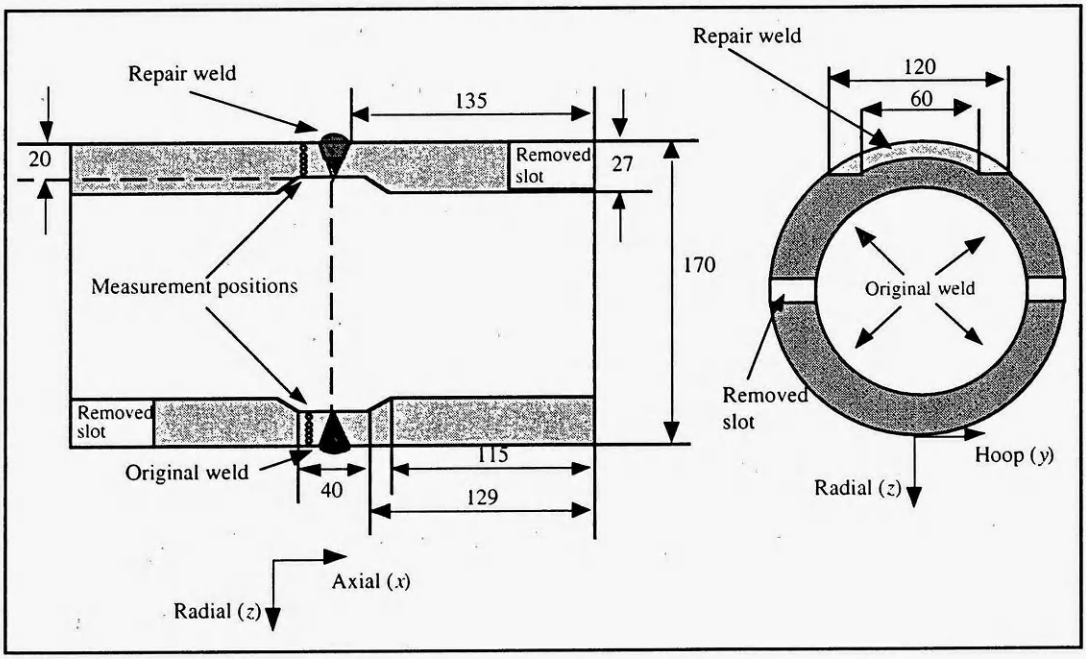

Figure 4.1: Schematic diagram of the welded component (smaller diameter pipe) and axis definition. All dimensions are in millimetres.

In order to minimise the neutron path length within the material, two slots (35 x 50 mm^2) were machined on the weld line at 90° around the circumference from the centre of the repair weld. This enabled measurements in the hoop direction to be made with the beam only passing once through the thickness of the pipe. Strain gauges were placed close to the repair weld to monitor any stress relaxation during this machining, but no significant change

(±10 micro-strain) was noticed. Similarly, sections (50 x 60 mm^2) were cut out from the two ends of the tube to ease measurements in the axial direction. Again, no discernible strain changes were recorded at the weld.

The 432 mm Diameter Pipe

For the experiments with a large diameter pipe, two pieces of ex-service AISI 316H pipes (from British Energy) of 432 mm outside diameter with a nozzle in both, were dressed to 19 mm wall thickness, solution heat treated at 1050°C for two hours and joined by a TIG butt weld. The nozzles were removed and the pipe was shortened at one end to be accommodated within the diffractometer space. The final weight of the welded pipe was 190 kg with a length of 830 mm and the position of the weld centre-line was at 350 mm from the shortened end. A slot of 30 x 90 mm^2 near the edge of the weld and at an angle of 36° from the measurement position was removed for the passage of incoming neutron beam during the hoop direction measurements. The component along with the axis definitions is schematically shown in figure 4.2.

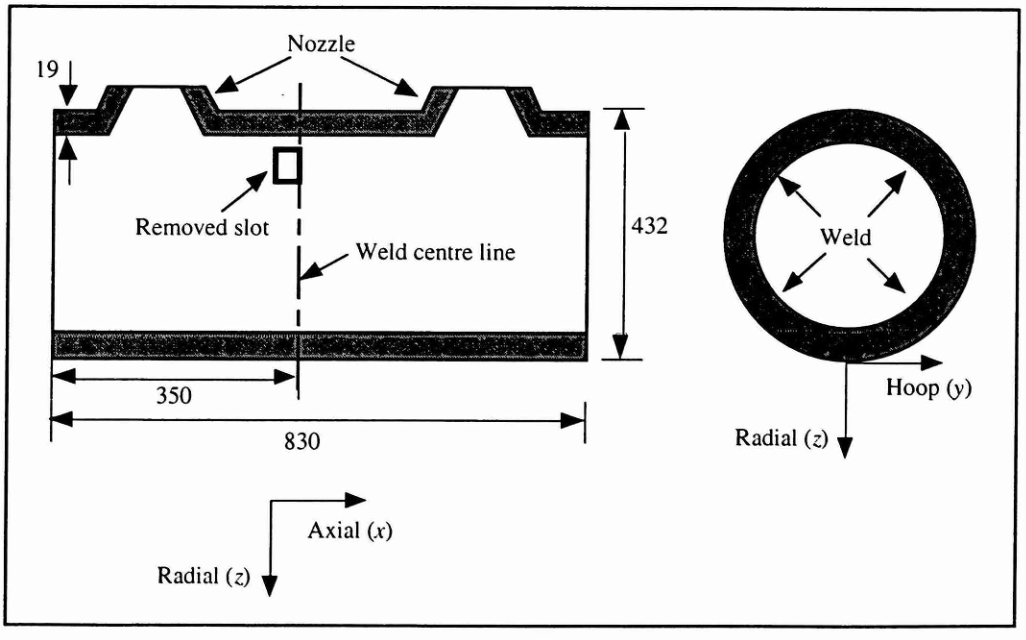

Figure 4.2: Schematic diagram of the large diameter pipe and axis definition (all dimensions in millimetres).

In order to minimise the circumferential variation in heat input, the specimen was rotated during welding to carry out welding in a fixed position. The root was made by a TIG welding using a 2.4 mm diameter filler wire (conforming to BS 2901 Part 2 316S92) and the remainder of the weld was filled by MMA welding method using varying sizes of Babcock Type S electrodes (conforming to BS 2926 19.12.3 L B R). High purity argon was used for the internal purge.

4.2.2 Experimental Set-up and Procedure

The 170 mm Diameter Pipe at ISIS

The measurements with the smaller diameter pipe were carried out at the ENGIN spectrometer of ISIS at the Rutherford Appleton Laboratory, UK. The general set-up of the instrument has already been shown in Chapter 2 (figure 2.2). All measurements were performed at the centre of the circumferential arc of the repair weld and in the original girth weld diametrically opposite to each other; that is, on a single diametral-axial plane that symmetrically bisects the tube. Measurement points on this plane were positioned with respect to the inner wall of the pipe and the radial centre-line of the weld, as shown in figure 4.3.

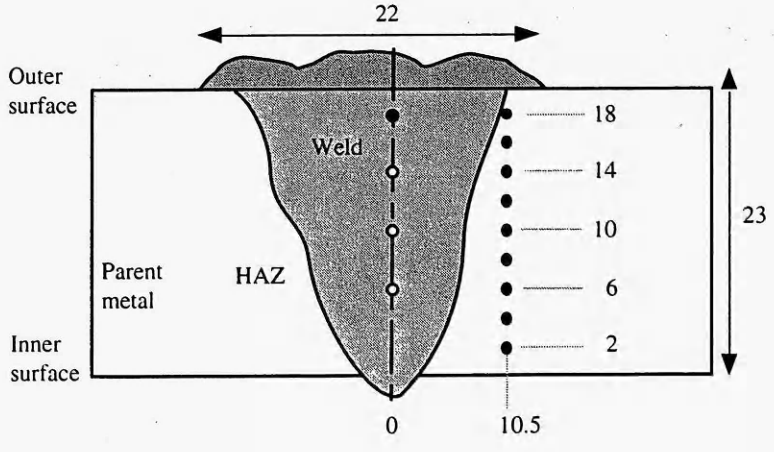

Figure 4.3: Measurement positions with respect to the weld centre-line and inner surface: all circles for the original weld and only closed circles for the repair weld. All dimensions are in millimetres.

Through thickness measurements in the hoop, axial and radial directions were made at the weld centre-line, and in the heat affected zone, *i.e.* 10.5 mm away from the weld centre-line, as shown in figure 4.3. However, owing to lack of neutron beam time only one measurement was performed in the repair weld fusion zone. The hoop and radial measurements were performed simultaneously with the pipe placed vertically whilst the axial measurements were performed with the pipe placed horizontally on a specially-made support block. The measurement positions were determined by first aligning the specimen with the help of two telescopes. The precise locations were then confirmed by using the intensity of the diffracted beam as the gauge volume enters the specimen [7, 8]. The incident neutron beam was collimated to 3 x 3 mm^2. The focal width of the radial detection collimators used was 1.6 mm. A photograph of the component on the ENGIN spectrometer is shown in figure 4.4.

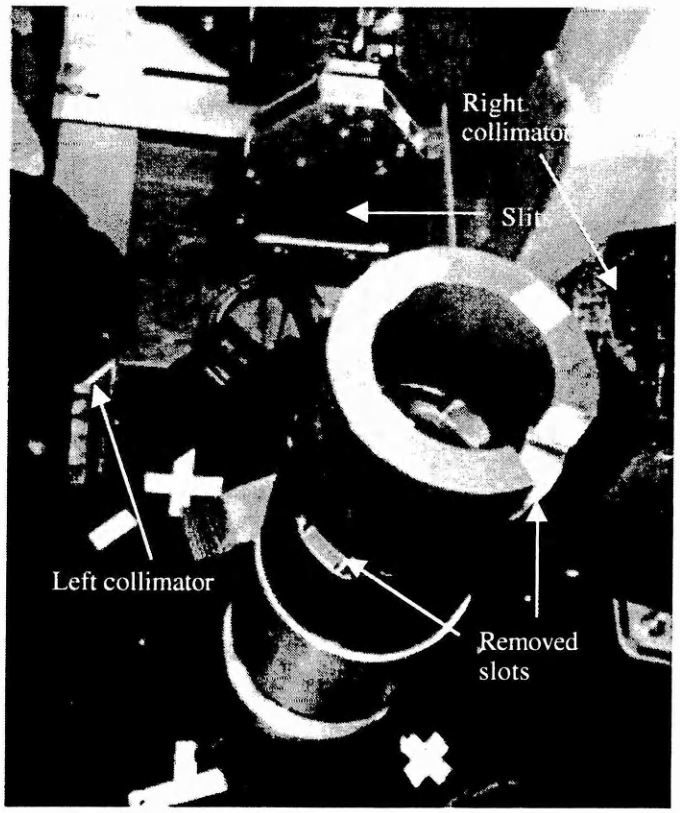

Figure 4.4: Photograph of the small diameter pipe on the ENGIN spectrometer. The component is set for the measurements in hoop and radial directions.

As noted earlier the ENGIN spectrometer uses the time of flight technique for the measurement of strain. Analysis of the resulting time of flight spectrum produces a lattice

parameter a, which is obtained by fitting all the detectable peaks using the Rietveld refinement technique [9] (modified Pawley fitting). It has been shown that the strain calculated from a Rietveld refinement is a good approximation to the engineering strain in the component, and is not significantly affected by either elastic or plastic anisotropy present in the material [7, 10].

The 432 mm Diameter Pipe at Studsvik

The measurements with the large diameter pipe were performed at the REST spectrometer of the R2 reactor of NFL (Laboratory for Neutron Scattering) in Studsvik, Sweden. Some specific details of this reactor source spectrometer have been mentioned in Chapter 2. The scattering angle for the chosen peak (311) at the selected wavelength of ~1.76Å was 108.6°. Mounting and alignment of this large component within the limited space of the spectrometer was difficult. The pipe was always held by a crane to partially relieve its load from the positioning table and fixed to the table with the help of either wedges and belt or clamps and counterbalances. The measurements in the hoop direction were performed with pipe in an upright position after removing the sample z-stage (figure 4.5); whereas the pipe was kept horizontal on the positioning table fitted with wedges for measurements in other two directions (figure 4.6).

The hoop measurements were carried out by allowing the incoming beam to pass through the cut slot and positioning the primary slit within the pipe, as shown in figure 4.5. During the axial measurements, the diametrical plane was slightly lower than the scattering plane as the pipe was rotated by 15° for the access of the primary slit within the pipe. This produced the same distance between the specimen and primary slit and thus the same experimental condition was maintained.

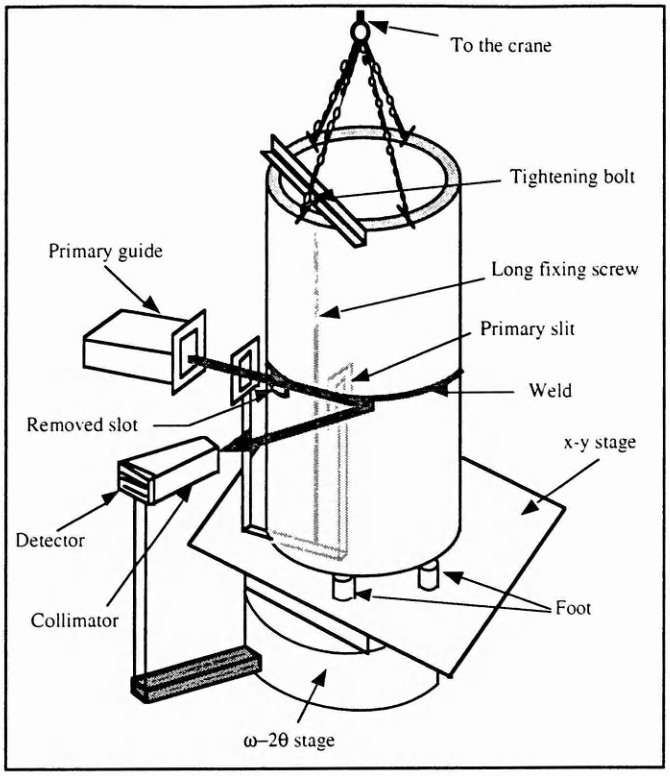

Figure 4.5: Sketch of the experimental set-up for measurements in the hoop direction in the welded component (large diameter pipe) at NFL, Studsvik.

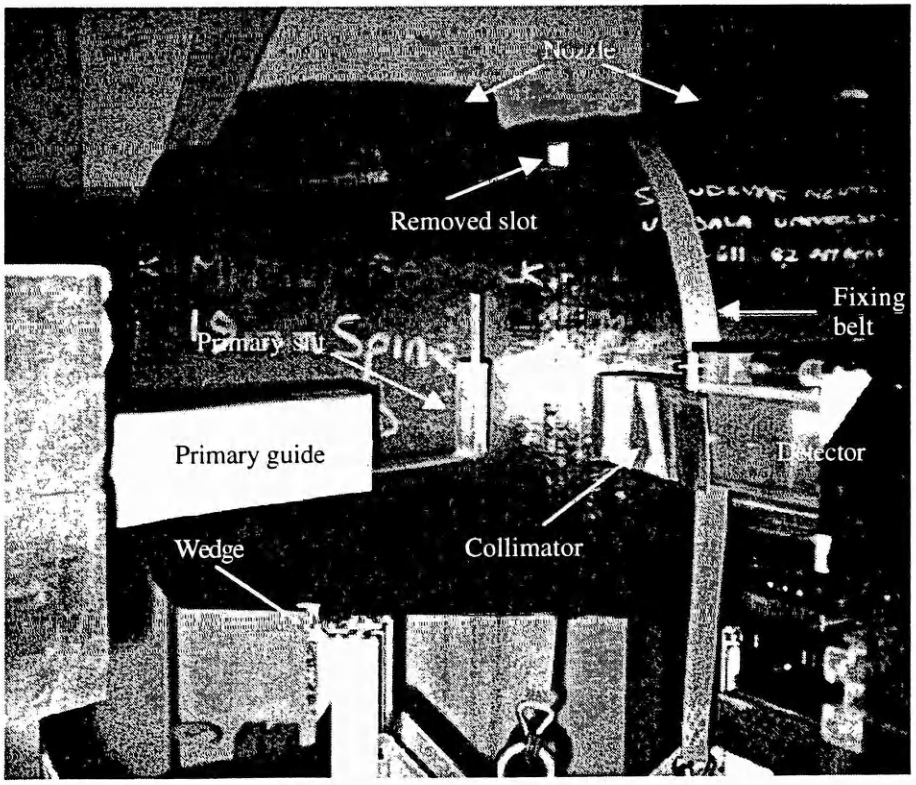

Figure 4.6: Photograph of the large diameter pipe on the REST spectrometer at NFL, Studsvik. The component is set for the measurements in the radial direction.

The width of the primary slit was the same (3 mm) for all measurements; whereas the height varied as 3 mm for the hoop direction and for the small reference cubes (d_0 measurements); 5 mm for the axial measurements; and 10 mm for the radial measurements. A double focusing monochromator is used at REST where both horizontal and vertical divergences play an important role in the resolution function. Three calibration runs were required to assess the correct wavelength in each case. The scans were performed with iron powder (a standard for NFL), measured at three different reflections (namely the (200), (211) and (220)). The exact wavelengths were found to be:

$\lambda = 1.75952 \pm 4 \times 10^{-5}$ Å for 3x3 mm^2 slit with an offset angle of $2\theta_0 = 0.156^\circ \pm 0.003^\circ$

$\lambda = 1.75984 \pm 3 \times 10^{-5}$ Å for 3x5 mm^2 slit with an offset angle of $2\theta_0 = 0.138^\circ \pm 0.003^\circ$

$\lambda = 1.75979 \pm 3 \times 10^{-5}$ Å for 3x10 mm^2 slit with an offset angle of $2\theta_0 = 0.131^\circ \pm 0.003^\circ$.

These offsets are critical for the evaluation of the strains since they are different for the three different measurement configurations. The alignment of the component and exact positioning was done with the help of a telescope and by neutron surface scanning. Measurements were performed both in the weld and in HAZ through the thickness as shown in figure 4.7; positions were determined in reference to the inner surface of the pipe. The exact configuration of this 'V' shaped weld is not yet known as the specimen is yet to be destructively sectioned. The innermost two measured points on the weld line were probably outside the weld; whereas, the outermost point in the HAZ could be at the weld edge.

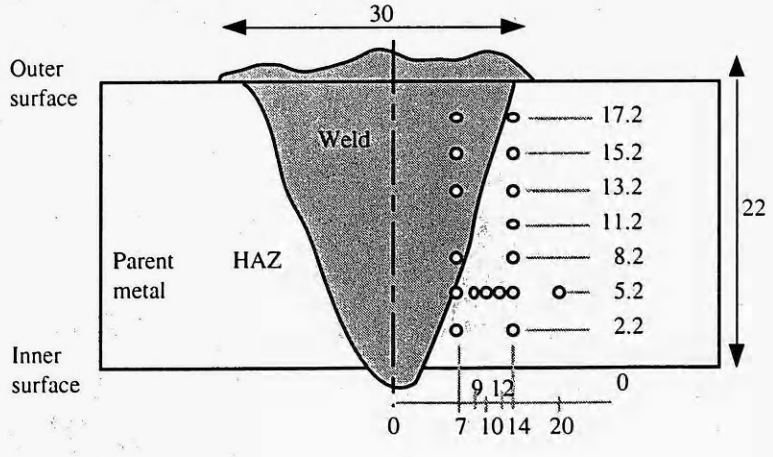

Figure 4.7: Measurement positions in the large pipe with respect to the weld centre-line and inner surface. All dimensions are in millimetres.

A transverse scan from the weld (or probably just beside the weld edge in the HAZ) up to the parent material was also performed at 5 mm from the inner surface. As can be seen in the previous figure, the thickness of the pipe at the measured position in the HAZ *i.e.* at 14 mm from the weld centre-line was 22 mm. The gauge volume was always kept completely immersed in the material.

4.2.3 Strain Free Reference

The 170 mm Diameter Pipe

The determination of a suitable stress free lattice parameter is often problematic in neutron measurements. This is particularly so with weldments owing to the compositional gradient typically found in the fusion zone and the HAZ. A constant stress free lattice parameter has been used in the analysis of the small diameter pipe, which was obtained by making measurements at different points through the thickness of a block ($50 \times 60\ mm^2$) cut from one end of the tube. No significant variation in lattice parameter was observed through the thickness of the tube and the results were averaged to produce a stress free lattice parameter value for each collimator.

However, the necessary corrections resulting from these measurements are not expected to be large. In a recent ISIS experiment, Withers [11] studied the variation in stress free lattice parameter across a similar stainless steel pipe butt weld by measuring stress free matchsticks, $2 \times 2 \times 16\ mm^3$ in size, taken from various parts of the component. The results showed that the variation was small (spread of ±50 micro-strain) throughout the heat affected zone and base metal. Thus the use of a single stress free lattice parameter for these regions would not introduce a noticeable error into the analysis. However, the measured variation in the weld fusion zone was larger, varying from 50 to 400 micro-strain across the weld, which could lead to errors of up to 80 MPa in the calculated stress.

For the large pipe, small cubes of 3 x 3 x 3 mm^3 were cut from a ring core specimen drilled (at British Energy) at 150° away from the measurement location, which represents material from all regions *i.e.* weld pool, HAZ and the parent material. Cubes from each region were scanned in four directions *i.e.* in the axial and hoop directions from both sides (positive and negative) to minimise the errors arising from misalignments of these tiny cubes. The averages of these inter-planar distance values (d_0) were found to be virtually identical in both the parent material and the HAZ, similar to the results of Withers [11], as discussed earlier. However, higher scatter was found amongst the average values in the weld pool. The average value at a particular point was used as the strain free reference (d_0) in determining the strain values at that point. The d_0 was also calculated considering the axial stress balance condition for the cylindrical geometry, *i.e.*

$$\int_T \sigma_a r \mathrm{d}r = 0 \qquad \text{(Equation 4.1)}$$

where T is the thickness and r is the radial co-ordinate of the point. This assumes that the weld is axi-symmetric. In our case the measured points did not cover the whole thickness, so an extra value was extrapolated at the outer layer (at 20 mm from the inner surface), and the values obtained for the reference are:

$d_{0(311)}$ = 1.08209 ± 6 x 10^{-5} Å in the HAZ and $d_{0(311)}$ = 1.08214 ± 7 x 10^{-5} Å in the weld. They are slightly different from the measured averages on the cubes.

4.3 RESULTS: THE 170 mm DIAMETER PIPE

The strain value for each measured point in the original and repair weld regions was obtained by comparing the respective lattice parameters with that of the strain free reference, as described in Chapter 2. The full stress tensor was calculated for all the measured points, assuming that the hoop, axial and radial directions were the principal stress axes. Given the symmetry of the component this is likely to be a reasonable assumption. In these calculations, the values for the (bulk average) modulus of elasticity (E) and the Poisson ratio (ν) were considered as 200 GPa and 0.3 respectively. Errors are given for all

measurements, but it should be noted that the actual uncertainty in the fusion zone measurements may be slightly higher owing to possible variations in the stress free lattice parameter arising from local chemistry effects and texture. The measured strains and calculated stresses both in original and repair welds will be presented in this section.

4.3.1 Measured Strain

All measured strains at 10.5 mm away from the weld centre-line (*i.e.* at the HAZ) in the three principal directions through the thickness are shown in figure 4.8 for the original weld and in figure 4.9 for the repair weld. Uncertainties for all measured strains are also shown in the form of error bars. In the original weld, general tension in the hoop direction and compression in the axial direction can be observed; whereas the radial strain does not change much through the thickness. The tensile nature of the hoop strain gradually increases from the inner surface to the outer surface.

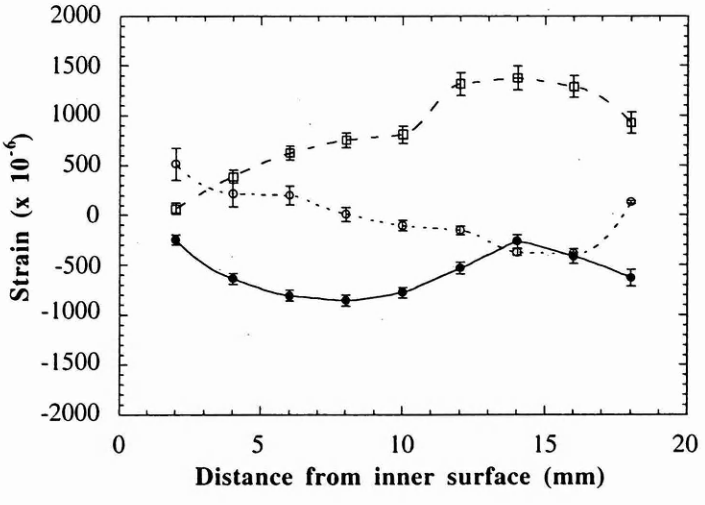

○: radial strain; □: hoop strain; ●: axial strain

Figure 4.8: Measured through-thickness strains at the HAZ (10.5 mm away from the weld centre-line) of the original weld in the three principal directions. Lines are guides for the eye.

Significant changes occurred in the strain profiles on repairing the weldment as seen in figure 4.9. The axial strain becomes tensile and the radial strain goes into compression. The variation in strain values through the thickness has reduced in all three directions making the profiles more flat.

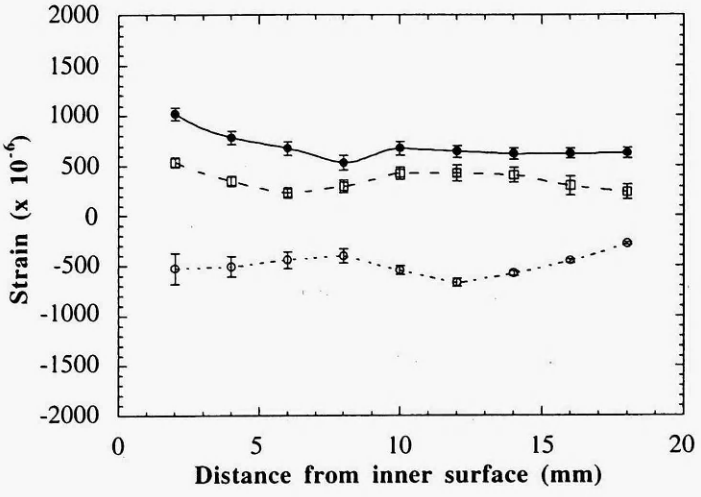

○: radial strain; □: hoop strain; ●: axial strain

Figure 4.9: Measured through-thickness strains at the HAZ (10.5 mm away from the weld centre-line) of the repair weld in the three principal directions. Lines are guides for the eye.

The strain values measured at the middle of the weld in all three principal directions through the thickness are shown in figure 4.10. The profiles are similar to those observed in the original weld HAZ, although a greater variation in the axial strain can be found in this case.

In all the above figures, a noticeable point is that the error in radial strains increases from the outer surface to the inner surface. This is due to attenuation; both the incoming and outgoing beam had to traverse further through the material as the measurements advanced towards the inner surface. The beam path within the material is constant for all measurement points in the hoop and axial directions unless the beam passed through the weld beads.

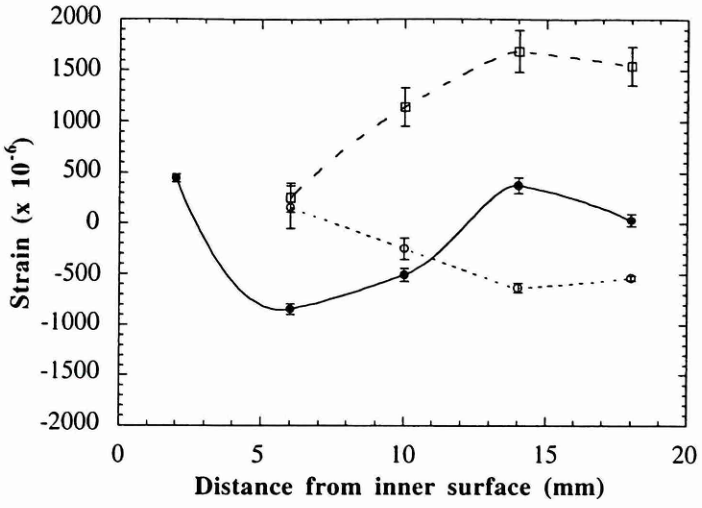

○: radial strain; □: hoop strain; ●: axial strain

Figure 4.10: Measured through-thickness strains at the weld centre of the original weld in three directions. Lines are guides for the eye. (Due to shortage of time the point at 2 mm away from the inner surface could not be measured for the radial and hoop directions.)

4.3.2 Calculated Stress

The measured through-thickness variation of residual stress in the original girth weld, diametrically opposite the repair, is given in figure 4.11 for the HAZ positions and figure 4.12 for the weld fusion zone. Both hoop stress profiles peak at 14 mm from the inner surface with a maximum value of 299 MPa (nearly equal to the 1% proof stress of base metal) in the HAZ and 427 MPa (nearly equal to the 0.2% proof stress of weld metal) being found in the weld fusion zone. The measured axial stresses in the HAZ exhibit a roughly sinusoidal distribution (compressive towards the inner surface and tensile towards the outer), with a superimposed compressive membrane stress (mean value through the thickness) equal to about –55 MPa. The radial stresses are generally low (<73 MPa tension), apart from the innermost HAZ value of 120 MPa. But the larger error (±55 MPa) for radial measurements towards the inner surface should be noted as already mentioned in the previous section.

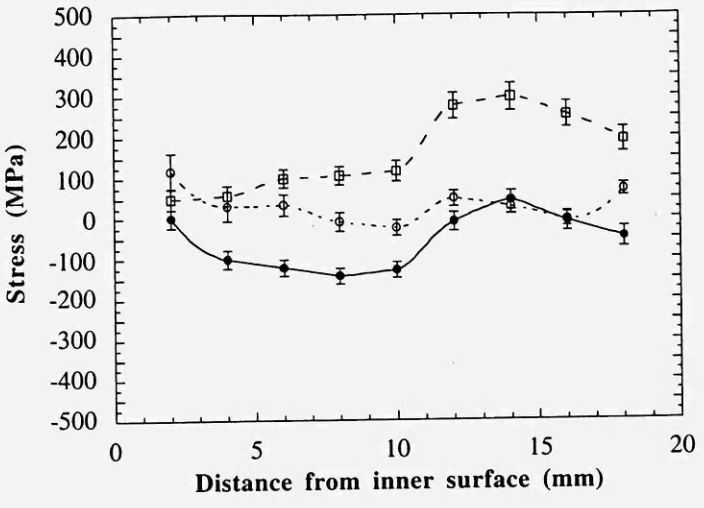

○: radial stress; □: hoop stress; ●: axial stress

Figure 4.11: Measured through-thickness stress at the HAZ (10.5 mm away from the weld centre-line) of the original weld in the three principal directions. Lines are guides for the eye.

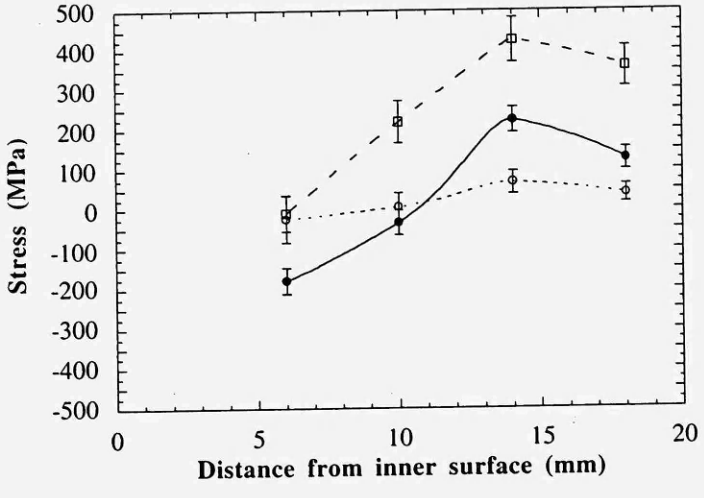

○: radial stress; □: hoop stress; ●: axial stress

Figure 4.12: Measured through-thickness stress at the weld centre of the original weld in the three principal directions. Lines are guides for the eye.

The through-thickness variation of residual stress in the HAZ adjacent to the repair weld is shown in figure 4.13. The repair treatment generates a sharp rise in axial stresses from their initial values in the original weld. All three components of stress show a similar membrane profile. The axial component is the largest, having an average tensile magnitude equal to

173 MPa, which is about 65% of the base metal 0.2% proof stress. Radial stresses through the whole thickness are small (from –54 MPa to 40 MPa).

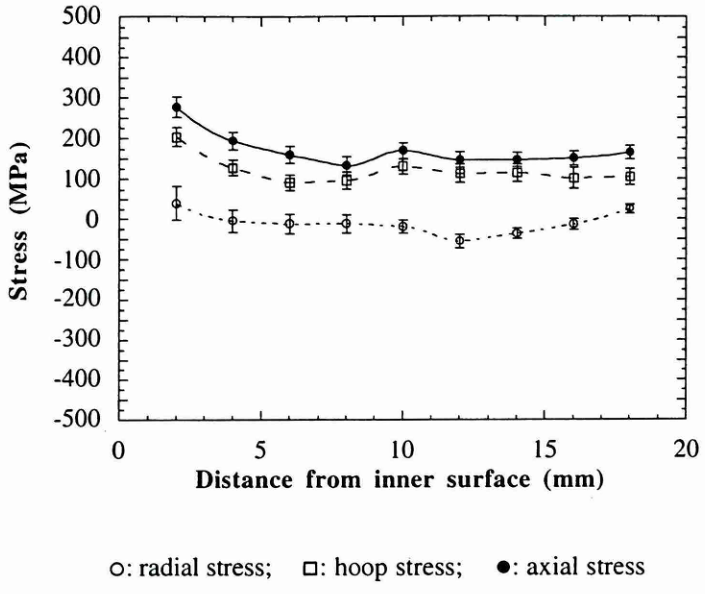

Figure 4.13: Measured through-thickness stress at the HAZ (10.5 mm away from the weld centre-line) of the repair weld in the three principal directions. Lines are guides for the eye.

The measured compressive axial membrane stress in the original weld, compared to the high tensile one in the repair weld, suggests that introduction of the repair weld during fabrication induced a global bending of the pipe. This bending effect was also observed at 17.5 mm from the weld centre-line measured earlier [12]. An alternative explanation is that the net membrane stress indicates an error in the stress free lattice parameter. The accuracy of the stress free lattice parameter used for the present assessment will be checked in future work (at the next available beam time), by examining small coupons extracted from the measurement locations. Finally, the variation in residual stress with distance from the weld centre-line, at 2 mm from the outer surface, is shown in figure 4.14(a) for the original weld and figure 4.14(b) for the repair weld. The values for the 17.5 mm position are taken from a previous measurement in the same component [12].

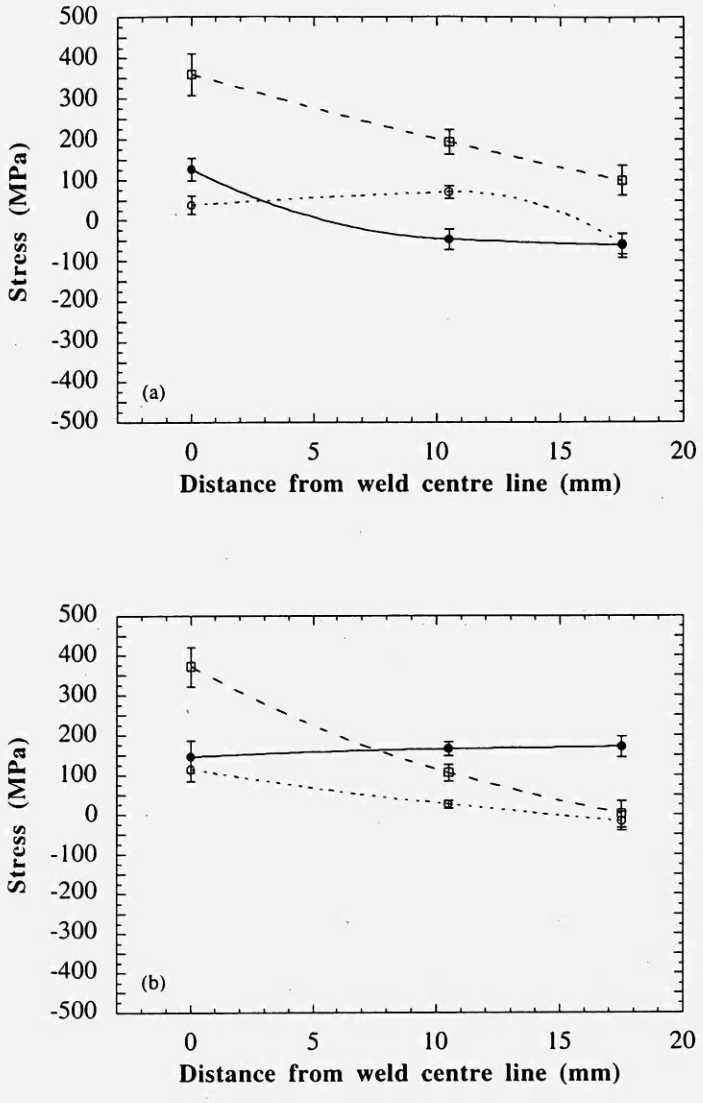

Figure 4.14: Stresses at 2 mm from the outer surface as a function of distance from the weld centre-line in (a) the original weld and (b) the repair weld. Interpolated lines are guides for the eye. The data for the 17.5 mm position are taken from a previous measurement [12].

It can be noticed that the highly tensile hoop stresses at the weld gradually relax towards the parent material. Radial stresses are small in both the original and repair welds. Significant changes of the axial stresses from compression to tension at the far field owing to the repair treatment are also apparent. This suggests an overall bending effect on the pipe arising from the repair treatment.

4.4 RESULTS: THE 432 mm DIAMETER PIPE

The strain values at each measured point in the three principal directions (axial, hoop and radial) were determined by comparing the peak shifts (or the change in inter-planar distance, Δd) with respect to the peak positions in the strain free reference cubes (or d_0 values from the cubes or the average d_0 value from the stress balance condition). Given the symmetry of the component, it was assumed that these three directions were also the principal stress axes and thus the full stress tensor was calculated using the measured strain values. For these reactor source single peak (311) measurements a value of 193 GPa was used for the modulus of elasticity (E) and 0.3 for the Poisson ratio (ν) in the stress calculations.

4.4.1 Measured Strain

The measured strains through the thickness of the component in the three principal directions are shown in figure 4.15 for the positions at the HAZ and figure 4.16 for the positions in the weld pool.

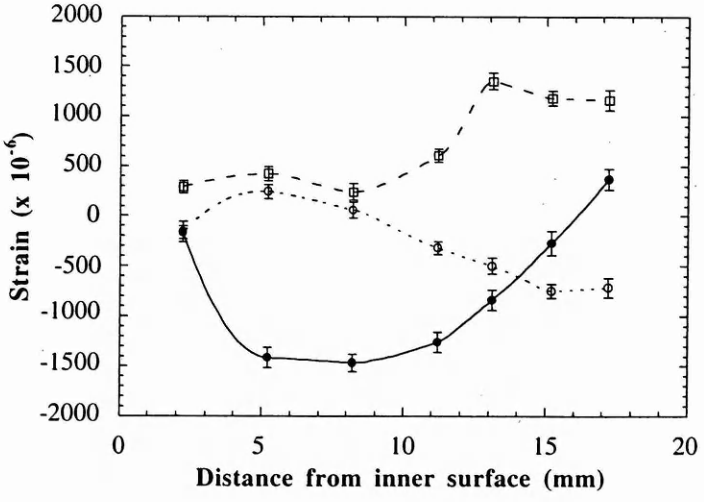

Figure 4.15: Measured through-thickness strains in the three principal directions at the HAZ of the large pipe (the last point towards the outer surface might be at the edge of weld). Lines are guides for the eye.

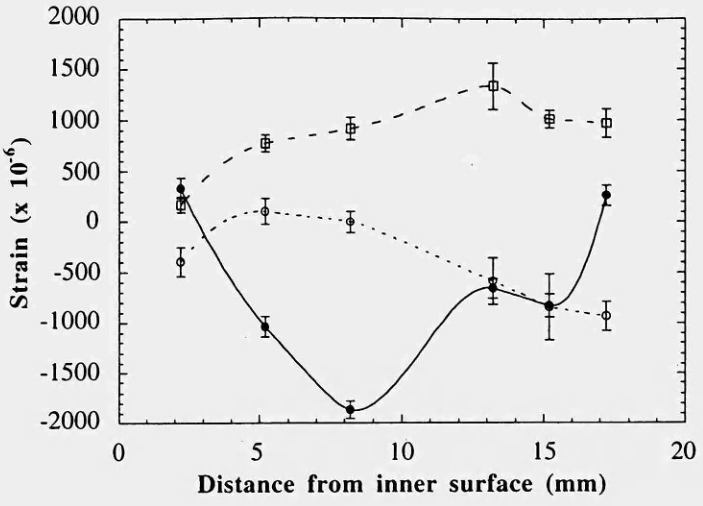

○: radial strain; □: hoop strain; ●: axial strain

Figure 4.16: Measured through-thickness strains in the weld of the large pipe in the three principal directions (at 7 mm away from the weld centre-line; the innermost two points might be outside the weld). Lines are guides for the eye.

As mentioned earlier, the last point toward the outer surface at the HAZ was probably just at the edge of the weld and the innermost two points in figure 4.16 are possibly outside the weld. The through-thickness strain profiles are similar in the two regions, except that a greater variation in axial strain is present in the weld, which was also seen in the smaller pipe. A large amount of tension can be observed in the hoop direction, particularly towards the outer surface in both the HAZ and weld. The axial component goes into compression from both surfaces towards the mid-thickness. The peak value is larger in the weld. The radial strain maintains a low profile throughout the thickness in both regions.

The results of the transverse strain measurements from the weld edge to the parent material at 5 mm from the inner surface are shown in figure 4.17. In the hoop direction, the high tension at the weld edge decreases continuously through the HAZ and becomes negligible in the parent material. The same is true for the radial strain although the initial strain value at the weld edge is much smaller than the hoop strain. The axial strain is always in compression, even in the parent material at a distance of 20 mm away from the weld centre-line.

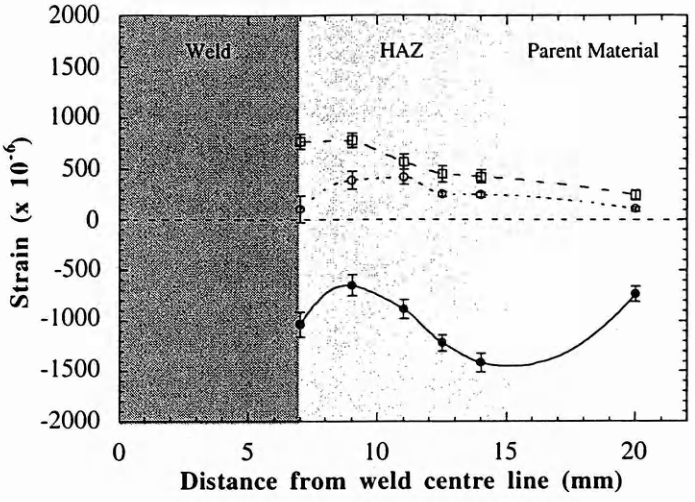

Figure 4.17: Measured transverse strains from the weld edge to the parent material in the three principal directions. The end positions of the weld zone and HAZ are estimates. Lines are guides for the eye.

4.4.2 Calculated Stress

Using the Strain Free Reference (d_0) from the Cubes

The calculated through-thickness stresses in the three principal directions, assumed to be coincidental with the axial, hoop and radial directions, are presented in figure 4.18 for the HAZ and figure 4.19 for the weld region. The hoop stress at the HAZ is small at the inner half of the thickness where it alters in sign from positive to negative. Then it rapidly increases towards the outer surface reaching its peak (just over 200 MPa) at about 13-14 mm from the inner surface, as also found in the smaller pipe. The outermost point with the highest value of ~250 MPa is probably in the weld or at the weld edge, as mentioned earlier. The axial stress is generally in compression, again with the exception of the outermost point. The peak compressive value of ~–350 MPa is observed at about 8 mm away from the inner surface. The radial stress is slightly compressive in nature throughout the thickness.

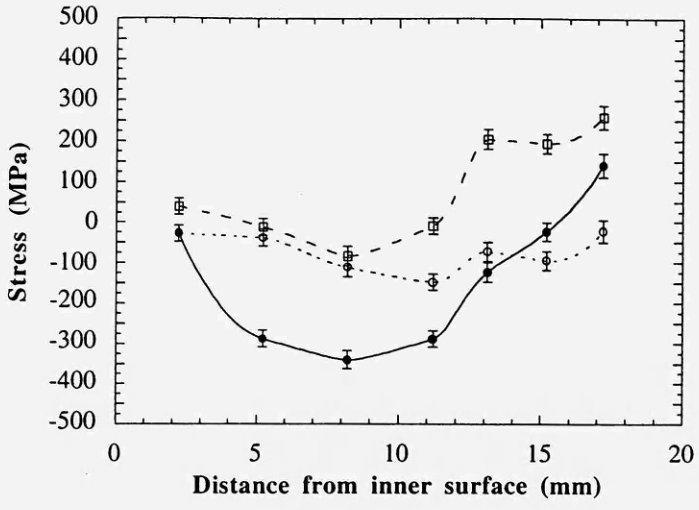

○: radial stress; □: hoop stress; ●: axial stress

Figure 4.18: Calculated through-thickness stresses in the three principal directions at the HAZ using the measured cube d_0 values (the last point towards the outer surface was at the edge of weld). Lines are guides for the eye.

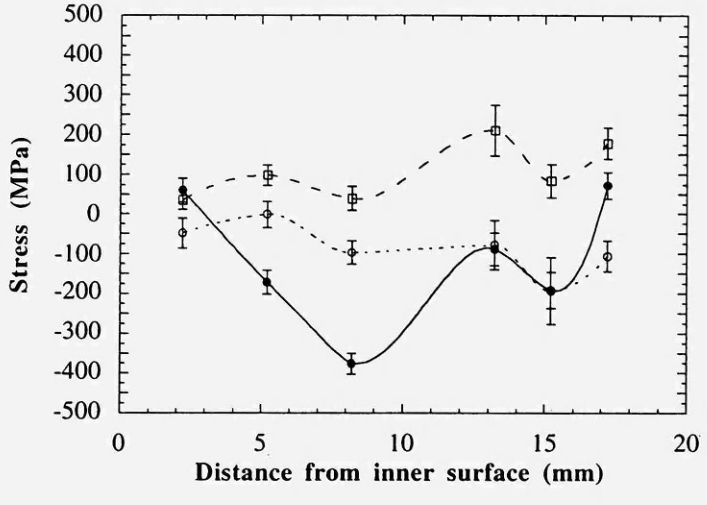

○: radial stress; □: hoop stress; ●: axial stress

Figure 4.19: Calculated through-thickness stresses in the three principal directions in weld (at 7 mm away from the weld centre-line; the innermost two points might be outside the weld) using the measured cube d_0 values. Lines are guides for the eye.

A similar tensile nature in the hoop stress and compressive nature in axial and radial stresses are also seen in the weld (figure 4.19). But all of them vary considerably through the thickness. A similar peak tensile hoop stress (~200 MPa) is observed at the same position

(13-14 mm away from the inner surface); and the peak compressive axial stress of almost –400 MPa exists at 8 mm away from the inner surface.

Finally, the transverse stresses measured at 5 mm away from the inner surface from the weld edge up to the parent material are shown in figure 4.20. It is interesting to note that the tensile nature of both hoop and radial stresses gradually reduces with distance from the weld centre-line and they completely relax within the HAZ, at a distance 12-14 mm away from the weld centre-line. But the compressive axial stress spreads over a greater distance, and attains its peak at the end of the HAZ (~15 mm away from the weld centre-line). A long range relaxation in the axial stress is apparent from the figure. The stress values for the first point (at the weld edge) seem to be incorrect in all directions; all of them should move upward. The reason is probably an erroneously high estimation of the d_0 value from the small coupon at that position.

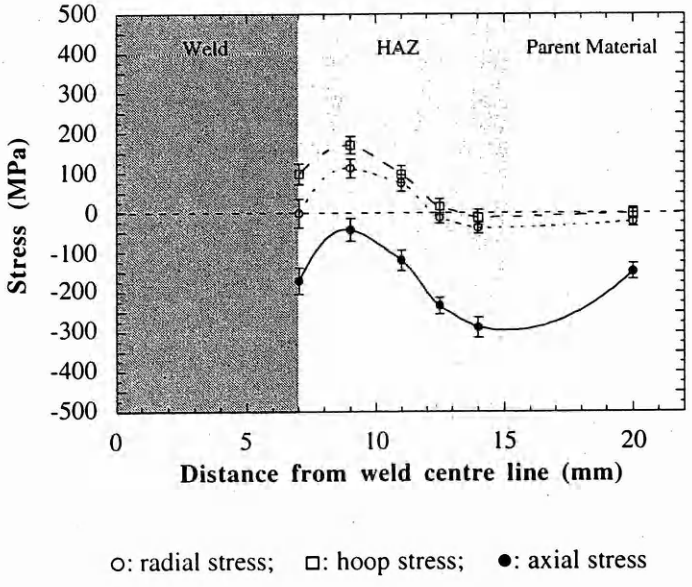

Figure 4.20: Calculated transverse stresses from the weld edge to the parent material in the three principal directions, using the measured cube d_0 values. The end positions of the weld zone and HAZ are estimates. Lines are guides for the eye.

Using the Strain Free Reference (d_0) from the Stress Balance Condition

Considering the possible inaccuracy arising from measuring the tiny ($3 \times 3 \times 3$ mm^3) coupons with a 3×3 mm^2 beam dimension, which was reflected with a large scatter in weld

d_0 values, an axial stress balance condition was also considered to determine the average d_0 values for the weld zone and the HAZ as described earlier. The calculated stresses in the three principal directions using this average d_0 from the stress balance condition are shown in figures 4.21 and 4.22 for the HAZ and weld zone respectively.

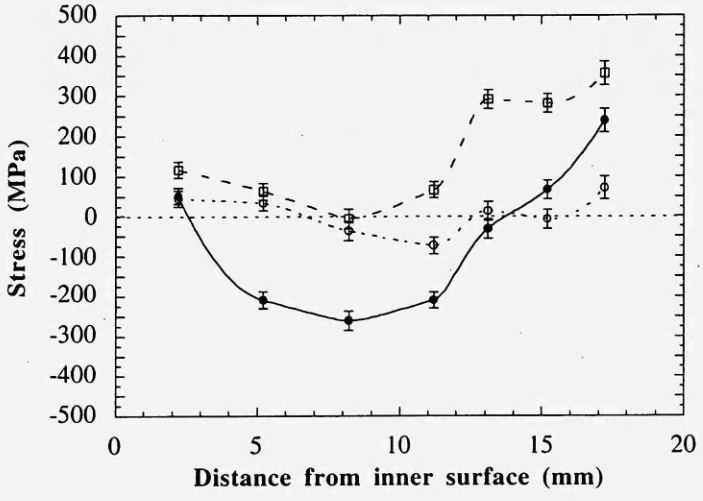

○: radial stress; □: hoop stress; ●: axial stress

Figure 4.21: Calculated through-thickness stresses in the three principal directions at the HAZ using the stress balance condition (the last point towards the outer surface was probably at the edge of weld). Lines are guides for the eye.

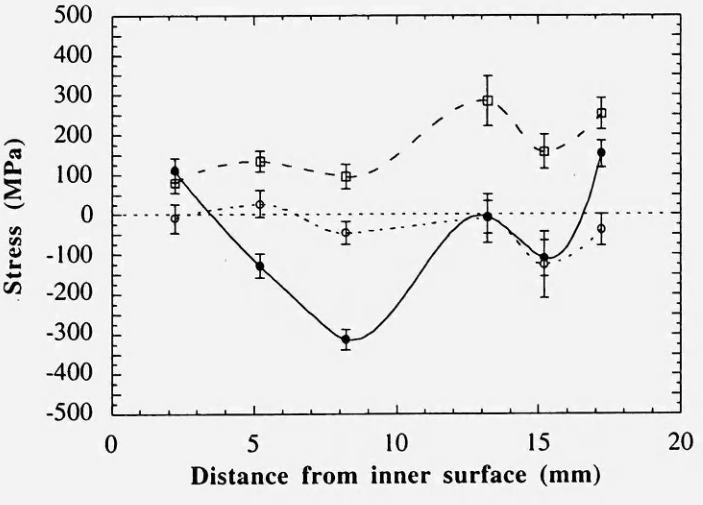

○: radial stress; □: hoop stress; ●: axial stress

Figure 4.22: Calculated through-thickness stresses in the three principal directions in the weld (at 7 mm away from the weld centre-line; the innermost two points might be outside the weld) using the stress balance condition. Lines are guides for the eye.

An overall upward shift (of about ~60 MPa) in all stress values from those obtained using the measured cube d_0 values, is observed in this case. Therefore, the tensile nature of the hoop stress has increased; whereas the axial stress at the mid-thickness has become less compressive in both the HAZ and the weld zone. The through-thickness radial stress is now close to zero. An initial finite element calculation performed by British Energy has shown a better agreement with the stresses calculated from the stress balance condition [13].

A significant change in the transverse stress profiles are obtained with this stress balance condition, as can be noticed by comparing figures 4.23 and 4.20. All the stress profiles have become more flat with less stress variation through the HAZ . The radial stress seems to be almost constant and close to zero.

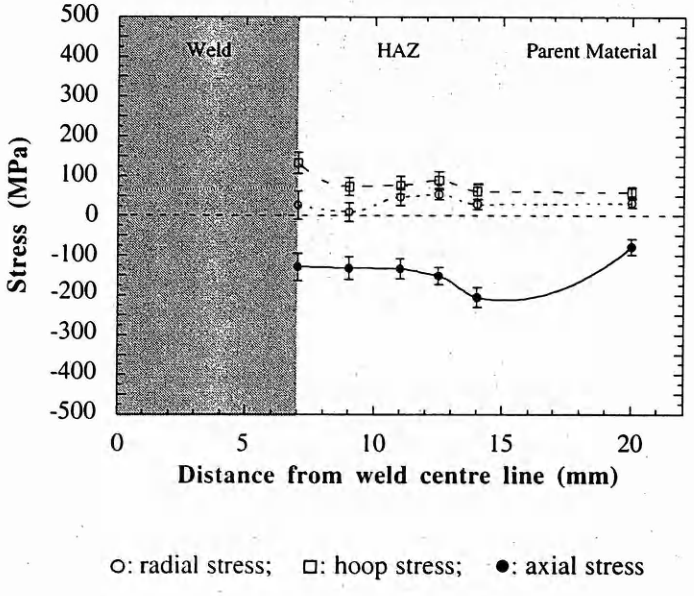

Figure 4.23: Calculated transverse stresses from the weld edge to the parent material in the three principal directions using the stress balance condition. The end positions of the weld zone and HAZ are estimates. Lines are guides for the eye.

4.5 COMPARISON BETWEEN PREDICTED AND MEASURED RESIDUAL STRESSES FOR THE ORIGINAL GIRTH WELD IN THE SMALL PIPE

A numerical weld simulation was performed independently by British Energy using the ABAQUS finite element code [14] to predict the residual stress field in the test component girth weld, that is prior to the introduction of the repair. This involved a thermal calculation to predict the multi-pass weld temperature history at any point in the model, followed by a sequential non-linear mechanical analysis. Thermal and mechanical properties for type 316 stainless steel up to melting temperatures were employed in these analyses. The details of the finite element analysis will not be discussed here as it is out of the scope of the present work.

The axi-symmetric finite element model used (Figure 4.24) provided a good representation of the test component geometry, weld preparation and weld bead lay-up. The slightly smaller thickness (19 mm) adjacent to the weld cap and absence of a counterbore in the model were judged to have a small effect on the residual stress field in the region of the weld.

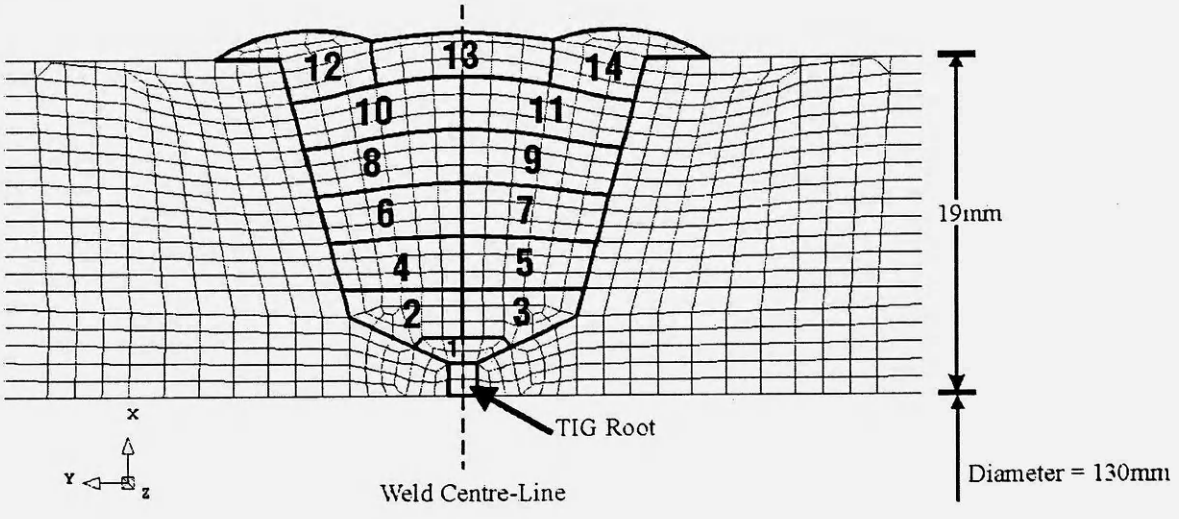

Figure 4.24: Finite element model for original girth weld simulation performed independently by British Energy.

The predicted hoop residual stresses from this model are shown in Figure 4.25. The stresses in the vicinity of the weld are influenced by the weld pass sequence. For example, a zone of high hoop stress is predicted immediately below the final capping pass. Thus the

final residual stress field is asymmetric about the weld centre-line, as can be observed at the 10.5 mm positions.

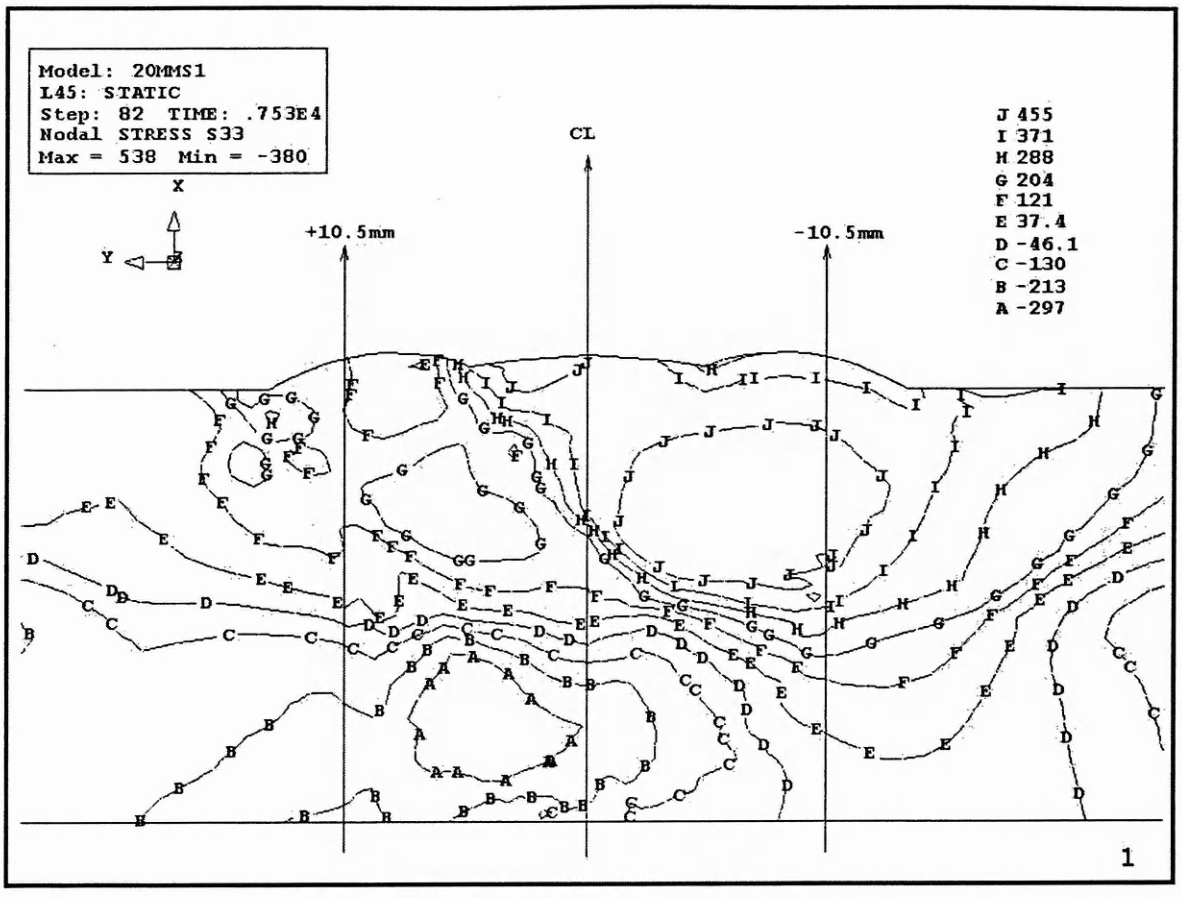

Figure 4.25: FE predicted residual stresses in the hoop direction in the original girth weld.

The measured through-wall residual stresses in the hoop direction at the original girth weld are compared with finite element predictions in figure 4.26, both at the weld centre-line and in the HAZ. The predicted HAZ stresses at the −10.5 mm position are most relevant as these correspond to the last capping pass, where the neutron measurements were made. Predicted stresses from the +10.5 mm side are shown to illustrate the asymmetry arising from weld pass sequence effects. Overall, the correspondence between measured and predicted stress is impressive, particularly in the weld where d_0 errors arising from anisotropy and chemistry effects might be expected to distort the measured results.

Both the measured and predicted hoop stresses demonstrate the same through-wall profile in both the weld fusion zone and HAZ; that is, exhibiting a peak at about 6 mm below the outer surface (that is 14 mm from the inner surface) and a falling trend towards the inner surface.

This characteristic profile is a global effect caused by the hoop contractions of outer weld passes applying a tourniquet compressive load on earlier passes. In the HAZ, it is evident that the predicted hoop stresses exceed those measured, particularly towards the outer surface. This conservative predictive feature has been observed in other weld analyses using similar modelling techniques and is the subject of on-going development work within British Energy [13].

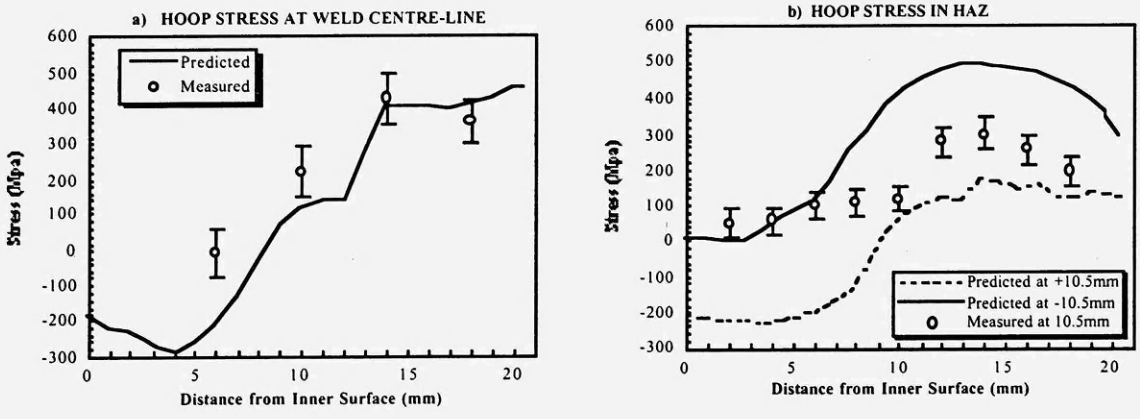

Figure 4.26: Comparison of measured and predicted through-thickness hoop residual stress at 10.5 mm away from the weld centre-line in the (a) weld and (b) HAZ of the original girth weld.

The agreement between measured and predicted axial stress profiles is equally good (see figure 4.27). The measured profile in the HAZ shows the same sine wave characteristic predicted by the finite element model below the last capping pass. This type of profile is typical for pipe girth welds where the heat input per unit thickness (Q/t) is less than around 100 J/mm^2 [15]; note that for the main filler passes of the test weld, $Q/t = 95$ J/mm^2. The axial stress comparison also highlights the presence of a net measured compressive membrane stress of about –55 MPa, which is probably associated with global bending induced by the repair weld procedure.

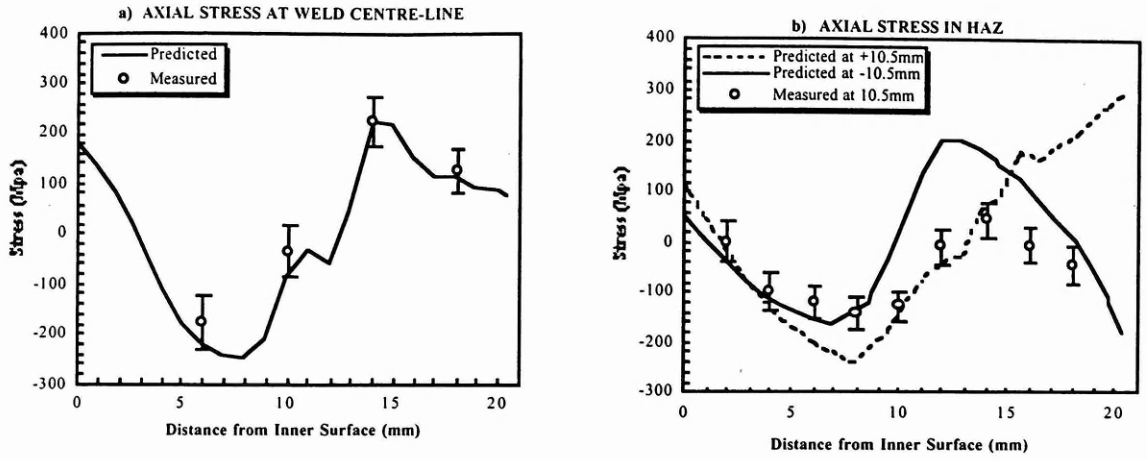

Figure 4.27: Comparison of measured and predicted axial residual stress at 10.5 mm away from the weld centre-line in the (a) weld and (b) HAZ of the original girth weld.

4.6 DISCUSSION

4.6.1 Residual Stresses in Multipass Welded Pipes

The residual stresses in an austenitic stainless steel weldment generate principally from the shrinkage of fused metal at the weld and hot metal in the HAZ during cooling. At high temperature, the metal has a low yield stress and can yield to accommodate the initial shrinkage. With the progress of cooling, the yield stress gradually increases, forcing the region to adjust the shrinkage effects elastically rather than by a plastic accommodation of the thermal contraction. The hot metal then shrinks against the constraint of the less-contracting cooler metal and thus tensile strains are generated at the hot zone. The thermal history is more complex for the generation of residual stresses in a multiple pass weld. The initial weld and the HAZ experience repeated annealing effects of short duration from each subsequent weld pass, which influences the final residual stress profile in the weldment.

From the measured points in the weld zone and in the HAZ at 10.5 mm from the weld centre-line in the small pipe and another set of measurements in the pipe performed earlier at 17.5 mm [12], two dimensional profiles of internal stress around the weld have been

developed. They are presented in figures 4.28 for the hoop direction and 4.29 for the axial direction.

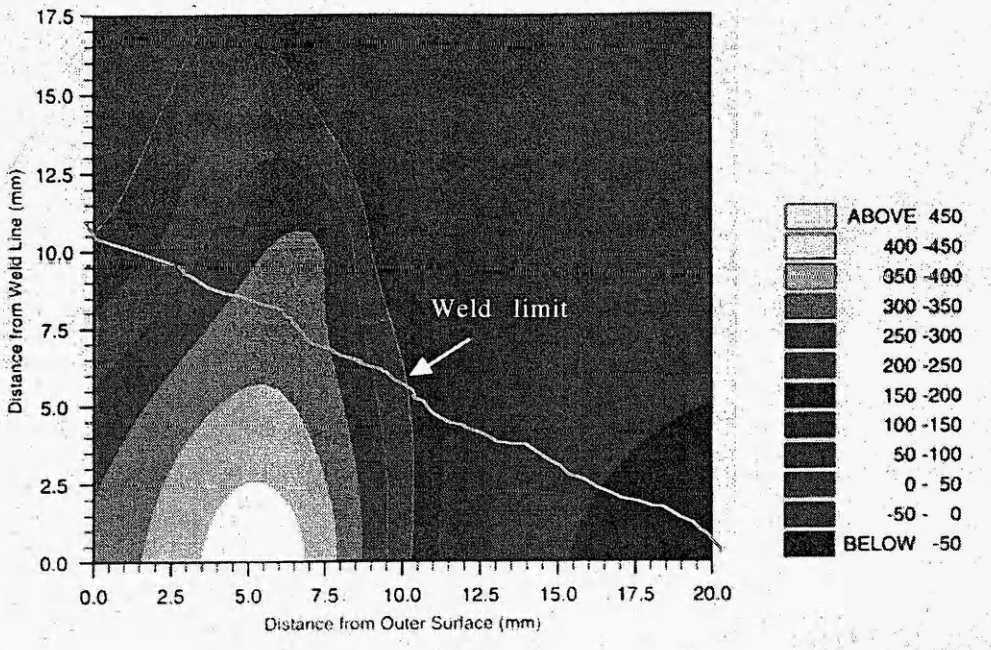

Figure 4.28: Two dimensional profile of the hoop stress around the original weld in the small pipe. It should be noted here that the x-axis represents the distance from the outer surface, and not from the inner surface as in the plots. The weld limit is an estimate.

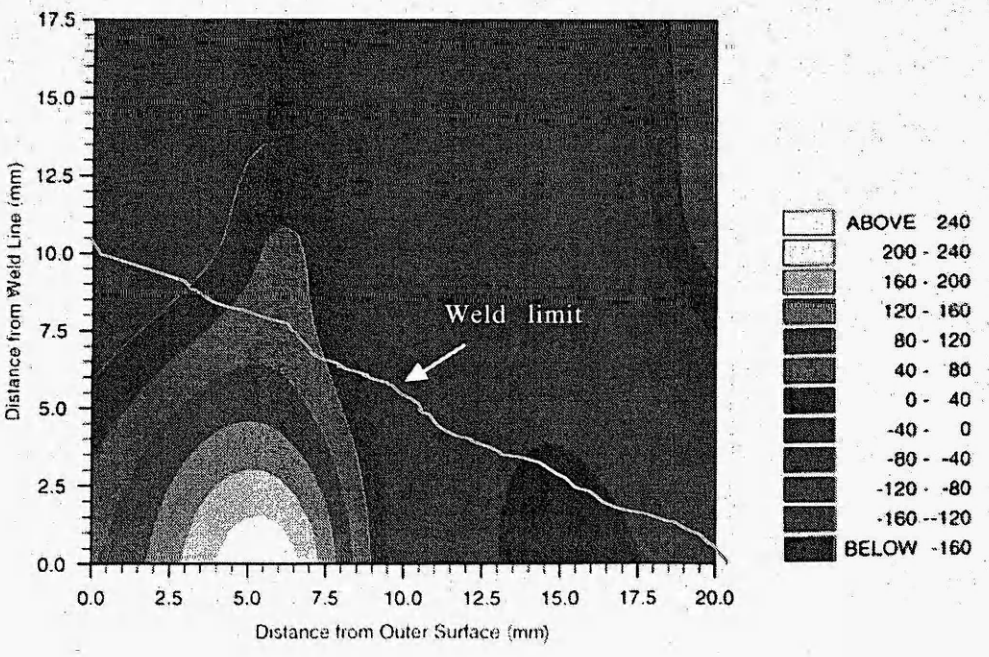

Figure 4.29: Two dimensional profile of the axial stress around the original weld in the small pipe. It should be noted here that the x-axis represents the distance from the outer surface, and not from the inner surface as in the plots. The weld limit is an estimate.

The hoop stress seems to be tensile everywhere in the region except around the root pass. The peak hoop stress can be noticed at 6 mm below the outer surface (or 14 mm from the inner surface) of the weld, *i.e.* just below the last weld cap pass, as expected in a multipass weld. Similar high stress positions beneath the final cap pass in multipass welds were either measured [16] or calculated [17] by others. Two points are to be noted here: firstly, the actual stress values in the weld zone should be less (by about 80 MPa as measured by Withers [11]) than the depicted values in the figures. This is due to the use of a single d_0 value measured at the far field parent metal. Secondly, the highly tensile region below the outer surface at ~10 mm away from the weld centre-line is more dangerous than the weld zone with peak stresses as far as reheat cracks are concerned; in austenitic steel pipes reheat cracks are frequently initiated beneath the last weld cap pass [18].

The annealing effects from the later weld passes on the weld metal and HAZ of the previous passes are manifested by the reduced stress in the rest of the region, as seen in figure 4.28. The initial root pass and its surrounding behave as a heat sink for the subsequent weld passes in a thick pipe and therefore a compressive residual stress is expected in this region.

In general, there is a strong interaction of cause and effect between the hoop and axial directions in a welded pipe. Shrinkage in the hoop direction of a circumferential weld causes axial bending stresses in the pipe. From the two dimensional stress profile as shown in figure 4.29, it is clear that the axial stress is tensile mainly around the last cap pass; otherwise it maintains a compressive profile. An overall compressive axial membrane stress in the HAZ and parent material is also visible which was probably caused by the global bending effect of the repair weld. The presence of tensile axial stresses close to the inner surface in the parent metal is not expected; but may be attributed to the repair weld effects or a slight underestimation of the d_0 value. Ideally, there should be a stress balance condition in the axial direction in a cylindrical pipe, *i.e.* the integral of the product of radial co-ordinate of the points and the stress along the axial direction through the whole thickness of the pipe should be zero, as expressed in equation 4.1. It should be noted that this stress balance condition was not valid for the small pipe because all measurements were performed after the introduction of the repair weld so that the specimen was no longer axi-symmetric. The

radial component of the residual stress was always found to maintain a low profile with values close to zero.

The measurements in the larger pipe produce similar results, particularly in the HAZ. The previous explanation of the generation of high tensile hoop stress beneath the final weld cap pass and the short annealing effects of multipass welds in reducing the initial tensile stresses towards the inner surface is also applicable for the large pipe. The wavy nature of the through-thickness stresses within the weld, measured at 7 mm away from the weld centre-line can be explained by a probable change in chemistry and/or microstructure in this region due to welding. The movement of a small amount of carbon or other elements from or into the stainless steel solution, which is highly plausible during the welding process, can result in a large variation in the lattice parameter. This was one of the reasons of the large scatter in d_0 values measured at different locations within the weld. Since the stress tensors of the original weld in this cylindrical pipe were not affected by any other effect like a repair weld, the axial stress balance condition was employed to obtain the average d_0 value, as described earlier.

The reliability of these measurements is further reinforced by the close agreement of the results in the small pipe with the values predicted by a finite element calculation, performed by British Energy.

4.6.2 Effects of Repair Weld on Residual Stress Field

The effects of a repair weld on the existing stress field in the small weld-pipe can be seen by studying the changes in measured through-wall HAZ stress values associated with the repair treatment as illustrated in figure 4.30.

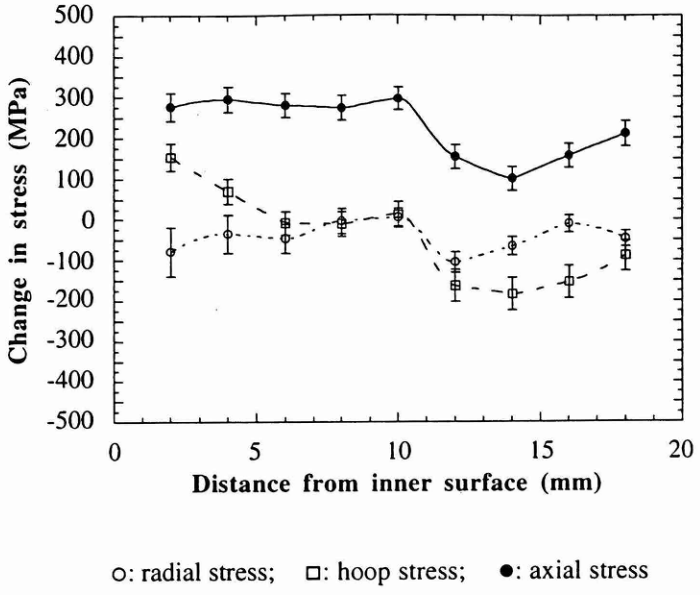

Figure 4.30: Change in residual stresses in the three principal directions caused by the repair treatment, measured in the HAZ at 10.5 mm away from the weld centre-line in the small pipe.

The repair treatment caused a significant increase in the axial stress in the HAZ, particularly over the inner half thickness (that is beyond the repair depth), where the increase was in the order of 300 MPa. Part of this increase can be attributed to global bending effects, as discussed earlier. The measured axial stresses in the repair HAZ displayed a membrane character of average tensile magnitude equal to 173 MPa, which is about 65% of the base metal 0.2% proof stress. Hoop stresses through the wall were generally reduced except near the inner surface. In effect, axial and hoop stresses became uniformly tensile throughout the thickness adjacent to the repair weld (see figure 4.13). No large change was observed in the radial direction due to the repair weld.

These features can be confirmed by comparing the measured near-surface profiles shown in figure 4.14. The axial stresses in the heat affected zone and the base metal are significantly increased by the repair treatment, and the tensile hoop stress decreases more rapidly moving away from the weld.

The measured residual stress field in the repair HAZ is also more tri-axial in nature than the remote girth weld location, with increases in hydrostatic stress in the order of 100 MPa over

the inner half thickness. The multi-axial nature of the measured repair weld stress field in the HAZ zone was used by British Energy [13] to estimate the expected reduction in creep ductility of the base material, using the function described by Bradford [1]. This analysis indicated that creep ductilities as low as 20% of the uniaxial properties may be induced by the multi-axial stress field in the HAZ about 2 mm below both the inner and outer surfaces. In the central region of the wall thickness the multi-axial creep ductility was predicted to be 50% or more of the uniaxial ductility. These findings imply that the test component repair weld would be significantly more susceptible to reheat cracking initiation than the original girth weld.

The neutron diffraction measurements have provided quantitative information about the effects of weld repairs on the three dimensional residual stress field in the test component girth weld, which is consistent with current understanding of repair welds.

4.7 SUMMARY

In this Chapter, the measurement and analysis of macrolevel stresses in stainless steel pipe weldments has been reported. The main objective was to study the effect of a part-thickness repair weld on the pre-existing residual stress field generated by the original weld. Neutron diffraction measurements have been performed through the pipe thickness in both the original and repair weld areas in a small diameter (170 mm) pipe and in the original weld area in a large diameter (432 mm) ex-service pipe from a nuclear power plant.

The results show the presence of a large tensile hoop stress in the outer half thickness in and around the weld with peak values just below the last weld cap pass. The peak values were found to be ~425 MPa in the weld fusion zone and ~300 MPa in the HAZ of the small pipe and ~300 MPa in both the weld region and HAZ in the large pipe. The axial stress distribution in the HAZ is nearly sinusoidal in the small pipe (compressive towards the inner surface and tensile towards the outer) and a parabola-type in the large pipe (tensile at the surfaces and compressive in the middle). The measured through-thickness stresses in the

small pipe show an impressive agreement with the finite element predictions performed in British Energy. A transverse scan at 5 mm away from the inner surface in the large pipe reveals that the tensile hoop stress gradually decreases with distance from the weld centre-line and attains a constant value, close to zero within the HAZ; but the compressive nature of the axial stress increases through the HAZ. The effect of a short part-thickness repair weld is manifested by a sharp rise (up to ~300 MPa) in the axial stress in the HAZ, particularly over the inner half thickness, *i.e.* beyond the repair depth; and a general reduction in the hoop stress through the thickness except near the inner surface. The radial stress has been found to be always low with values close to zero in both the original and repair weld areas. The presence of a highly tensile axial membrane stress (~175 MPa) in the repaired area relative to a compressive one (–55 MPa) in the original weld region implies that an overall bending in the pipe has been caused by the repairment.

4.8 REFERENCE

1. R. A. W. Bradford, *Finite Element Modelling of Reheat Cracking Initiation in Austenitic Weldments*, in Proc. International Conference on Assuring It's Safe, I Mech E, Edinburgh, UK, May 1998, pp. 287-295.

2. P. Dong, J. K. Hong, J. Zhang, P. Rogers, J. Bynum, and S. Shah, *Effects of Repair Weld Residual Stresses on Wide-Panel Specimens Loaded in Tension*, Trans. ASME- J. Press. Vessel Tech., 120, 1998, pp. 122-128.

3. J. Zhang, P. Dong, F. W. Brust, *A 3-D Composite Shell Element Model for Residual Stress Analysis of Multi-pass Welds*, in Trans. of the 14th International Conference on Structural Mechanics in Reactor Technology (SMiRT 14), Lyon, France, 1997, 1, pp. 335-344.

4. K. Masubuchi, *Analysis of Welded Structures*, Pergamon Press, 1980.

5. R. H. Leggatt, *Computer Modelling of Transverse Residual Stresses in Repair Welds*, Welding J., 70 (11), 1991, S299-S310.

6. Y. C. Kim, T. Yamakita, H. S. Bang and Y. Ueda, *Mechanical Charateristics of Repair Welds in a Thick Plate (Report II)*, Trans. JWRI, 17 (2), 1988, pp.137-145.

7. D. Q. Wang, Ph.D. Thesis, Dept. of Materials Engineering, The Open University, 1994.

8. D. Q. Wang and L. Edwards, *Precise Determination of Specimen Surface Position During Sub-Surface Strain Scanning by Neutron Diffraction*, in Proc. Fourth European Conference on Residual Stress (ECRS4), ed. S. Denis *et al.*, SFM, France, 1, 1996, pp. 135-144.

9. H. M. Rietveld, *A Profile Refinement Method for Nuclear and Magnetic Structures*, J. Appl. Cryst., 2, 1969, pp. 65-71.

10. M. R. Daymond, M. A. M. Bourke, R. B. Von Dreele, B. Clausen and T. Lorentzen, *Use of Rietveld Refinement for Elastic Macrostrain Determination and for Evaluation of Plastic Strain History from Diffraction Spectra*, J. Appl. Phys., 82 (4), 1997, pp. 1554-1562.

11. P. J. Withers, ISIS Experimental Report (RB No. 8230).

12. L. Edwards, D. Q. Wang, M. E. Fitzpatrick, ISIS Experimental Report (RB No. 8127).

13. Dr P. J. Bouchard, British Energy, Private Communications.

14. ABAQUS, Version 5.5, Hibbitt, Karlsson and Sorensen Inc.

15. A. Scaramangas and R. F. D. Porter Goff, *Residual Stresses in Cylinder Girth Butt Welds*, in Proc. 17th Annual Offshore Technology Conference, Houston, Texas, 1985, pp. 25-30.

16. R. A. Winholtz and A. D. Krawitz, *The Relaxation of Residual-Stresses with Postweld Heat-Treatment in a High Performance Weld Measured with Neutron Diffraction*, Metall. Mater. Trans.-A, 26.(5), 1995, pp. 1287-1295.

17. B. L. Josefson, *Stress Redistribution During Annealing of a Multipass Butt-Welded Pipe*, Trans. ASME- J. Pressure Vessel Tech., 105, 1983, pp. 165-170.

18. M. C. Coleman, D. A. Miller and R. A. Stevens, *Reheat Cracking and Strategies to Assure Integrity of Type 316 Welded Components*, in Proc. International Conference on Integrity of High-Temperature Welds, The Inst. of Mech. Engineers, 1998, pp.169-179.

CHAPTER 5: DETERMINATION OF RESIDUAL STRESSES AT THE MICROLEVEL

5.1 INTRODUCTION

For the study of microlevel residual stresses, a material is required where such stresses are present on a measurable scale. As mentioned earlier, and as will be discussed in detail in the next section, an MMC of aluminium alloy matrix reinforced with silicon carbide particulates was selected for this purpose. It has already been described in Chapter 2 (section 2.7.1), how various micro (and macro) stresses are generated in an MMC by simple quenching from a high temperature. This study on the microlevel residual stresses in MMCs can be divided in two parts:

- study with fatigue cracked specimens and
- study with heat treated specimens.

In the first set of experiments, two specimens were fatigue cracked by four point bending; one sample was plastically deformed by a uniaxial tensile load before fatiguing. Neutron strain measurement was carried out along the path of the fatigue crack. The samples were measured both unloaded and loaded elastically using a specially designed four point bending rig, to the same value of K_{max} that was experienced in the specimens during crack growth. Strain gauges were mounted on the specimens to allow monitoring of the applied load. Strain was measured along the three principal axes as inferred from the symmetry of the specimens; this allowed calculation of the total stress. Various stress components were then separated out as described in the second Chapter, and the effect of plasticity on the stresses, misfit stresses in particular, near the crack tip was studied under the conditions of plastic stretching and elastic loading.

In the second set of experiments, a series of MMC specimens were heat treated, both at sub-zero and high temperatures following plastic deformation in bending. The aim of these experiments was to investigate the change in both macrostress and misfit stress occurring during the heat treatment process, particularly in the areas where the misfit stress had been altered by the plastic deformation.

Pulsed neutron strain scanning was used to measure the strain variations for both sets of experiments at the ENGIN spectrometer at ISIS, the Rutherford Appleton Laboratory, UK during different periods of time: the first set with fatigue cracks in March, 1997 and the second set with heat treatments in June, 1998. Two specimens of the second set of experiments were also measured at a reactor neutron source, D1A of ILL, France in April, 1999. Details of these experiments, experimental results, determination of microlevel stresses and their interpretations will be presented in this Chapter.

5.2 EXPERIMENTAL DETAILS

5.2.1 The Material

The material studied was an MMC of 2124 Al alloy matrix reinforced with SiC particles. MMCs are potential materials for applications in the aerospace and automobile industries where stiffness critical components can be manufactured by composites with a great saving of weight, and so an increase in fuel economy. For an MMC of the type studied here, the reinforcement (SiC) has a much higher stiffness (E) of 450 GPa than the 2124 Al alloy matrix (E=72 GPa) with a similar density (ρ) (3.2 g/cm^3 and 2.77 g/cm^3 respectively) [1]: this gives a higher specific stiffness (E/ρ) to the composite. A description of a wide range of applications of MMCs with their improved stiffness, strength, resistance to wear and creep can be found in [2]. But the potential of MMCs was not the only reason for selecting this material in this study. It was also the presence of micro-level misfit stresses in the material as described earlier. The materials used here were produced by Aerospace Metal Composites, Farnborough by a powder metallurgy technique, consisting of blending and

compaction. In this process, fine powders of the matrix and reinforcement are thoroughly blended and cold-compacted before the hot isostatic pressing (HIPing). The SiC content was ~17% by volume (20% by weight) in the material used for the first set of experiments; and ~22% by volume (25% by weight) in the material for the second set of experiments. The matrix of the material in both sets of experiments was based on 2124 aluminium, which nominally contains 4.2% Cu, 1.5% Mg and 0.6% Mn (all in weight percent). This is a precipitation hardening alloy with $CuAl_2$ or θ-phase as the main precipitate along with the presence of S´-phase (Al_2CuMg).

The density of the composite (17 vol% of SiC) is 2.85 g/cm^3 and the modulus of elasticity is 100 GPa. After a heat treatment under a T4 condition (solution treatment, quenching and natural ageing at room temperature), the extruded MMC has a yield strength of 410 MPa, an ultimate tensile strength (UTS) of 620 MPa with a ductility of 7% (data taken from the technical data sheet of Aerospace Metal Composites Ltd., Farnborough).

5.2.2 Preparation of Test Specimens

Fatigue Cracked Specimens

The MMC plate used for the first set of experiments was first solution heat treated comprising a two hour soak at 505°C followed by a cold water quench to generate various macro and micro stresses in it, as described in section 1.3. In order to relieve partially any long range stress variation present in the quenched plate, it was then given an overageing treatment at 180°C for 48 hours [3]. The combination of the time and temperature for this overageing treatment was selected from previous reported results of ageing treatments in similar Al/SiC_p MMCs [4-6]. Two samples were prepared as standard edge notched bend (SENB) specimens as shown in figure 5.1. A plastic deformation of 1% was introduced in one of the samples before its final machining by applying a tensile load along the

longitudinal axis (y-direction) of the specimen. Both were fatigue cracked using four point bending. Details of the specimens are given in Table 5.1.

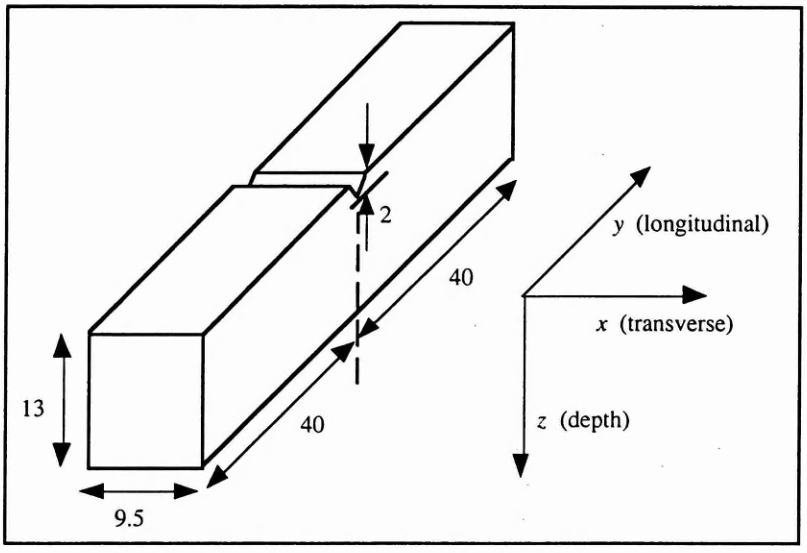

Figure 5.1: Diagram of the specimen and axis definition for the first set of experiments. All dimensions are in millimetres.

	K_{max} during final crack growth (MPa$\sqrt{m}$)	R (K_{min}/K_{max})	Final crack length (mm)
Unstretched sample	14.3	0.1	6.0
Stretched sample	15.8	0.1	5.8

Table 5.1: Details of the two fatigued specimens that were examined.

Heat Treated Specimens

For the second set of experiments, a block of the composite material (with 22 vol% of SiC) of dimension 135 x 77 x 29 mm^3 was first solution treated at 505°C for 2 hours followed by a water quench and prolonged natural ageing at room temperature. A number of specimens were cut from this MMC block as shown in figure 5.2. A diagram of an individual specimen along with the axis definition is also given below the composite block in the same figure.

A higher amount of reinforcement leads to a reduced strain-to-failure. These specimens were therefore given a total deformation in bending of 1%, giving a plastic deformation of ~0.3%. The width of the specimens was reduced by about 11 mm from the original one, as shown in the figure. One sample was kept as-deformed and four of them were then heat treated. The details of the dimensions, amount of deformation introduced and heat treatment for all specimens that were examined, is given in Table 5.2. All heat treated specimens were cooled in air after the heat treatment. The end specimen (No. 11) which was neither deformed nor heat treated, was measured to obtain the initial quench thermal stress in the composite. The as-deformed specimen (No. 2) was finally kept in liquid nitrogen for 30 minutes and then left in air to bring it back to room temperature and examined again to see if there was any modification in the residual stress states by the liquid nitrogen treatment.

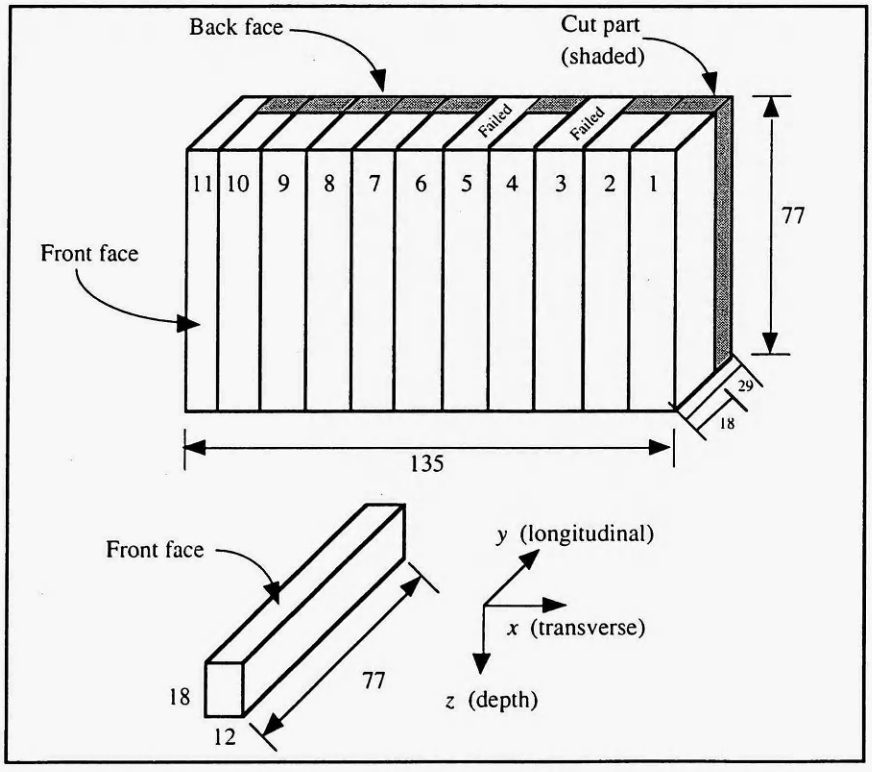

Figure 5.2: The composite block from which the specimens were machined. The width of the specimens was reduced (shaded part) individually. Below the composite block is the diagram of an individual specimen along with the axis definition. All dimensions are in millimetres.

Specimen No.	Dimension			Deformation		Heat treatment	
	Length (y) (mm)	Depth (z) (mm)	Thickness (x) (mm)	Total (%)	Plastic (%)	Temperature (°C)	Time (h)
2	77.0	18.2	12.5	1.0	0.32	-	-
6	77.0	18.0	12.2	1.0	0.33	180	48
7	77.0	17.7	12.0	1.0	0.34	240	0.5
8	77.0	17.9	12.3	1.0	0.35	300	0.5
10	77.0	18.3	12.1	1.0	0.33	240	2
11	77.0	29.0	8.0	-	-	-	-
2	77.0	18.2	12.5	1.0	0.32	–196	15

Table 5.2: Details of the dimension, deformation by four point bending and heat treatments for the specimens of the second set of experiments.

Different heat treatment temperatures and times were selected to study their effects on the residual stresses. Two specimens were treated for different times at the same temperature; and two specimens were treated for the same time at two different temperatures, as shown in table 5.2.

5.2.3 Experimental Set-up and Procedure

Fatigue Cracked Specimens

The strain variation was measured in the three principal directions of the samples as a function of position along the z direction, as defined in figure 5.1. The principal strain directions were inferred from the symmetry of the specimens to lie along the axes, also shown in the same figure. The general set-up of the ENGIN spectrometer has already been shown in Chapter 2 (figure 2.2). Neutron strain measurement was carried out in two stages; firstly with no applied load and then loaded *in situ* on the diffractometer with the help

of a specially designed loading rig, as shown schematically in figure 5.3. The loading rig allowed the specimens to be loaded by four point bending to the same K_{max} value that was applied to them during the final stage of crack extension. This was achieved by strain gauge measurement on the back-face of the specimens during loading, and reproduction of the back-face strain when they were loaded from zero to the maximum load on the testing machine. There was enough space for the neutron beam to traverse without going through any part of the steel loading frame. A photograph of the specimen within the loading rig, placed on the ENGIN diffractometer is shown in figure 5.4.

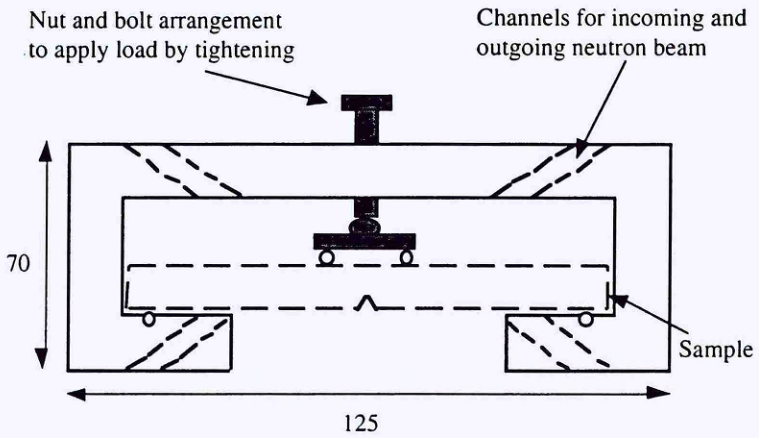

Figure 5.3: Schematic of the stress rig that was used to reproduce the crack propagation load in the specimens *in situ* on the ENGIN diffractometer; dimensions in millimetres.

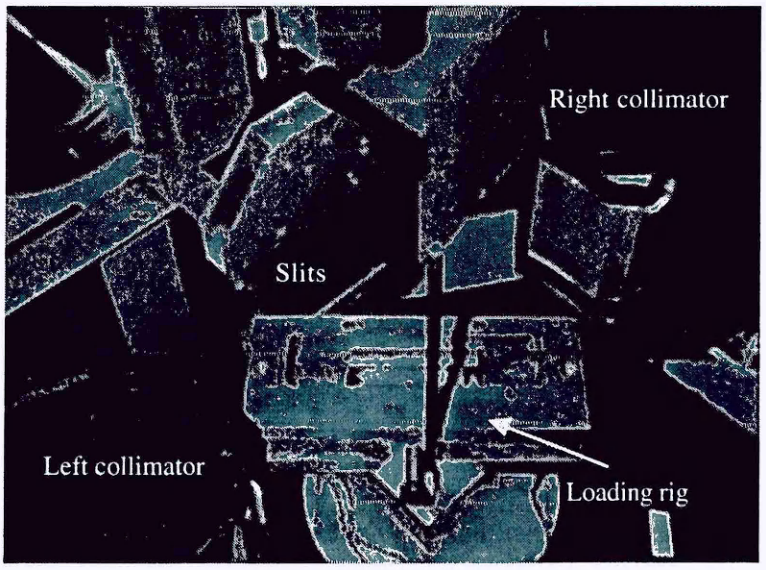

Figure 5.4: Photograph of the loading rig with a specimen on the ENGIN diffractometer. The specimen is set for strain measurement along the *y* and *z* directions of the specimen.

The sampling or 'gauge' volume used was $2 \times 5 \times 1.6\,mm^3$, with the long axis of the gauge volume aligned along the *x*-direction for measurement of the ε_y and ε_z strains, and along the *y*-direction for measurement of the ε_x strains. Simultaneous measurement of two perpendicular strain directions was possible as the ENGIN spectrometer has two separate radial collimators with detector banks, situated on opposite sides of the sample position, as mentioned earlier. Hence, the ε_y and ε_x strains were measured with the sample in one orientation, and ε_z and ε_y in another. The ε_y strain variation was therefore measured twice, and the results from these duplicate measurements showed that the averaging of the ε_x strain along the *y*-direction did not cause large errors in the results. The measurement positions were determined by first aligning the specimens with the help of two telescopes and then confirming the precise location using the intensity of the diffracted beam as the gauge volume enters the specimen [7, 8].

A modified Pawley fit was applied to the time-of-flight diffraction patterns to determine the lattice parameters. Typical spectra for the composites are shown in figures 5.5 and 5.6, with the fitted spectra for the aluminium shown in figure 5.5, and that for the silicon carbide shown in figure 5.6. These plots show how the fitting routine selects only the peaks which are obtained from the phase of interest, by virtue of a knowledge of its approximate lattice parameter and crystal structure. The SiC phase in this composite was mainly cubic; however, a non-cubic polytype peak was captured during the measurements, as shown in figure 5.6.

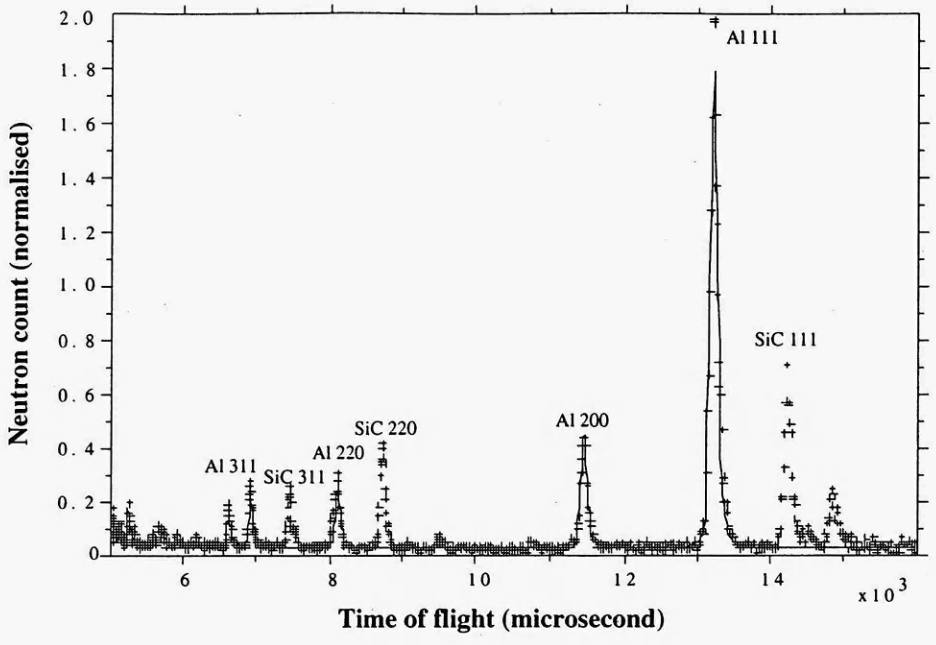

Figure 5.5: Time of flight neutron diffraction spectrum obtained from Al/SiC composite material, showing modified Pawley fit to aluminium peaks.

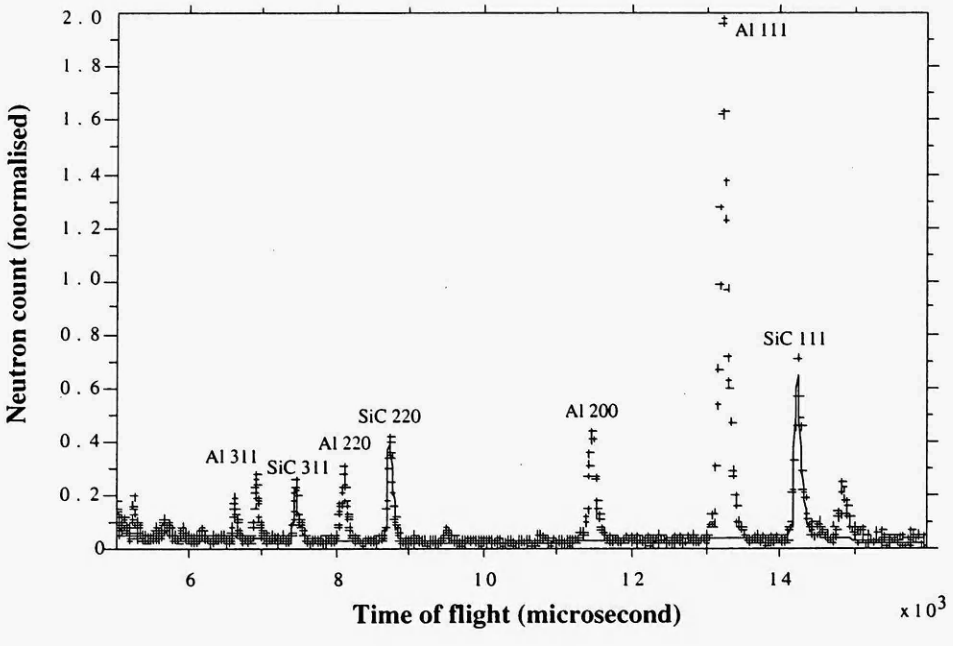

Figure 5.6: Time of flight neutron diffraction spectrum obtained from Al/SiC composite material, showing modified Pawley fit to silicon carbide peaks. The unfitted peak to right of SiC (111) reflection arises from a non-cubic SiC polytype present in the composite.

Heat Treated Specimens

In the second set of experiments, the heat treated samples and as-deformed specimen were measured at the ENGIN spectrometer of ISIS. Two specimens, the quenched and naturally aged (Q+NA) and the as-deformed specimen (specimen nos. 11 and 2 respectively) were examined at ILL, France to see the change made by the bending load and liquid nitrogen treatment on the thermal residual stresses, since the as-deformed sample was measured both before and after a treatment with liquid nitrogen.

For the heat treated specimens at ISIS, a gauge volume of $2 \times 10 \times 1.6\,mm^3$ was used, with the long axis of the gauge volume again aligned along the *x*-direction for measurement of the ε_y and ε_z strains, and along the *y*-direction for measurement of the ε_x strains. A photograph of the experimental set-up is shown in figure 5.7. In this particular set-up, three specimens were fixed on a support block for consecutive measurements of ε_x and ε_z strains. Specimens were placed wide apart to avoid any interference of the neutron beam between samples.

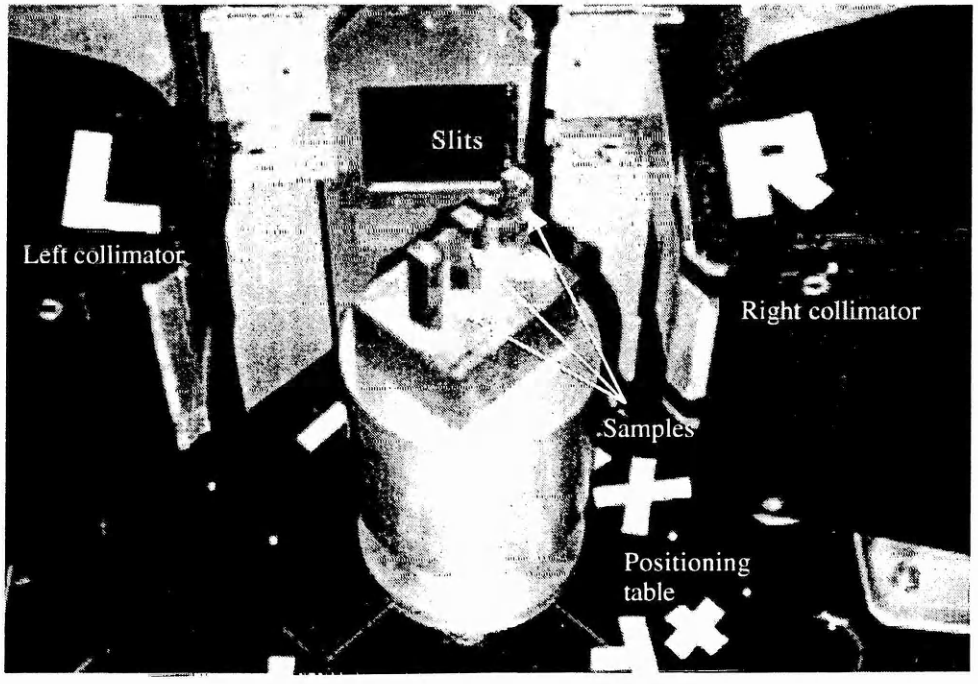

Figure 5.7: Photograph of the experimental set-up for the heat treated specimens on the ENGIN spectrometer. The specimens are set for strain measurement along their *x* and *z* directions.

The time-of-flight diffraction data obtained at ISIS, were fitted using the modified Pawley fit program to determine the lattice parameters for the aluminium phase. The silicon carbide phase was found to be a polytype in this MMC. The same fitting program could not be used to fit the SiC peaks for many of the experimental data because of the multi-polytype nature of the phase. A single peak fitting program 'RESFIT' was therefore used to fit the hexagonal SiC (110) peak for all specimens as well as the SiC powder. The strain values in the three principal directions were then obtained by comparing the measured lattice parameters of Al and SiC phases of the composite with those of the corresponding powder specimens.

During the measurement of the Q+NA specimen and the deformed specimen before and after the treatment with liquid nitrogen at the reactor source of ILL, France, a wavelength of 1.9114 Å was used to detect Al (311) peaks and 2.993 Å for SiC (110) peaks. Apertures of $1 \times 10\ mm^2$ or $2 \times 4\ mm^2$, depending on the specimen orientation, were used in the incoming beam. No slit mask was used in front of the detector to get the detector focal width of 1.1 mm. A single peak fitting program was used to fit the (311) peak for aluminium and (110) peak for SiC_{6H} in both composite bars and the powder specimens. The strain was determined in three principal directions from the shift in scattering angle, using equation 2.6.

Calculation of the total stresses and separation of macro and micro stresses were performed as in the first set of experiments. The values of the elastic constant and Poisson ratio for SiC_{6H} (110), which were used in stress calculations, were obtained using the Kröner model. They were found to be 469 GPa and 0.14 respectively. For aluminium, the same values as used in previous calculations, *i.e.* 72 GPa and 0.33 were considered. The gauge volume was always kept totally immersed in the specimens. In both sets of experiments, powder samples of matrix and reinforcement materials were measured separately to obtain the reference strain-free lattice parameters (a_0).

5.3 RESULTS: FATIGUED SPECIMENS

5.3.1 Measured Strains

Strain values were calculated from a comparison of the measured lattice parameters in the composite with those obtained from the powder samples. The matrix and reinforcement strains in the three principal directions for both unstretched and stretched bars, in the unloaded state, are shown in figures 5.8 and 5.9 respectively. Error values arising from the uncertainties in measured peak position are shown as line bars along with the corresponding points. In the unstretched specimen, general tension in the matrix and compression in the reinforcement can be observed. Although the measurement was performed along the crack path, the gauge volume was too large relative to the plastic zone around the crack to reveal the effects of fatigue crack plasticity on the thermal residual stresses and thus the expected natures of a tensile matrix and a compressive reinforcement in an MMC are obtained. From the standard relation for the plastic zone ahead of a crack tip (r_c) under a cyclic load [9], *i.e.*

$$r_c \approx \frac{1}{\pi}\left(\frac{\Delta K_I}{2\sigma_{YS}}\right)^2 \qquad \text{(Equation 5.1)}$$

and for the composite material that was examined, which has a yield strength (σ_{YS}) of ~410 MPa as mentioned earlier, it can be calculated that a relatively high range of applied stress intensity factor (ΔK_I) of 15 MPa$\sqrt{m}$ will produce a maximum plastic zone size of ~100 μm. The gauge volume was much larger than this, extending up to 2 mm away from the fatigue crack path.

It is evident from the plots that there are clear differences between the absolute strains that are measured in the stretched and unstretched samples. In general, the measured strains become less tensile in the matrix and less compressive in the reinforcement due to pre-straining of the specimen.

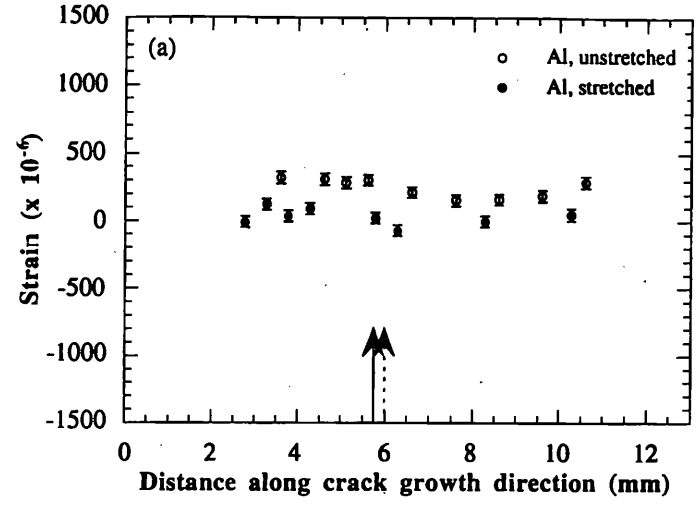

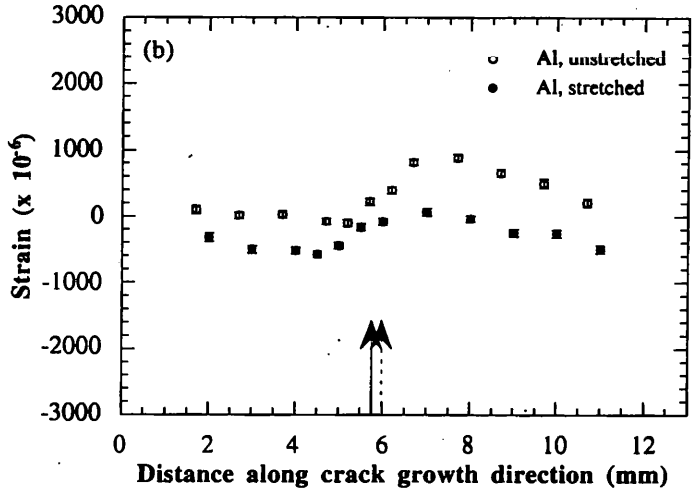

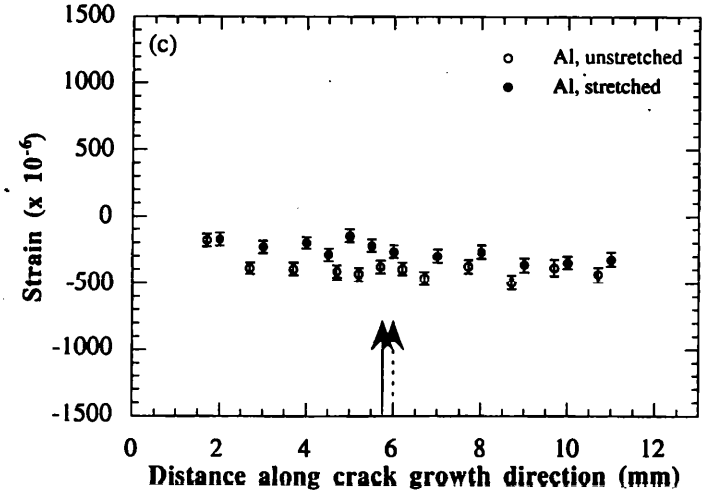

Figure 5.8: Matrix strains in unstretched and stretched specimens with no applied load: (a) ε_x strain, (b) ε_y strain and (c) ε_z strain. The arrows indicate the position of the crack tip: the broken line for the unstretched specimen and the solid line for the stretched one.

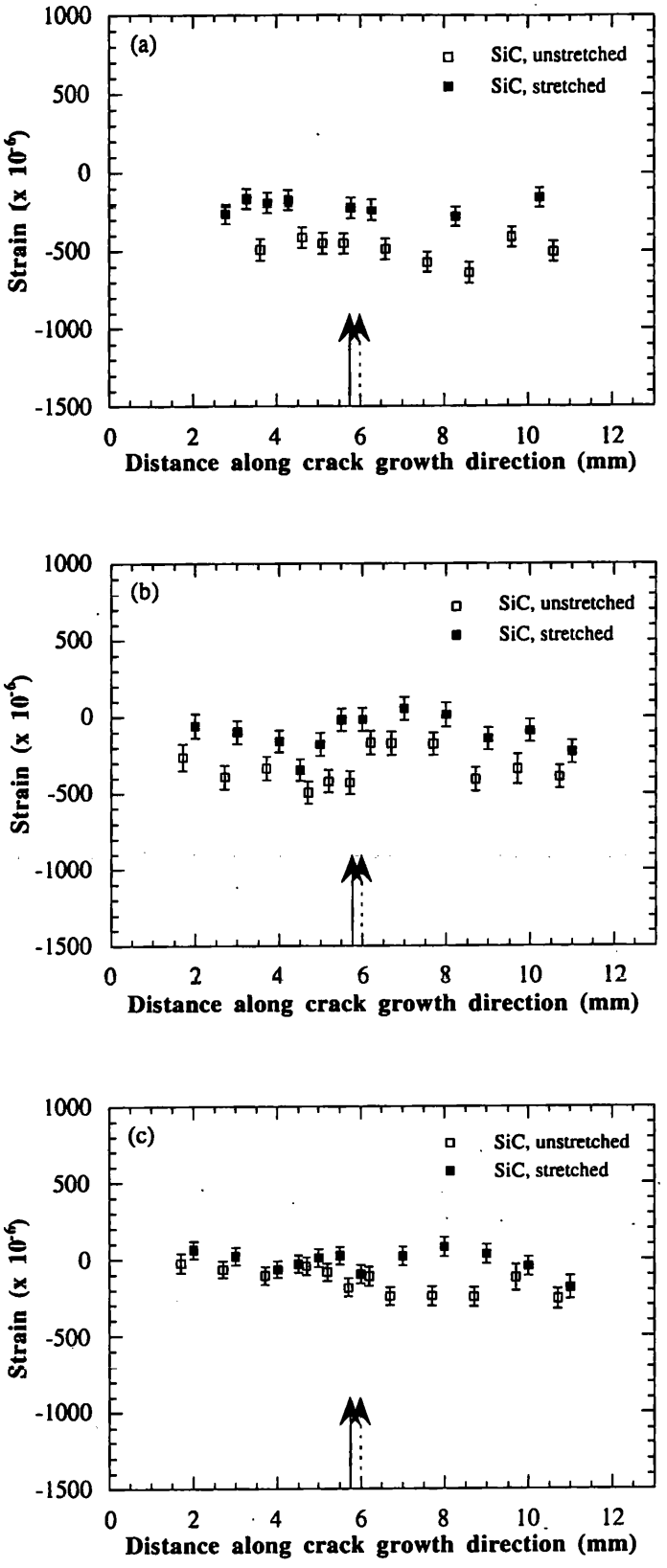

Figure 5.9: Reinforcement strains in unstretched and stretched specimens with no applied load: (a) ε_x strain, (b) ε_y strain and (c) ε_z strain. The arrows indicate the position of the crack tip: the broken line for the unstretched specimen and the solid line for the stretched one.

Similarly, the absolute strain values were obtained in the three principal directions for both phases of the specimens, when loaded to K_{max}. They are shown in figures 5.10 and 5.11 for the matrix and reinforcement respectively. Application of a bending load gives the expected effect, particularly in the crack opening direction (longitudinal or y-direction): for both phases, the crack tip region becomes increasingly tensile and the area far ahead of the crack tip becomes increasingly compressive; while almost a flat level of strain can be observed at the crack wake. The opposite effect in the x-direction is probably due to the Poisson strains. There is not much difference in strain through the depth for either phase in the z-direction, as also observed in the unloaded specimens; but a definite increase in strains due to loading can be noticed, if compared with the unloaded data. A similar effect of stretching as observed in the unloaded specimens, is also apparent here, *i.e.* the matrix becomes less tensile and the reinforcement becomes less compressive.

It has been mentioned earlier that the measurement in the y-direction was repeated as an additional set of data counted by the left detector, while measuring for the x-direction on the right detector. This gives an opportunity to examine the reproducibility of neutron measurement results by comparing the data of repeat measurements by the same detector. The measured strains in the matrix of the unstretched specimen are shown in figure 5.12 for both loaded and unloaded conditions. An excellent match between these two sets of data proves the high degree of reproducibility. Similar matching values were also obtained for the reinforcement phase and for both phases in the stretched specimen. The long axis (5 mm) of the gauge volume was along the x-direction of the specimen in the first set of measurements and along the y-direction during the repeat measurements. Identical results from these two sets of measurements also show that averaging of the ε_x strains along the y-direction did not make large errors in this case.

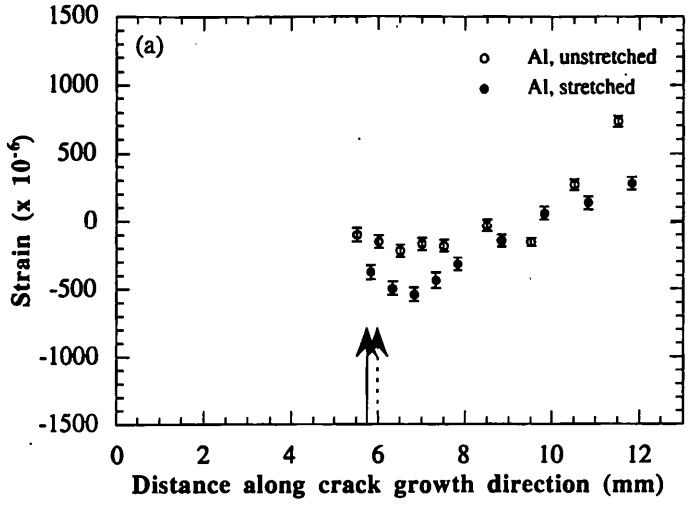

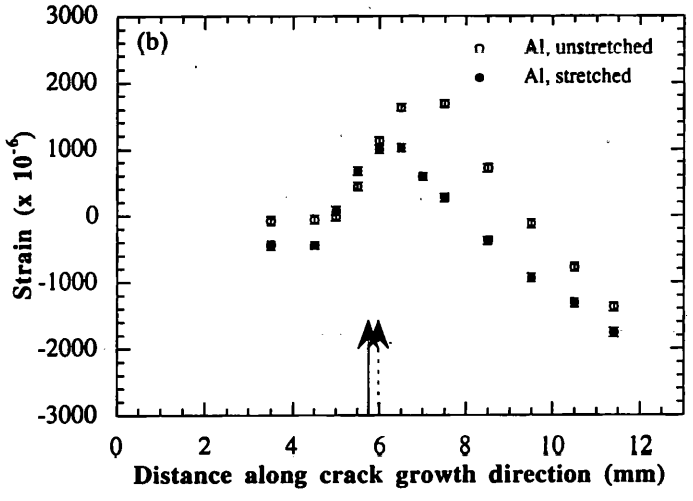

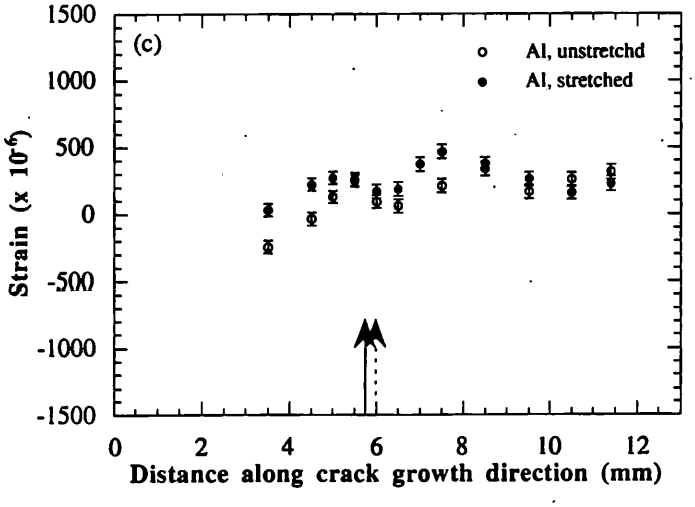

Figure 5.10: Matrix strains in unstretched and stretched specimens, loaded to K_{max}: (a) ε_x strain, (b) ε_y strain and (c) ε_z strain. The arrows indicate the position of the crack tip: the broken line for the unstretched specimen and the solid line for the stretched one.

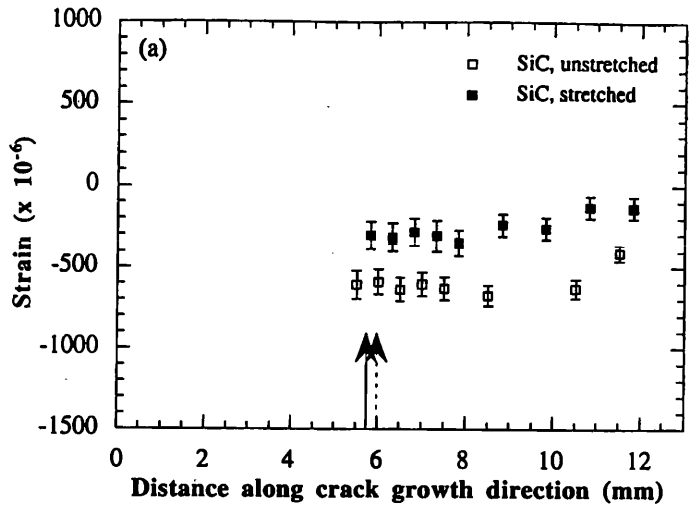

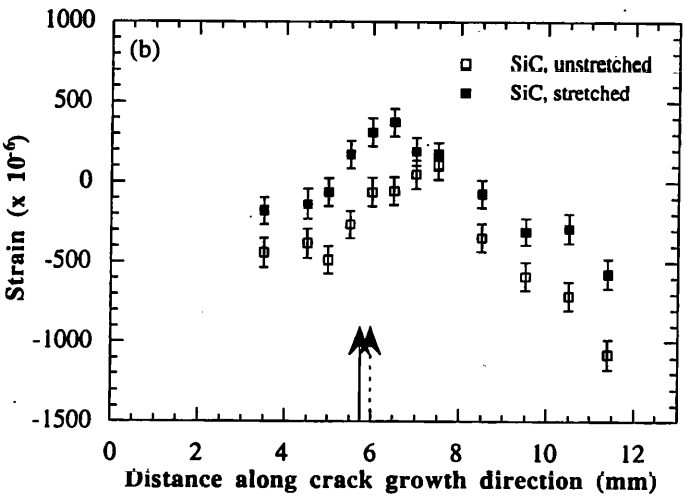

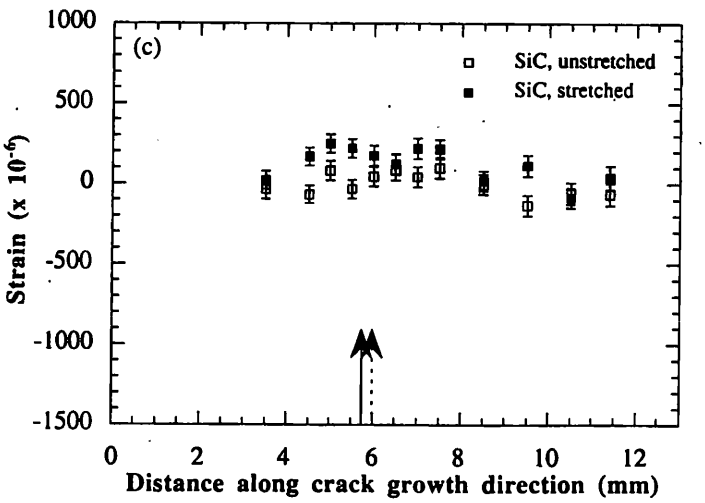

Figure 5.11: Reinforcement strains in unstretched and stretched specimens, loaded to K_{max}: (a) ε_x strain, (b) ε_y strain and (c) ε_z strain. The arrows indicate the position of the crack tip: the broken line for the unstretched specimen and the solid line for the stretched one.

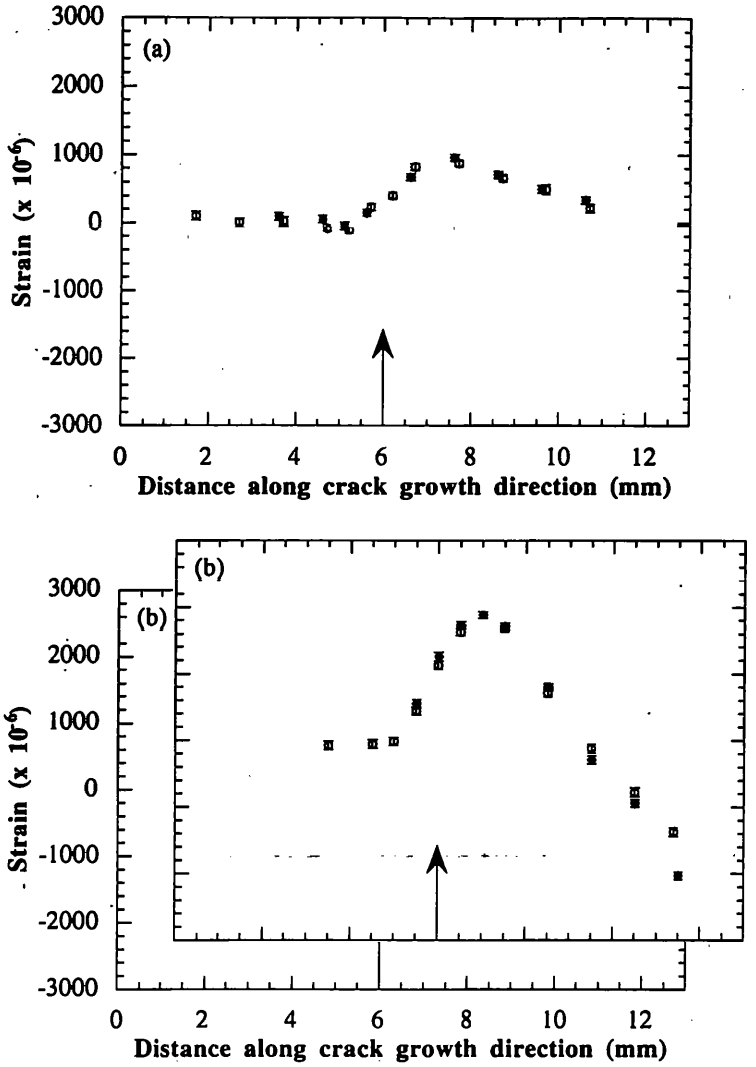

Figure 5.12: Comparison of the matrix strains in the unstretched specimen, measured twice in the *y*-direction; (a) unloaded, (b) loaded to K_{max}. The arrow indicates the position of the crack tip.

5.3.2 Calculated Total Stresses

The strain measurements were made along three strain directions parallel to the specimen axes. As the sample geometry is simple, it can be inferred that these are also the principal stress directions. It is therefore possible to use the three measured strain variations to calculate the principal stress variations. This is achieved by simple elasticity theory as described in Chapter 2. As the fitting routine gives an average lattice parameter over all the

crystal reflections, the bulk Young's modulus was used in the conversion from strain to stress. The values of Young's modulus (E) and the Poisson ratio (ν) used in these calculations are 72 GPa and 0.33 respectively for Al, and 450 GPa and 0.14 respectively for SiC. Some interpolation of strain data between measured positions was required to generate values of ε_x, ε_y, and ε_z in equivalent positions within the sample. The error values at the nearest measured points were considered for such interpolated strains. The total stresses so calculated in the three principal directions are shown in figures 5.13 to 5.16 for each phase in unloaded and loaded conditions. Since the error values do not vary much, the average error is given for each plot for clarity, instead of putting individual error bars on each point.

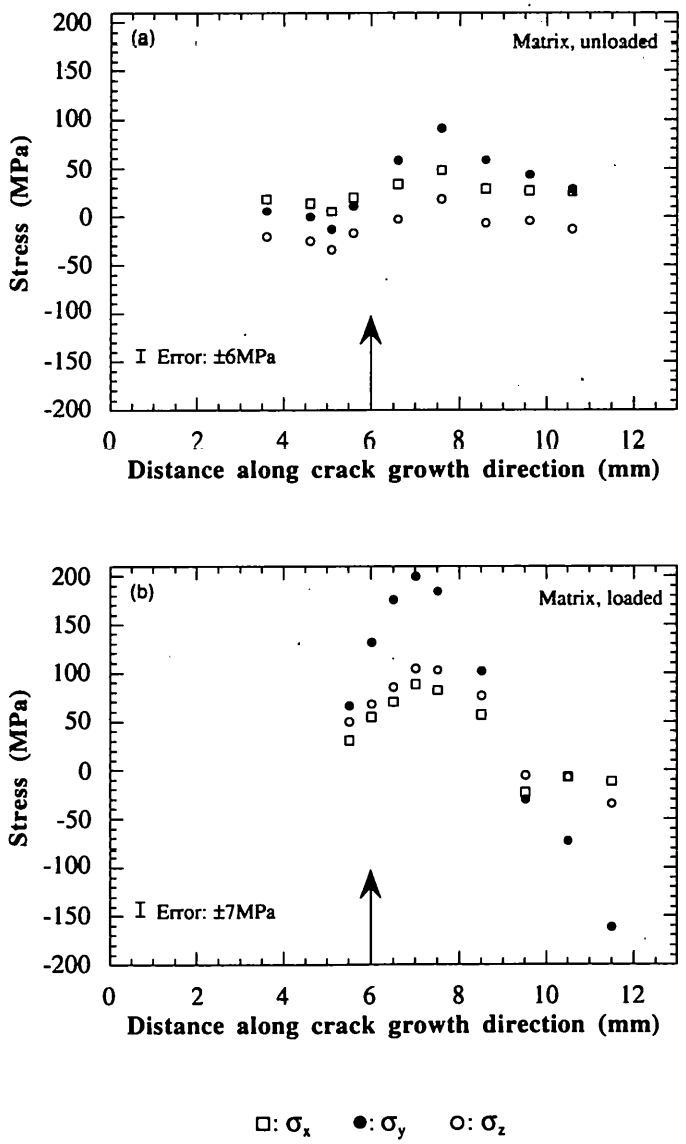

Figure 5.13: Variation of total stresses in the three principal directions for the matrix of the unstretched specimen: (a) unloaded and (b) loaded to K_{max}. The arrow indicates the position of the crack tip.

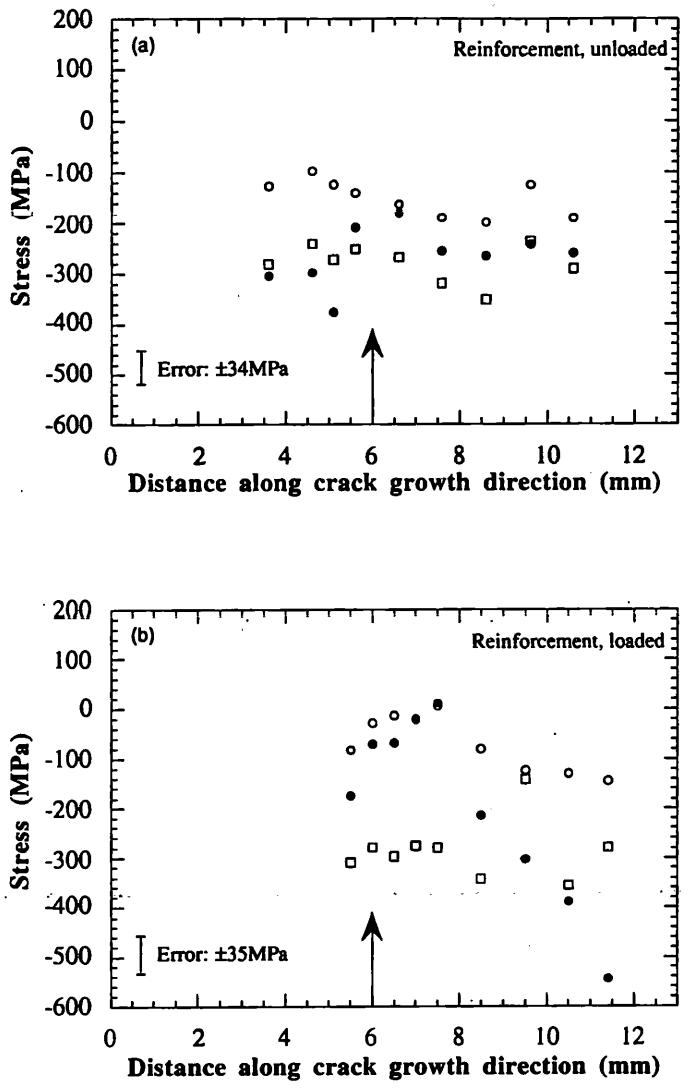

Figure 5.14: Variation of total stresses in the three principal directions for the reinforcement of the unstretched specimen: (a) unloaded and (b) loaded to K_{max}. The arrow indicates the position of the crack tip.

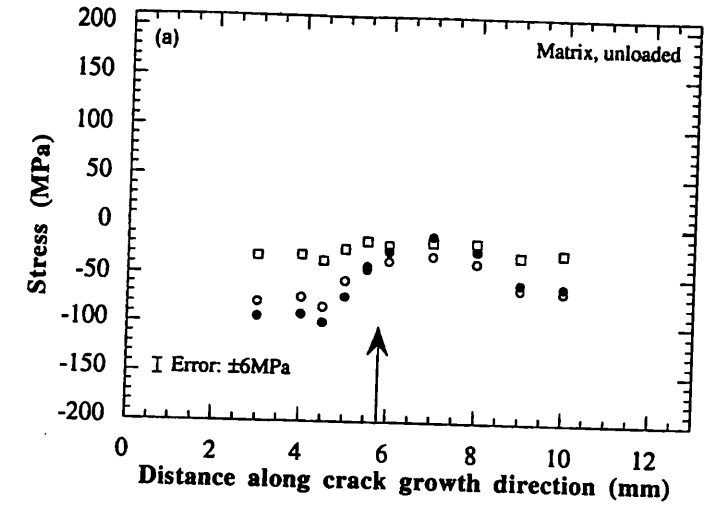

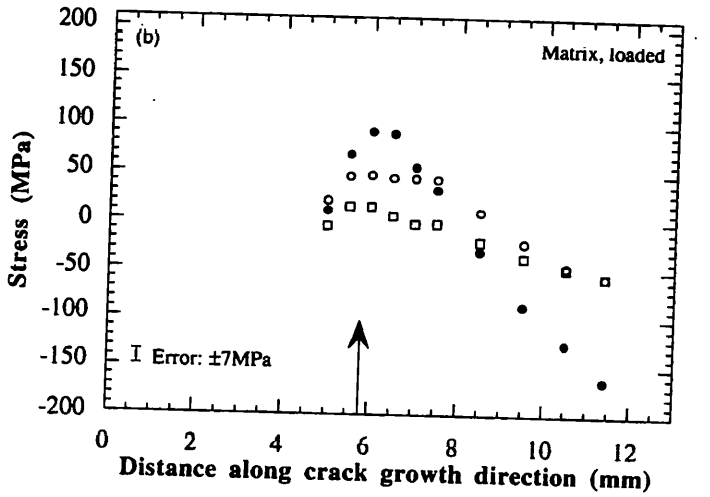

□: σ_x ●: σ_y ○: σ_z

Figure 5.15: Variation of total stresses in the three principal directions for the matrix of the stretched specimen: (a) unloaded and (b) loaded to K_{max}. The arrow indicates the position of the crack tip.

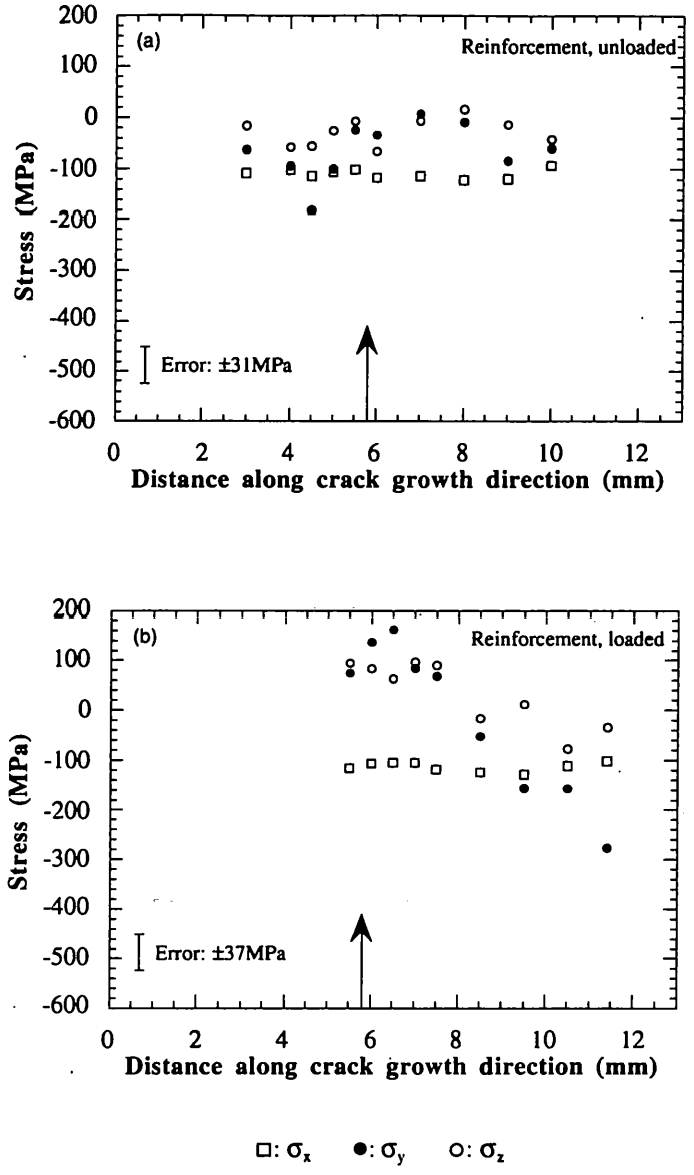

Figure 5.16: Variation of total stresses in the three principal directions for the reinforcement of the stretched specimen: (a) unloaded and (b) loaded to K_{max}. The arrow indicates the position of the crack tip.

The effects of stretching and loading the composite become more clear from these figures. The observations made from the plots of measured strains can now be explained in terms of total stresses. For the unstretched sample, in both the loaded and unloaded conditions (figures 5.13 and 5.14), the matrix can be seen to be shifted in a tensile sense relative to the stress in the reinforcement. The effect of the applied four point bending load is precisely as expected: the stress in the region of the crack tip becomes increasingly tensile, while the back face of the sample is compressed. The effect of the stretch is manifested by a change in the near-crack tip stress: a comparison of the near-crack tip stress between the stretched

and the unstretched samples (figures 5.13 and 5.14 vs. figures 5.15 and 5.16) shows that the matrix stresses are less tensile after the stretch, while the reinforcement stresses become more tensile. This is not an effect of different loading conditions for the two samples: figure 5.17 shows that the differences in total stresses in the crack opening direction between the loaded and unloaded conditions for the two samples are approximately equal. This also shows the intensification of the crack tip stress arising from external loading during the fatigue of a component.

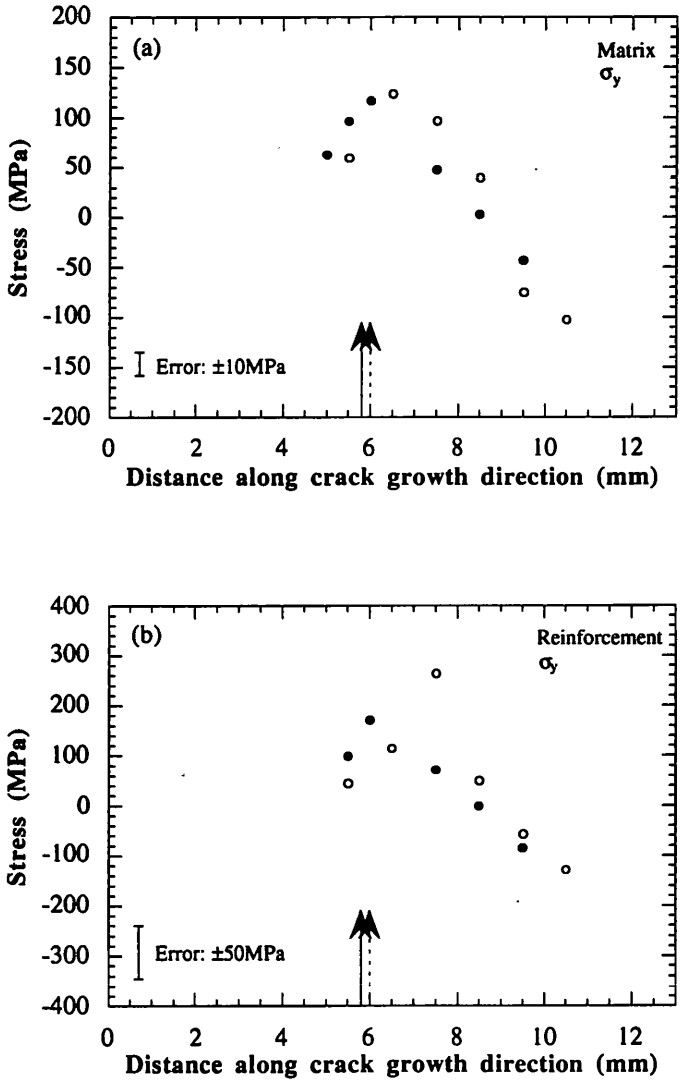

Figure 5.17: Change in total stress between the loaded and unloaded conditions for the two samples in (a) the matrix and (b) the reinforcement. Fewer points are shown than in the previous figures, as only positions where strains were recorded in both loaded and unloaded states could be used for the subtraction. The arrows are as described in figure 5.11.

5.3.3 *Macro and Micro Stress Components*

It is now possible to separate the macro and micro stress components that exist in the material by combining these phase stresses. Full description of this stress separation method was given in Chapter 2. The first stage in the process is to calculate the overall macrostress in the material, which is essentially that stress which would exist if the material were homogeneous. So the macrostress in any particular direction is the same for both the matrix and reinforcement. The calculated macrostresses in the three principal directions are shown in figure 5.18 for the unstretched specimen and in figure 5.19 for the stretched one. The average error values arising from errors of the total stresses are also given in the figures. From the simple geometry of the specimens, it is expected that these macrostress components in each direction would sum to zero. However, a small bias towards net compression is apparent from the figures, particularly in figure 5.19(a). This may be attributed to any small difference of the elastic load transfer coefficients, or the volume fraction of reinforcement that was used in calculations, from the exact ones; the effect of the small plastic zone around the crack; or more probably, a small error in the determination of the stress free lattice parameter. All points may be pushed towards compression by a slight over estimation of the stress free lattice parameter of the matrix. It is well established that the lattice parameter of aluminium is very sensitive to the presence of solute atoms [10]. Different ageing characteristics of the reinforced and parent alloys may be another reason for an incorrect stress free lattice parameter [3]. An identical observation of compressive macrostresses in a similar Al-SiC system was reported by Fitzpatrick *et al.* [3].

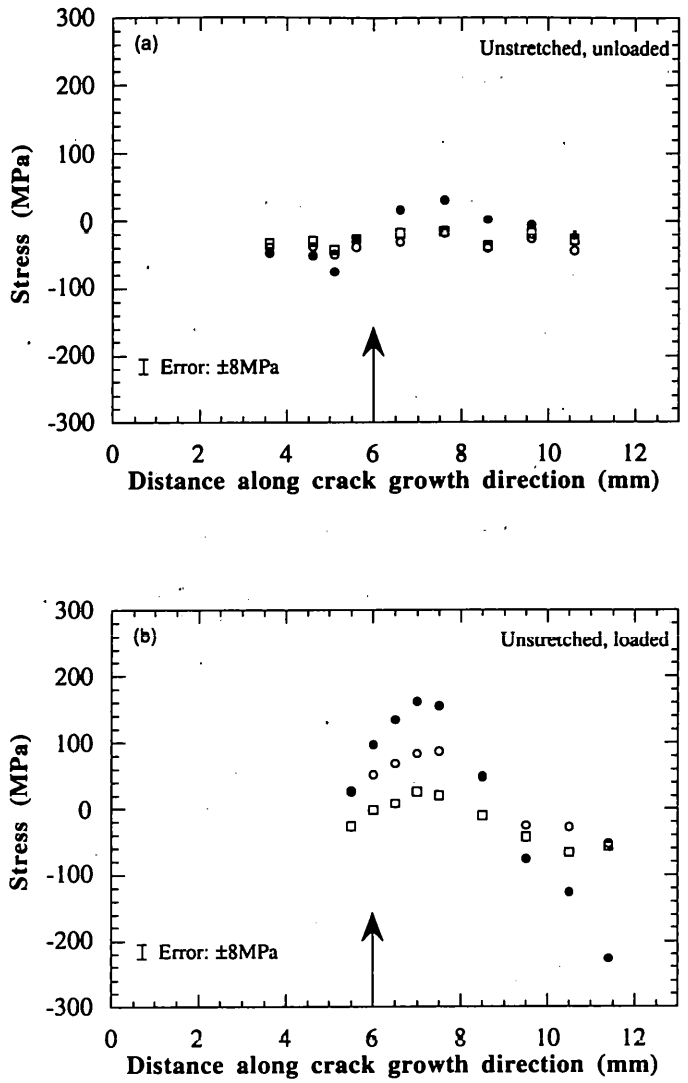

Figure 5.18: Calculated macrostresses in the three principal directions for the unstretched specimen: (a) unloaded and (b) loaded to K_{max}. The arrow indicates the position of the crack tip.

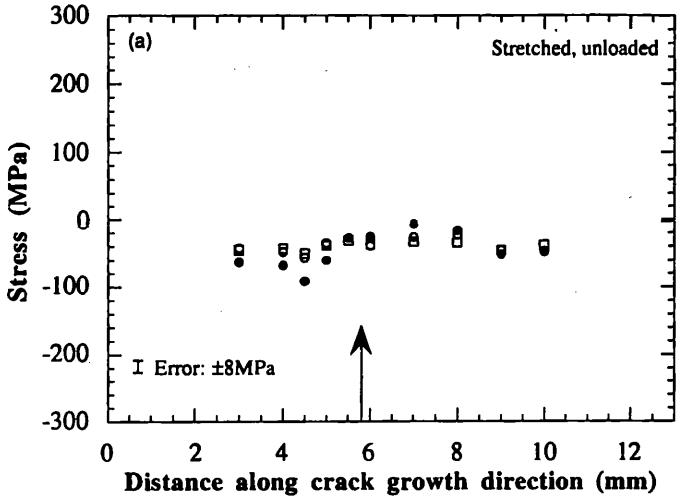

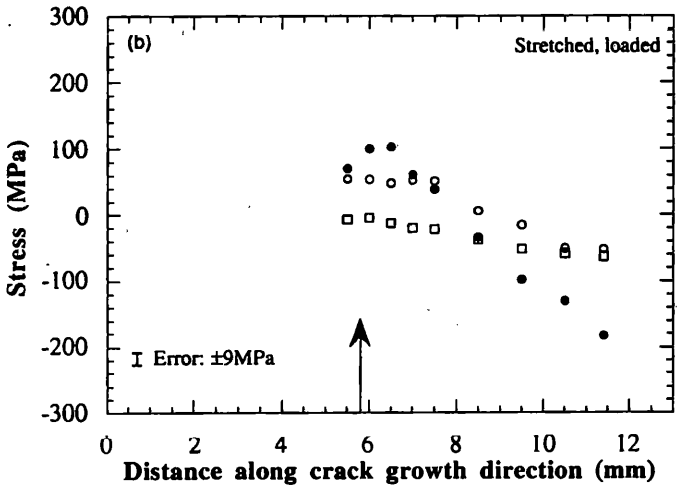

□: σ_x ●: σ_y ○: σ_z

Figure 5.19: Calculated macrostresses in the three principal directions for the stretched specimen: (a) unloaded and (b) loaded to K_{max}. The arrow indicates the position of the crack tip.

The concentration of the applied bending load near the crack tip in all three directions is obvious from the figures. Although the unstretched composite appears to have been loaded to a greater degree than the stretched, comparison with the stress levels when unloaded shows that this is not so.

The calculated macrostresses were then used to obtain the elastic mismatch stresses that exist in each phase, arising from the unequal elastic constants of the two phases. Once these

stresses are determined, subtracting them and the macrostresses from the measured total stresses, as described in Chapter 2, will leave the shape misfit components. These are shown for the two phases in figures 5.20, 5.21 and 5.22 for the x, y and z-directions respectively. It should be mentioned here that the shape misfit stress is assumed to consist of only the thermal misfit part in the unstretched specimen. But plastic misfit terms of opposite natures in both phases, as described in Section 2.7.1, will contribute to the shape misfit stresses in the plastically stretched specimen.

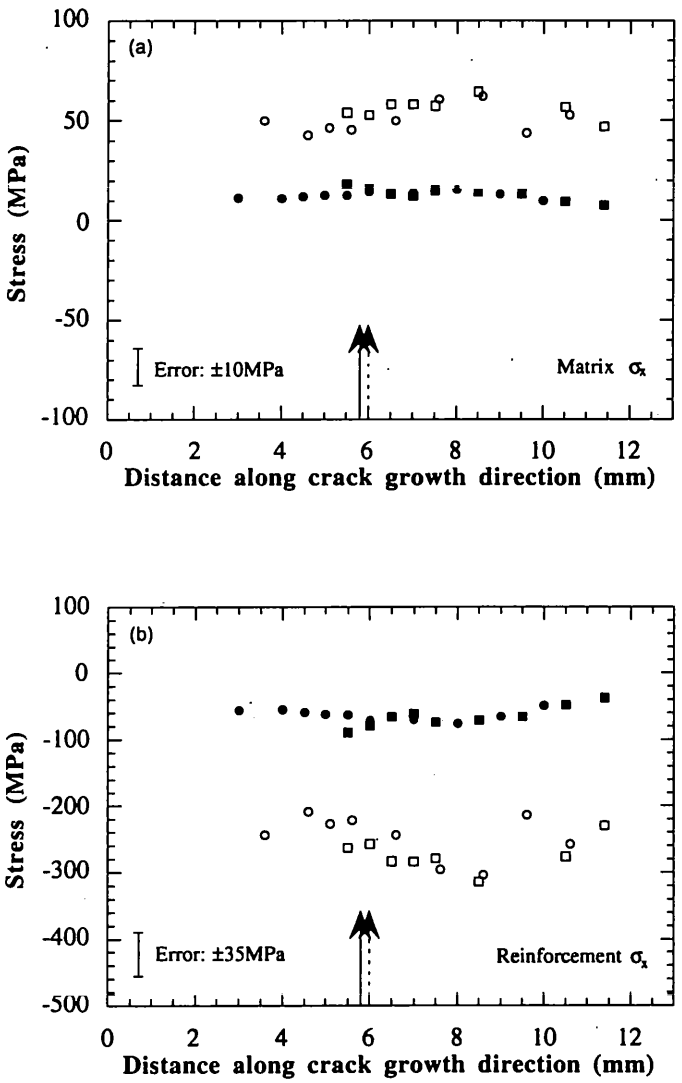

○: unloaded, unstretched; □: loaded, unstretched; ●: unloaded, stretched; ■: loaded, stretched

Figure 5.20: Calculated shape misfit stresses in the transverse or x-direction for unstretched and stretched bars in the (a) matrix and (b) reinforcement. The arrows indicate the position of the crack tip: the broken line for the unstretched specimen and the solid line for the stretched one.

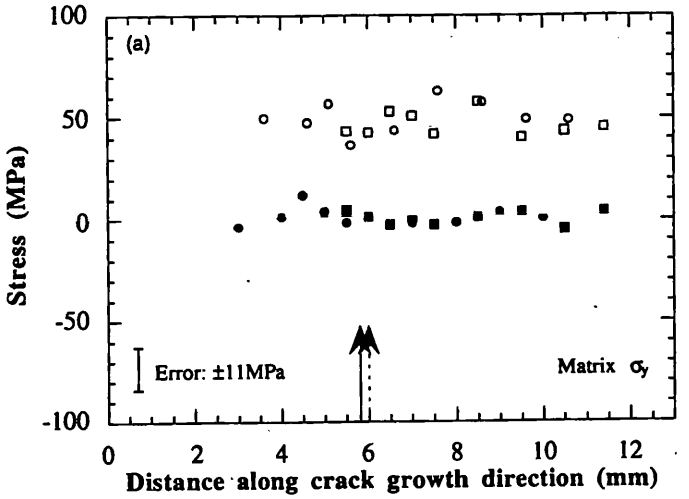

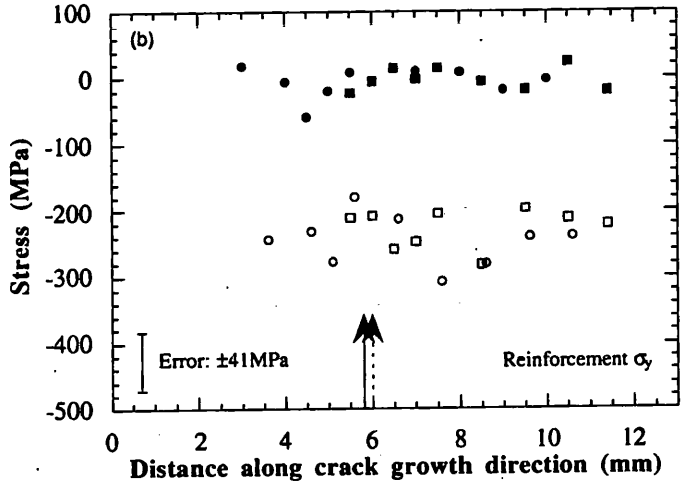

○: unloaded, unstretched; □: loaded, unstretched; ●: unloaded, stretched; ■: loaded, stretched

Figure 5.21: Calculated shape misfit stresses in the longitudinal or *y*-direction for unstretched and stretched bars in the (a) matrix and (b) reinforcement. The arrows are as described in the previous figure.

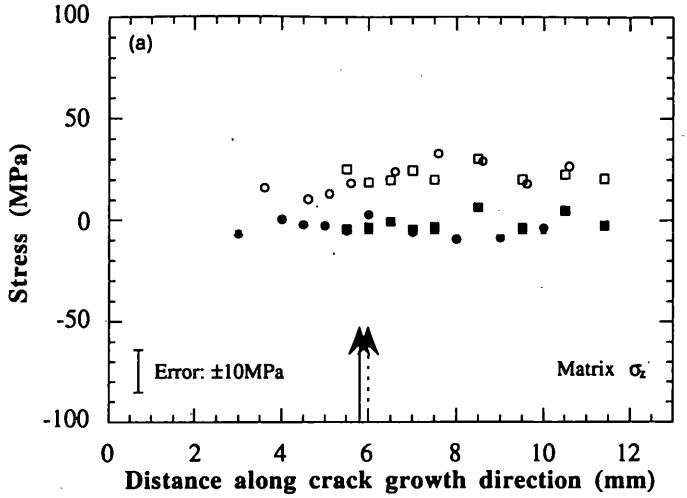

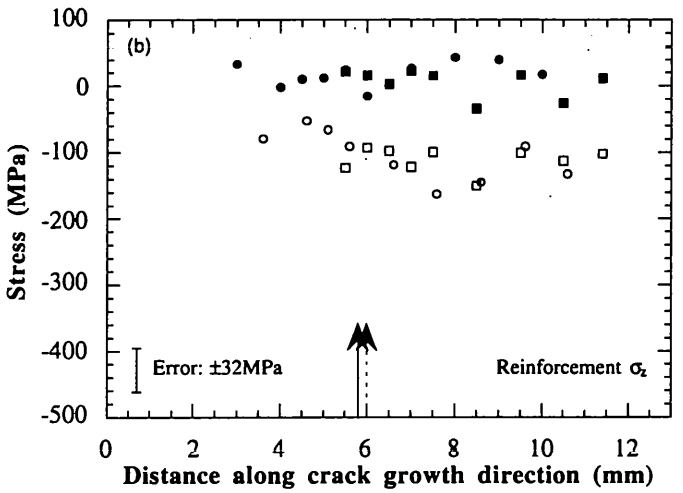

○: unloaded, unstretched; □: loaded, unstretched; ●: unloaded, stretched; ■: loaded, stretched

Figure 5.22: Calculated shape misfit stresses in the depth or z-direction for unstretched and stretched bars in the (a) matrix and (b) reinforcement. The arrows are as described in figure 5.20.

Some interesting points should be noted from these figures. The thermal misfit stresses in these samples are known from the calculated shape misfit stresses in the unstretched specimen. They are found to be almost constant throughout the thickness at ~+50 MPa in the matrix and ~–250 MPa in the reinforcement in the x and y-directions. One may expect a hydrostatic nature of the thermal misfit stress in this particulate reinforced MMC. However, the values in both the matrix and reinforcement in the z-direction are half of those found in other directions; the reason is not very clear.

The calculated shape misfit stress in the stretched specimen provides clear evidence that plastic deformation has had the effect of changing the thermal misfit stress in the composite. The plastic misfit stresses, having acted in the opposite sense of the thermal misfit stresses, have reduced the latter to near zero in both phases in the y and z-directions and to a lesser extent in the x-direction. If it is assumed that the thermal and plastic misfit terms are the only contributors to the shape misfit stresses, then it can be inferred that a 1% plastic deformation by a tensile load along the y-direction in this Al-SiC_p MMC produces a plastic misfit stress of ~–50 MPa in the matrix and ~+250 MPa in the reinforcement in the same direction. No effect of a fatigue crack on misfit stress was observed in this study.

The success of the separation method is reflected in that there is no change in the calculated misfit stress when the sample is loaded. The shape misfit stress component is independent of any elastic loading stresses, and the loading of the sample should not produce any change in this stress component. Interestingly, the passage of the crack has not altered the misfit stress in the crack wake in the unstretched material, despite the plasticity which is associated with fatigue crack growth. This is doubtless a reflection of the degree of localisation of this plasticity, which is restricted to ~100 μm either side of the crack line as discussed earlier (Section 5.3.1). The neutron sampling volume is much larger than this, extending up to 2 mm away from the crack path. The method does not, therefore, have sufficient resolution to be able to detect changes in the misfit stress on that scale.

5.4 DISCUSSION: FATIGUED SPECIMENS

It is clear from the above results that there is an intensification of measured total stress at the crack tip, particularly in the loaded specimens. This crack tip stress intensity arises entirely from the effect of concentration of the macrostress at the crack tip (figures 5.18(b) and 5.19(b)), not from any microstress effects. The macrostress mainly comes from the external load and the intensity of the crack tip stress is therefore more prominent in the

loaded specimens. Microstresses, *i.e.* the thermal misfit and the plastic misfit stresses, are independent of the presence of the fatigue crack. They are uniform throughout the depth along the crack growth direction.

The thermal and plastic misfit stresses in both phases are opposite in nature to each other. The plastic deformation by stretching reduces the effective shape misfit stress uniformly. This, in turn, alters the total stresses by a constant amount through the depth of the specimen. The effect of the stretch has therefore had a large effect on the near-crack tip stress in both phases, especially in the loaded condition. Reducing the tensile residual stress in the matrix has reduced the overall matrix stress at the crack tip, while the effect in the reinforcement is that the crack tip reinforcement stress is larger, as a result of the removal of the previously-compressive residual stress. It is not yet clear what, if any, effect this change in stress has on the macroscopic properties of the material. Previous work in this area has not yielded consistent results. For example, Levin and Karlsson [11] reported improved fatigue crack growth resistance in an Al6061/SiC composite after a 0.33% pre-strain, which was attributed to a change in the measured levels of crack closure. However, Beyer *et al.* [12] report a reduction in the overall fatigue life of a similar MMC following a pre-strain.

This may be a reflection of different mechanistic effects, depending on whether the fatigue crack growth properties or the fatigue life properties are studied. In the early stages of fatigue crack formation, where the plastic zone is small, the presence of the compressive stress in the reinforcement may lead to arrest of small cracks; and any reduction in this compressive stress from plastic deformation may increase the growth of cracks shortly after initiation, so leading to an overall reduction in the fatigue life of the material. If the crack growth is considered once the crack is growing in the Paris régime, however, removal of the pre-existing net tensile stress in the matrix may have the effect of reducing the plastic zone size, thereby reducing the rate of fatigue crack growth.

A critical element to any of these possible mechanisms, is the consideration of whether the shape misfit stress does indeed affect the fatigue propagation. If fatigue crack growth is driven by the size of the cyclic plastic zone produced during fatigue loading, then the yielding of the matrix within the forward plastic zone at P_{max} (the peak load during the fatigue cycle) will alleviate the misfit stress before reverse yielding occurs during the unloading portion of the cycle.

5.5 RESULTS: HEAT TREATED SPECIMENS

In this section, the experimental results on the effect of different heat treatments after a plastic deformation on the macro and micro stresses in composites will be presented. Table 5.2 in Section 5.2 may be recollected for the details of heat treatments. But first, the relaxation of the thermally induced strains and stresses produced by a plastic deformation by a four-point bending load, as measured during examining the liquid nitrogen-treated specimen at ILL, will be presented. Since the longitudinal or y-direction is the most important in these bent specimens, plots of measured strains and calculated stresses only in this direction will be presented here. Plots for the other two directions are shown in Appendix I.

5.5.1 Measured Strains

The matrix strains in the longitudinal or y-direction for the quenched and naturally aged (Q+NA) and as-deformed specimens, are shown in figure 5.23. The dotted line indicates the back surface of the as-deformed specimen. The Q+NA specimen shows tension at the middle of the specimen, which tends to become compressive towards the surfaces: as expected in a quenched block. During the four-point bending, the longer span was applied on the front face of the specimens, *i.e.* the zero on the abscissa, and the shorter span on the back face which is at ~18 mm on the abscissa. On removal of the bending load after the

plastic deformation, the state changes to a compression-tension-compression-tension pattern from the surface with longer span to the surface with the shorter span, as can be seen in the as-deformed specimen in figure 5.23. The existing fitting program at ILL did not provide the uncertainty values of the fitting results; hence no errors are shown in this plot. The program will be updated soon to overcome this deficiency. However, the smooth profile obtained indicates that any errors are not unduly large.

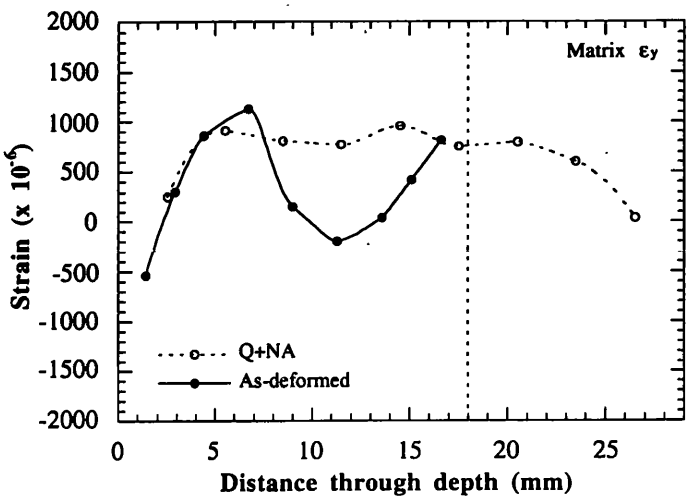

Figure 5.23: Measured matrix strains in the longitudinal (y) direction of the quenched and naturally aged (Q+NA) and the as-deformed specimens through the depth. The dotted line indicates the back face of the as-deformed specimen. No uncertainty values were available from the existing fitting program at ILL; hence no error bars.

Quenching this bent specimen in liquid nitrogen from room temperature and bringing it back again to room temperature did not make any significant change in the strain values in either phase. They are not presented here. However, this will be discussed in terms of calculated stresses in the next section.

Figure 5.24 shows the longitudinal strains, measured at ISIS, in both the matrix and reinforcement for all heat treated and the as-deformed samples through their depth (z-axis). The expected tension in the matrix and compression in the reinforcement generated by the initial water quench of the composite block from a high temperature, can be observed. The general trend of a plastic four point bending load is clearly visible in both phases of the as-deformed specimen (filled circles in the figure). Similarly, the tensile nature of the matrix is

also observed in the transverse (x) direction (figure A1.1 in Appendix I). In the depth or z-direction, the matrix is slightly compressive, probably because of the Poisson effect (figure A1.2 in Appendix I).

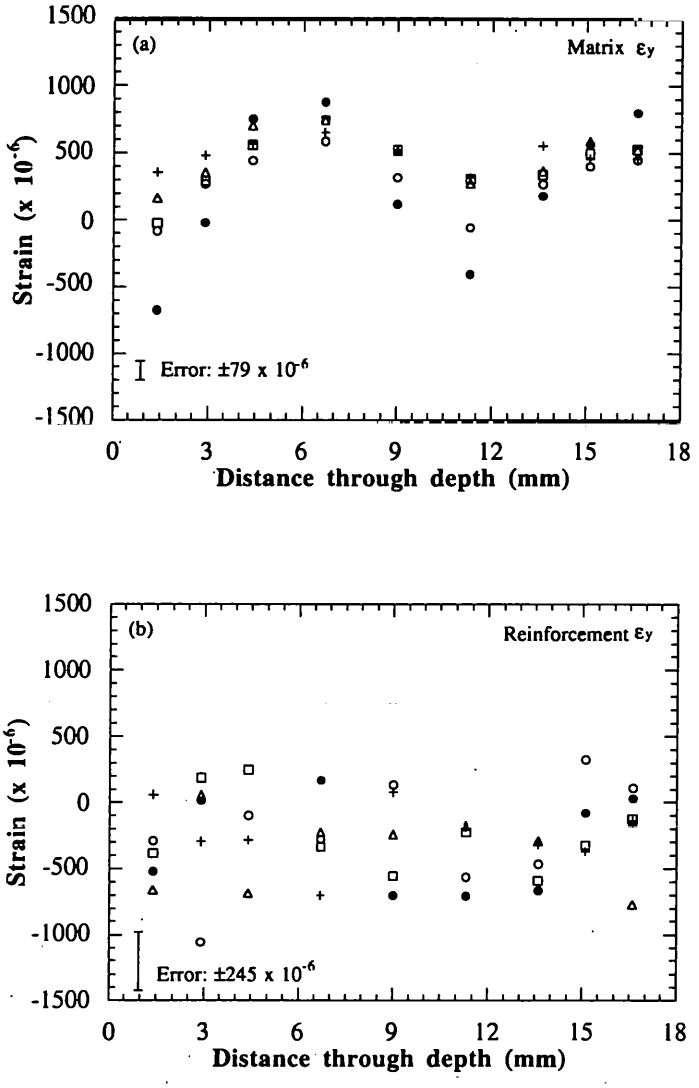

●: as-deformed; ○: 48h @ 180°C; □: 0.5h @ 240°C; △: 2h @ 240°C; +: 0.5h @ 300°C

Figure 5.24: Measured strains in the longitudinal or y-direction in the (a) matrix and (b) reinforcement of the as-deformed and heat treated specimens through the depth.

The reinforcement however, maintains its compressive nature in all three directions. The average error values for each phase are shown, instead of individual errors for every point, for clarity of the plots. High error values can be attributed to the smaller counting time for each experiment (~30 minutes compared to ~90 minutes for the first set of experiments). An indication of the change in strain (stress), caused by different heat treatments can be noticed. These effects will be more clear in dealing with the stresses in the next section.

5.5.2 Calculated Total Stresses

The calculated total stresses in the matrix of the Q+NA and the as-deformed specimens, are shown in figure 5.25. Typical profiles of residual stress arising from quenching an MMC block and four point bending are seen in the Q+NA and as-deformed specimens. The mean values of all measured points in a specimen, shown as horizontal lines in the figure, indicate that the 0.33% plastic deformation in the MMC bar has relaxed the total stress in the matrix from 115 MPa to half (57 MPa). This occurs because of the reduction in thermal misfit stress in regions which undergo plastic deformation.

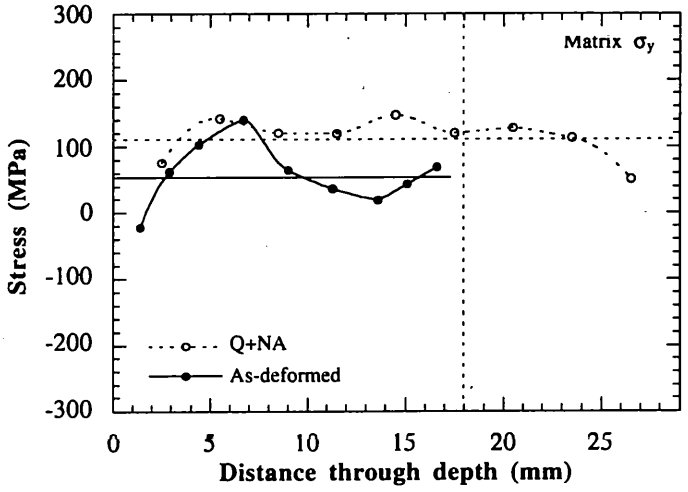

Figure 5.25: Calculated total matrix stresses along with their mean values (horizontal lines) in the longitudinal (y) direction of the quenched and naturally aged (Q+NA) and the as-deformed specimens through the depth. The vertical dotted line indicates the back face of the as-deformed specimen. No uncertainty values were available from the existing fitting program at ILL; hence no error bars.

Measurements at the same positions in the as-deformed specimen were performed both at ISIS and at ILL. These measurements produced almost identical results as can be seen in figure 5.26. Because of non-availability of the uncertainty values of the fitting results from ILL, the errors are not shown in the plot; however, the small differences might be well within the error bars. This highlights the accuracy of the strain measurement by the neutron diffraction technique, irrespective of the source of neutrons (a reactor source or a spallation source). However, the agreement in results is not so good for the reinforcement phase, as

can be seen in figure A1.3 in Appendix I. The same is true for the comparisons of results in other two directions, *i.e.* good agreement for the matrix but not so good for the reinforcement.

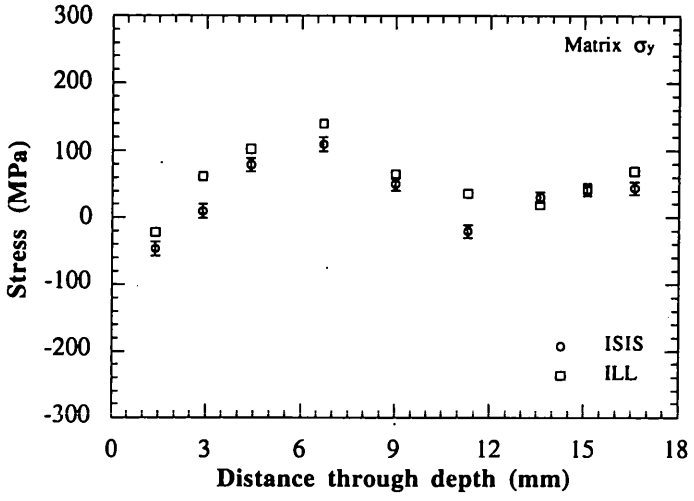

Figure 5.26: Comparison of calculated total matrix stresses in the longitudinal (*y*) direction of the as-deformed specimen through the depth, measured at ISIS and ILL.

As mentioned in the previous section, the treatment of the deformed specimen in liquid nitrogen did not generate a noticeable change in the stress state. The calculated total stresses in the specimen before (as-deformed) and after the treatment are compared in figure 5.27. Any small changes may result from a slight positional error during the measurement. The drop in temperature was not enough to produce a plastic deformation in this 2124 Al alloy matrix, which might alter the stress states. This will be further discussed in the following section.

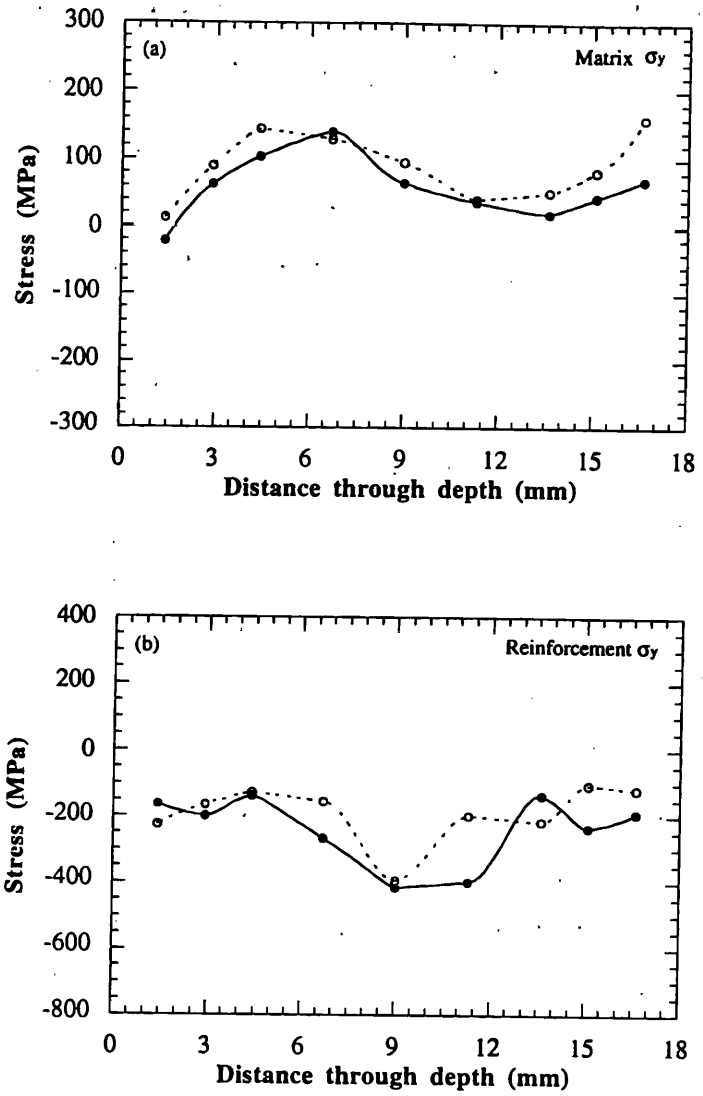

Figure 5.27: Calculated total stresses in the longitudinal or *y*-direction through the depth in the (a) matrix and (b) reinforcement of the deformed specimen before (as-deformed) and after the liquid nitrogen treatment. No uncertainty values were available from the existing fitting program at ILL; hence no error bars.

The calculated total stresses in the heat treated specimens are shown in figure 5.28. A typical residual stress pattern after a plastic four point bending can be noticed in the matrix of the as-deformed specimen (filled circles in the figure). The trend is also apparent in the reinforcement. The matrix stress is generally tensile in nature; whereas the reinforcement stress is compressive, as expected in an MMC. In the matrix, the first point is an exception with negative stress, which might be due to the compressive stress at the surface from bending effect. Similar natures of the total stresses were also found in the other two directions (figures A1.4 andA1.5 in Appendix I).

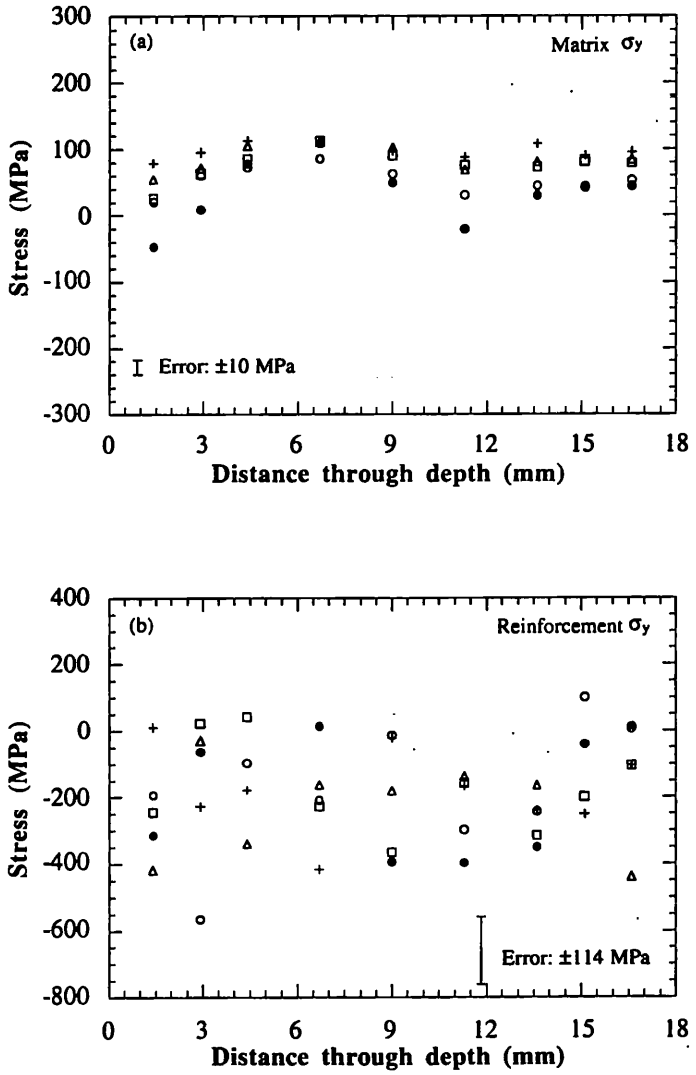

●: as-deformed; ○: 48h @ 180°C; □: 0.5h @ 240°C; △: 2h @ 240°C; +: 0.5h @ 300°C

Figure 5.28: Calculated total stresses in the longitudinal or *y*-direction in the (a) matrix and (b) reinforcement of as-deformed and heat treated specimens through the depth.

The effect of different heat treatments is prominent in figure 5.28(a). The total stress in the matrix gradually becomes more positive as the heat treatment time and temperature increase. This is a combined effect of relaxation of the macrostress and reinstatement of the positive thermal misfit stress by the heat treatment. In the reinforcement, the effect is not so clear from this figure as the set of stress values for individual specimens are not well defined. But the mean value of all measured points through the depth in each specimen indicates that the heat treatments gradually increased the compressive reinforcement stress from –135 MPa to a maximum of –235 MPa. Similar effects of the heat treatments in increasing the phase stresses in the other two directions were obtained (figures A1.4 and A1.5 in Appendix I).

As the plastic bending produced a variable stress state through the depth in both the matrix and reinforcement, and almost the same amount of plastic deformation had been introduced in all the specimens before heat treatment, it is interesting to see if there is any effect of the magnitude of the initial stress state in the phases on the change made by heat treatments. This is shown in figure 5.29, where the change in phase stresses has been plotted against the initial stress at the same points as found in the as-deformed specimen. A clear linear relation between the initial stress and the amount of change in stress made by the heat treatments is evident in both phases. If the initial stress is more positive (or less negative), heat treatment produces a more negative stress change in the matrix and vice-e-versa. In the reinforcement, the more negative the initial stress, the more positive is the change. It is also clear from figure 5.29(a) that higher treatment temperature (and time) generates more positive changes in the matrix.

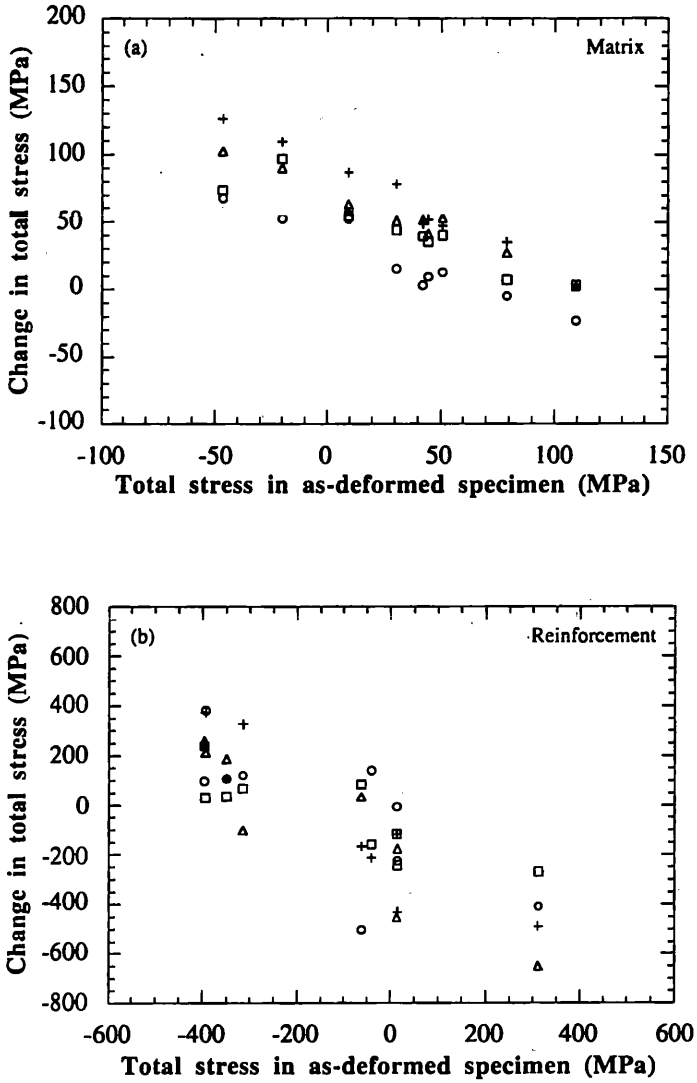

o: 48h @ 180°C; □: 0.5h @ 240°C; ▵: 2h @ 240°C; +: 0.5h @ 300°C

Figure 5.29: Change in total stresses in the longitudinal or *y*-direction due to heat treatment, from the initial states as found in the as-deformed specimen in the (a) matrix and (b) reinforcement.

5.5.3 Macro and Micro Stress Components

The macro and micro stresses were separated from the total phase stresses following the method described in Chapter 2. The macrostresses in the longitudinal direction are plotted in figure 5.30 for all specimens. The maximum variation of macrostress through the depth, following the four point bending pattern, can be noticed in the as-deformed specimen. As

one would expect for this simple specimen geometry, the integral of the macrostress components are close to zero in all specimens. Slight variations can be attributed to any small errors in the strain-free lattice parameters. It is interesting to note the effect of heat treatment: the macrostress has relaxed after heat treatment and the relaxation is proportional to the treatment temperature (and time) as illustrated in table 5.3. Similar effects have also been obtained in the other two directions as shown in Appendix I (figure A1.6).

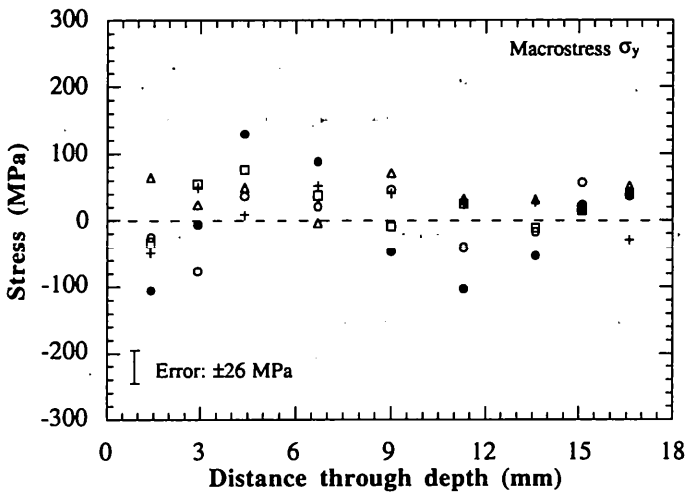

●: as-deformed; ○: 48h @ 180°C; □: 0.5h @ 240°C; △: 2h @ 240°C; +: 0.5h @ 300°C

Figure 5.30: Calculated macrostresses in the longitudinal or *y*-direction of the as-deformed and heat treated specimens through the depth.

Heat treatment	As-deformed	48 h @ 180°C	0.5 h @ 240°C	2 h @ 240°C	0.5 h @ 300°C
Difference between the maximum and minimum macrostress (MPa)	235	133	109	100	75

Table 5.3: Effects of heat treatment on the macrostress as manifested by the difference between the maximum and minimum values.

The integrals of macrostress values through the depth in the specimens measured at ILL, were also close to zero. But no considerable change in macrostresses was obtained after the liquid nitrogen treatment (shown in Appendix I (figure A1.7) for the longitudinal direction).

The shape misfit stress is entirely thermal in nature in the Q+NA specimen and a combined effect of thermal and plastic misfit stresses in all other deformed and heat treated specimens. The mean values of this misfit stress through the depth in the starting material, *i.e.* the Q+NA specimen were 100 MPa in the matrix and −356 MPa in the reinforcement (not shown here). Figure 5.31 shows the variation of the longitudinal shape misfit stresses across the depth in the deformed specimen before and after the liquid nitrogen treatment.

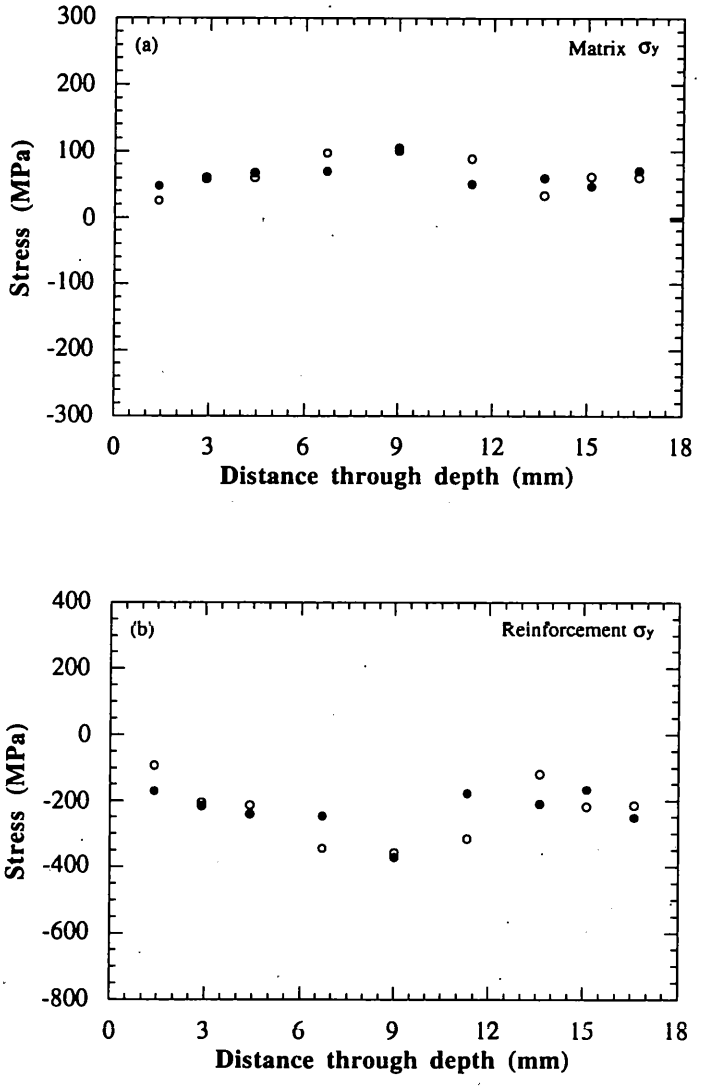

●: as-deformed; ○: deformed and quenched in N_2

Figure 5.31: Calculated shape misfit stresses in the longitudinal or *y*-direction through the depth in the (a) matrix and (b) reinforcement of the deformed specimen before (as-deformed) and after the liquid nitrogen treatment.

There was hardly any effect of the liquid nitrogen treatment on misfit stresses, as seen in the plots. The misfit stress field is unchanged with constant mean values in both phases. But these mean values are much lower than those obtained for the Q+NA specimen, which is an effect of the plastic deformation. This will be discussed further in the next section.

The misfit stresses in the longitudinal direction for all other heat treated specimens and the as-deformed specimen are shown in figure 5.32. It is interesting to note that the heat treatment gradually increases the total misfit stresses in both phases which were initially lowered by the plastic deformation.

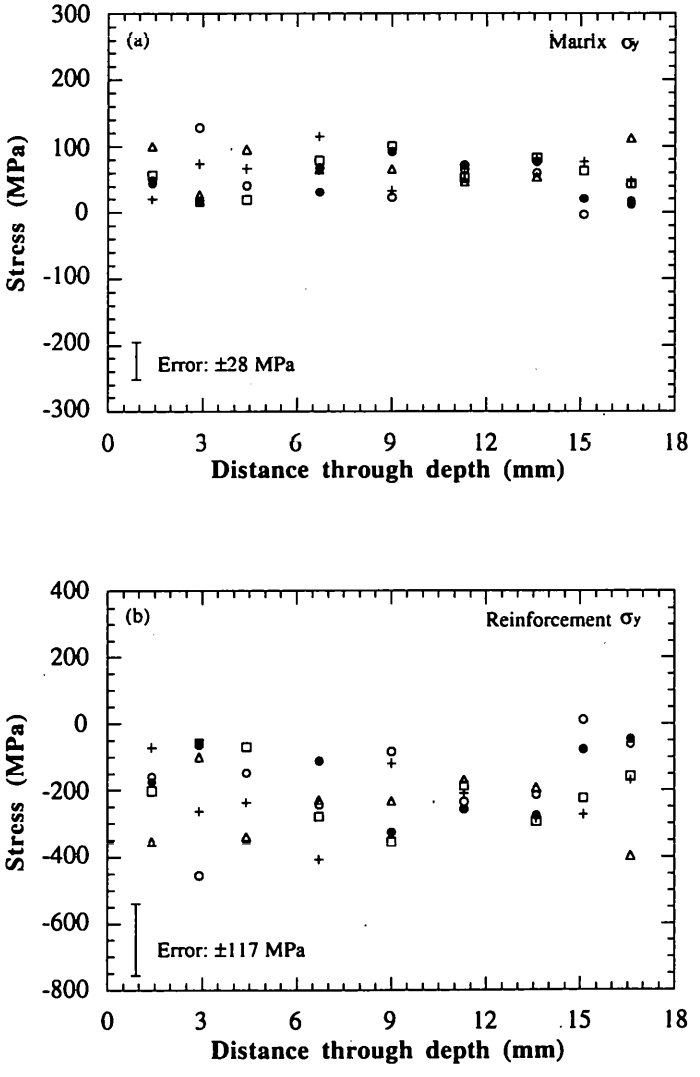

●: as-deformed; ○: 48h @ 180°C; □: 0.5h @ 240°C; △: 2h @ 240°C; +: 0.5h @ 300°C

Figure 5.32: Calculated shape misfit stresses in the longitudinal or *y*-direction in the (a) matrix and (b) reinforcement of as-deformed and heat treated specimens through the depth.

5.6 DISCUSSION: HEAT TREATED SPECIMENS

The results in the previous section show how the macro and micro stresses are modified by different heat treatments in an Al-SiC_p composite after plastic deformation. The thermal residual stresses were first partially relaxed near the surfaces by introducing about 0.33% plastic deformation in all specimens by four-point bending, which also introduced a macrostress variation through the depth. In the first set of experiments with the fatigued specimens, it was found that a 1% plastic deformation by a uniaxial tensile load could result in a total relaxation of the shape misfit stresses in the longitudinal direction. In this case, a plastic deformation of ~0.33% relaxes the shape misfit stresses by ~35% in the longitudinal direction, as can be seen in table 5.4. A significant amount of relaxation in the Al-SiC_p system at low strains was also mentioned by others [13]. Although it is not yet established if a linear relation exists between the amount of plastic deformation and this stress relaxation, it can be seen here that 0.33% plastic deformation by a four-point loading is sufficient for 35% relaxation of the mean misfit stresses. However, a complete relaxation is not possible by a four-point bending as it leaves the neutral axis unyielded. The mechanism of relaxation may be plastic flow in the matrix which reduces the shape misfits between the phases or the generation of plastic misfit stresses of opposite nature to that of thermal misfit stresses, as explained in section 2.7.1.

Specimen	Mean shape misfit stress (MPa)	
	Matrix	Reinforcement
Q+NA	100	-356
As-deformed	65 (–35%)	-231 (35%)
Deformed and quenched in liquid N_2	64 (–36%)	-228 (36%)

Table 5.4: Mean values of shape misfit stresses through the depth in both phases of quenched and naturally aged (Q+NA) and the deformed specimen before (as-deformed) and after treated in liquid nitrogen. Figures within parentheses are the changes in misfit stress.

Interestingly, quenching this deformed specimen in liquid nitrogen (–196°C) from room temperature and then bringing it back to room temperature does not make any change in the misfit stress. It is possible to calculate the thermal misfit stress generated from this temperature drop as described by Fitzpatrick *et al.* [3]. For this MMC with 22 vol% SiC, it was found that a quench in liquid nitrogen (–196°C) from room temperature (25°C) can generate a misfit stress of ~80 MPa in the 2124 Al alloy matrix, which is much less than its yield strength (~400 MPa) [14]. The drop in temperature is therefore not sufficient to generate any plastic deformation in the matrix, which, in turn, can alter the shape misfit stress. However, a plastic deformation assisted relaxation in both the matrix and reinforcement after a liquid nitrogen treatment was reported by Sun *et al.* [15] in a similar composite system; but with a much softer matrix of pure aluminium. The thermal misfit stresses originated during the cooling probably reverted back to their original values after reheating the specimen to room temperature.

Heat treatment of the deformed specimens relaxes the macrostress, which has already been shown in figure 5.30 and table 5.3. The probable mechanism of stress relaxation at higher temperature in this particulate reinforced MMC is mass diffusion in the matrix [16]. Various amounts of macrostress were found after four point bending of the specimens, the as-deformed specimen being the representative. This gives an opportunity to examine the effect of the initial amount of macrostress on its relaxation by heat treatment, as can be seen in figure 5.33. The changes in macrostress values from the original ones, found at identical positions in the as-deformed specimen are plotted against the original values. It is very interesting to note that the points from each heat treated specimen are close to the –45° line or the line for complete relaxation (the axes are in the same scale). This suggests that the more the initial macrostress, the more will be the relaxation. The deviations from the –45° line reflect incomplete relaxation of the macrostress. Ideally, the points for each set of heat treatment should have been spread over both sides of the line, for a balanced state of the macrostress. Although a greater fraction of the points which are above the –45° line belong to the treatments at higher temperature, no conclusion can be drawn in this regard.

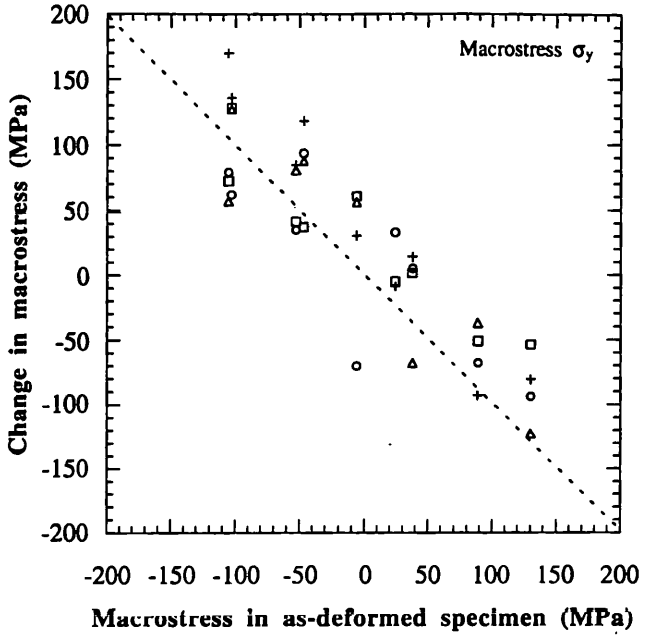

o: 48h @ 180°C; □: 0.5h @ 240°C; ▵: 2h @ 240°C; +: 0.5h @ 300°C

Figure 5.33: Change in macrostresses in the longitudinal or *y*-direction due to heat treatments, from the initial states, as found in the as-deformed specimen.

It was seen that the plastic deformation reduced the thermal misfit stress by about 35% in both phases, which was regenerated after heat treatment. In fact, it is the cooling of the hot specimens in air after heat treatment, which generates the thermal misfit stress. The regeneration of misfit stress increases with treatment temperature. As a specimen is heated and cooled down again to room temperature during the heat treatment, changes occur in the stress states in both phases of the composite, as shown schematically in figure 5.34. As the temperature increases from room temperature (A or M) to the treatment temperature, the matrix gradually goes towards compression and the reinforcement towards tension (B and N), owing to the difference in thermal expansion coefficients between the phases. For a composite with a given difference in the coefficients of thermal expansion between the phases, the slope and length of AB and MN will depend on the initial phase stresses and treatment temperature. When the specimen is held at higher temperature for a certain time, diffusion-based relaxation takes place and the phases come to a lower stress state (C and O). The length of BC and NO depends on treatment temperature and holding time (until the relaxation process is complete). On cooling again to room temperature, tensile stress in the

matrix and compressive stress in the reinforcement develops (D and P) from the shape misfits of the two phases during the contraction. Room temperature relaxation of phase stresses is possible after such heat treatments [17]. The final stress states are therefore E and Q for the matrix and reinforcement respectively, which may be higher than the original ones. In this study, the initial stress states A and M have been calculated from the measurements in the as-deformed specimen and the final states E and Q have been obtained from the individual heat treated specimens at many points through the depth.

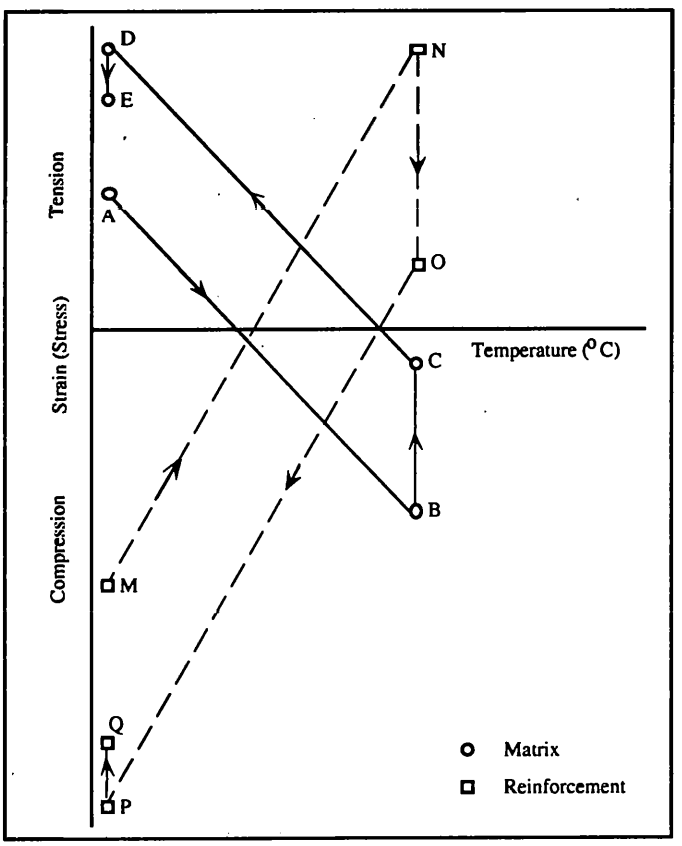

Figure 5.34: Schematic diagram for the change in strain (stress) states in both matrix and reinforcement occurring during the thermal cycle: room temperature-heat treatment temperature-room temperature.

Once the MMC specimens reach the heat treatment temperature, the stress states go through two opposite phenomena: relaxation of the macro and micro stresses during the holding time, and regeneration of the misfit stress during air-cooling of the specimens. The amount of this diffusion-based relaxation (*i.e.* the length of BC or NO in figure 5.34) is higher at higher temperature. However, the attainment of the maximum possible length of BC or NO (*i.e.* maximum relaxation) at a particular temperature may not be possible if the treatment

time is too short. If only the regeneration of thermal misfit stress by cooling the specimens in air is considered, higher treatment temperature may not have any effect on the final stress states, as long as CD and OP are considered parallel to AB and MN respectively. But they may not be essentially parallel as the stress values after cooling are sometimes less than these theoretical levels (D and P), as observed by Lorentzen *et al.* [17] in an Al based composite reinforced with SiC whiskers. The relaxation therefore seems to be mainly responsible for the final levels of misfit stresses. From the Arrhenius equation for the coefficient of diffusion, D:

$$D = Ae^{\left(-\frac{Q}{RT}\right)} \qquad \text{(Equation 5.2)}$$

where, A is the frequency factor; Q is the activation energy; R is the gas constant and T is the temperature in Kelvin, and from the values for Al of A=2.25 cm^2s^{-1}, Q=34.5 $kcal\,mol^{-1}$ and R=1.987 $cal\,mol^{-1}K^{-1}$ [18], different values for D are obtained at different heat treatment temperatures as shown in table 5.5.

Treatment temperature (°C)	Coefficient of diffusion, D (cm^2s^{-1})
180	5.08×10^{-17}
240	4.50×10^{-15}
300	1.56×10^{-13}

Table 5.5: Coefficients of diffusion at different heat treatment temperatures as calculated from the Arrhenius equation.

Table 5.5 shows that the coefficient of diffusion increases by four orders of magnitude as the treatment temperature increases from 180°C to 300°C. It is therefore expected that the relaxation will be much more at higher temperature because of the enhanced diffusion.

It is important to mention again (as done in section 5.3.3) about a common problem in strain measurement by the neutron diffraction technique, that is to obtain the strain free reference value. The lattice parameter of aluminium is very sensitive to the presence of solute atoms

[10]. Even if the alloy composition of the powder is correct, as in this case, it is virtually impossible to assure about the same proportion of the alloying elements actually in solid solution since the high temperature ageing characteristics are different for the reinforced and parent alloys [4-6, 19, 20], which may create an error in evaluating the strain free lattice parameter. However, the error may not be significantly large; a nominal change of ~100 microstrain in the matrix was observed by Hermann *et al.* [21] in an Al-3.5 wt%Cu/SiC_p (20 vol%) MMC after heating it at 230°C for several hours. In comparison, the measured strain in the matrix here is in the range of 500-1500 microstrain. Moreover, the effects of the presence of Cu and Mg atoms on the Al-alloy lattice spacing are opposite to each other and of similar magnitude [10]. As the atom percents of Cu (~1.8%) and Mg (~1.7%) in this 2124 Al alloy matrix are similar, the overall effect may be neutralised. The results presented in this study therefore should not be affected much by any d_0 problem.

The overall effect of different treatment temperatures and time on the final values of misfit stress is not very clear in figure 5.32. But if the mean values through the depth of each specimen are compared, as shown in table 5.6, an obvious effect can be noticed.

Specimen	Mean shape misfit stress (MPa)	
	Matrix	Reinforcement
As-deformed	47	-166
48h @ 180°C	50 (6%)	-176 (–6%)
0.5h @ 240°C	57 (21%)	-202 (–22%)
2h @ 240°C	71 (51%)	-251 (–51%)
0.5h @ 300°C	64 (36%)	-225 (–36%)

Table 5.6: Mean values of shape misfit stresses across the depth in both phases of the as-deformed and heat treated specimens. Figures within parentheses are the changes in misfit stress by heat treatment.

The low temperature (180°C) treatment can relax partially both macrostress and misfit stress by assisting the relaxation over a long a period of time (48 hours). In this case, BC and NO in the previous figure perhaps attain their maximum possible lengths at 180°C, which may be very small, and the positions of D and P become close to A and M respectively. Therefore, hardly any change is observed in the misfit stresses (table 5.6). With the increase in temperature, more relaxation of the misfit stress occurs, which brings D and P (E and Q finally) further away from the respective starting points. As mentioned earlier, the holding time plays an important role in determining the lengths of BC and NO, *i.e.* the relaxation. Holding for 30 minutes is probably not sufficient to produce the maximum possible relaxation at a particular temperature. Therefore, a moderate increase in thermal misfit stresses can be noticed in table 5.6 for the specimen treated at 240°C for 30 minutes and even for that treated at 300°C. But the values are more in the latter case, because of enhanced rate of diffusion and hence higher relaxation at higher temperature, as discussed earlier. The specimen treated at 240°C for two hours undergoes the maximum amount of relaxation and finally regenerates the maximum amount of thermal misfit stresses in both phases. However, these changes in misfit stress are not proportional to the factor of $\sqrt{Dt}$ (D is the coefficient of diffusion and t is treatment time).

The overall effect of heat treatment is reflected in the total stresses in both phases, which consists of both macrostress and misfit stresses. As the amount of relaxation of the macrostress caused by the heat treatment is less than the overall regeneration of thermal misfit stresses, a general increase in total stresses in both phases of the composite has been seen in figure 5.28.

5.7 SUMMARY

In this Chapter, the measurement and analysis of microlevel stresses in an Al-SiC_p MMC has been presented. The study can be divided into two parts. The effect of plasticity on the internal stresses around a fatigue crack-tip was studied in the first set of experiments. All

macro and micro stress components in both phases in a plastically stretched and fatigue cracked specimen, both unloaded and elastically loaded, were separated from the total stresses measured by neutron diffraction, and were compared with those in an unstretched and cracked specimen. The shape misfit stresses in the unstretched specimen (which are also the thermal misfit stresses in absence of any plastic deformation) in the crack opening direction were found to be +50 MPa in the matrix and –250 MPa in the reinforcement. 1% plastic deformation by a uniaxial stretching of the specimen brings these misfit stresses down to almost zero in both phases. The reason may be attributed to the plastic misfit stresses of opposite nature. With the assumption that the shape misfit stress consists of only the thermal and plastic misfit terms, it can concluded that 1% plastic deformation by a uniaxial tensile load along the longitudinal direction in this Al-17 vol% SiC_p MMC generates a plastic misfit stress of ~–50 MPa in the matrix and ~+250 MPa in the reinforcement. The overall effect of plasticity on the total stresses in the stretched specimen is that the matrix becomes less tensile, whereas the reinforcement becomes less compressive. This may lead to two opposite effects on the material performance. The reduction in compressive reinforcement stress may decrease the arrest of small cracks and thereby may enhance the initial crack growth. However, reduction of the net tensile stress in the matrix may decrease the rate of subsequent fatigue crack growth by reducing the plastic zone size in the Paris régime. No effect of fatigue cracking and elastic loading on the misfit stresses was observed in this study.

In the second part of the study, changes in microstresses (that had already been modified by plasticity) in bent MMC (22 vol% of SiC) specimens caused by different heat treatments have been investigated. A plastic deformation of ~0.33% by a four-point loading reduced the misfit stress by ~35% in both phases, which is regenerated by heat treatment. The relaxation during the heat treatment is mainly responsible for determining the final values of the misfit stress. The regeneration of misfit stresses therefore depends on both treatment time and temperature. Heat treatment also relaxes the macrostress in the specimens. There is a linear relation between the initial macrostress in the specimen and the magnitude of its relaxation by heat treatment with a negative slope of –45°. This means that the relaxation

depends on the amount of initial macrostress, irrespective of the sign. No significant change in the stress states occurs before and after the treatment of the deformed specimen in liquid nitrogen. The thermal misfit stresses in both phases generated by the quench revert back to their original values as the specimen returns to room temperature, and this thermal misfit stress (~80 MPa in the matrix) is not sufficient to generate any plastic deformation in this 2124 Al matrix, which can further alter the shape misfit stresses.

5.8 REFERENCES

1. M. E. Fitzpatrick, Ph. D. Thesis, Dept. of Materials Science and Metallurgy, University of Cambridge, 1995.

2 T. W. Clyne and P. J. Withers, *An Introduction to Metal Matrix Composites*, Cambridge Solid State Science Series, Cambridge University Press, 1993.

3. M. E. Fitzpatrick, M. T. Hutchings and P. J. Withers, *Separation of Macroscopic, Elastic Mismatch and Thermal Expansion Misfit Stresses in Metal Matrix Quenched Plates from Neutron Diffraction Measurements*, Acta Mater., 45 (12), 1997, pp. 4867-4876.

4. M. P. Thomas, D. M. Knowles and J. E. King, *Microstructure/Property Relationships in Al/SiC Particulate Metal Matrix Composites*, in Proc. Euromat 91: Second European Conference on Advanced Materials and Processes, Institute of Materials, 1991, pp. 105-116.

5. S. Suresh, T. Christman and Y. Sugimura, *Accelerated Aging in Cast Al Alloy-SiC Particulate Composites*, Scripta Mater., 23, 1989, pp. 1599-1602.

6. T. Christman and S. Suresh, *Microstructural Development in an Aluminum Alloy-SiC Whisker Composite*, Acta Metall., 36 (7), 1988, pp. 1691-1704.

7. D. Q. Wang, Ph. D. Thesis, Dept. of Materials Engineering, The Open University, 1994.

8. D. Q. Wang and L. Edwards, *Precise Determination of Specimen Surface Position During Sub-Surface Strain Scanning by Neutron Diffraction*, in Proc. Fourth European Conference on Residual Stress (ECRS4), ed. S. Denis *et al.*, SFM, France, 1, 1996, pp. 135-144.

9. S. Suresh, *Fatigue of Materials*, Cambridge Solid State Science Series, Cambridge University Press, 1991, p. 163.

10. H. G. Priesmeyer, *The Stress Free Reference Sample: Alloy Composition Information from Neutron Capture*, in Measurement of Residual and Applied Stress Using Neutron Diffraction, eds. M. T Hutchings and A. D. Krawitz, Kluwer Academic: London, 1992, pp. 277-284.

11. M. Levin and B. Karlsson, *Influence of SiC Particle Distribution and Prestrainig on Fatigue Crack Growth Rates in Aluminium AA6061-SiC Composite Material*, Mater. Sci. Tech., 7, 1991, pp. 596-607.

12. G. Beyer, H. Biermann and H. Mughrabi, *On the Effect of Pre-Straining on the Fatigue Behaviour of a Particulate-reinforced Metal-Matrix Composite*, Scripta Mater. 36 (8), 1997, pp. 935-941.

13. S. F. Corbin and D. S. Wilkinson, *Low Strain Plasticity in a Particulate Metal Matrix Composite*, Acta Metall. Mater., 42 (4), 1994, pp. 1319-1327.

14. Metals Handbook, 10th edn., ASM International, 1990.

15. Z. M. Sun, J. B. Li, Z. G. Wang and W. J. Li, *Residual Stresses in Silicon Carbide Particulate Reinforced Aluminium Composite*, Acta Metall. Mater., 40 (11), 1992, pp. 2961-2966.

16. P. J. Withers, *Relaxation*, in Measurement of Residual and Applied Stress Using Neutron Diffraction, eds. M. T Hutchings and A. D. Krawitz, Kluwer Academic: London, 1992, pp. 205-222.

17. T. Lorentzen, Y. L. Liu and H. Lilholt, *Relaxation of Thermal Induced Internal Stresses in Metal Matrix Composites*, in Ninth International Conference on Composite Materials (ICCM-9), ed. A. Miravete, Madrid, Spain, Vol. 1, University of Zaragoza-Woodhead Publishing Ltd., 1993, pp. 371-378.

18. Smithells Metals Reference Book, ed. E. A. Brandes, 6th edn., Butterworths, 1983.

19. Jun-shan Lin, Peng-xing Li and Ren-jie Wu, *Aging Evaluation of Cast Particulate-Reinforced SiC/Al(2024) Composites*, Scripta Metall. Mater., 28, 1993, pp. 281-286.

20. I. Dutta and D. L. Bourell, *A Theoretical and Experimental Study of Aluminum Alloy 6061-SiC Metal Matrix Composite to Identify the Operative Mechanism for Accelerated Aging*, Mater. Sci. Engng.-A, 112, 1989, pp. 67-77.

21. R. Hermann, D. Q. Wang, M. A. Tomlinson and L. Edwards, *Measurements of Residual Stresses in Metal-Matrix Composites during Heat-Treatment using Neutron Diffraction Techniques*, in Proc. Of the Fourth International Conference on Residual Stresses (ICRS 4), Baltimore, MA, Society for Experimental Mechanics, 1994, pp. 549-558.

CHAPTER 6: CONCLUSIONS

6.1 INTRODUCTION

The aim of this project was to study residual stress in engineering components, both at the macrolevel and microlevel, using the neutron diffraction technique. A classic problem with weld residual stresses in stainless steel pipes used in power plants was chosen for the study of the macrolevel residual stresses. The objective was to see the effect of a repair weld on the pre-existing residual stress fields developed from the original weld. The strain values were therefore measured both in the original weld and repair weld areas of a small diameter (170 mm outer diameter) pipe in three directions and the full stress tensors through the thickness of the pipe were calculated. The measured stresses in the original weld were compared with the predicted values from a finite element analysis performed at British Energy. After the successful measurement in the smaller pipe, a large piece of ex-service pipe (432 mm outer diameter) from a nuclear power plant was also studied at the original weld region.

For the study of the microlevel residual stresses an Al alloy matrix composite reinforced with SiC particles was selected, where large misfit microstresses are generated by a simple quench of the material from a high temperature. This study can be divided into two parts. The objective in the first set of experiments was to study the effect of plasticity on crack-tip stresses, particularly the misfit stresses in the MMC. Two specimens were fatigue cracked; one of them was plastically deformed before fatiguing. The strain values in the three principal directions were measured along the fatigue crack in the samples, both unloaded and elastically loaded in a specially-designed four point loading rig. All the stress components, *i.e.* the macrostress and the microstresses (the elastic mismatch and the shape misfit stresses) were separated to study the effect of plasticity on misfit stress. The aim of the second set of experiments was to study the effect of heat treatment on the misfit microstress that was already modified by plasticity in the MMC. Several specimens of

similar dimensions were plastically deformed (~0.33%) by four point bending and then heat treated at different combinations of time and temperature. They were measured through the depth in the three principal directions parallel to their axes. All macrostress and microstress components were separated to study the effect of heat treatment on misfit stress.

6.2 MACROLEVEL STRESSES IN THE WELDMENT

6.2.1 Residual Stresses in Multipass Welded Pipes

The following conclusions can be drawn from the through-thickness measurements of residual stresses around the original weld regions of the two pipes:

- A large tensile hoop stress was present in the outer half thickness of both pipes. It was found to peak just below the final weld cap pass (at ~14 mm from the inner surface) reaching a maximum value of about 425 MPa (equal to the 0.2% proof stress of the weld metal) in the weld fusion zone and about 300 MPa (equal to the 1% proof stress of base metal) in the HAZ of the small pipe (section 4.3.2). In the large pipe both peak values were found to be ~300 MPa (with an axial stress balance condition) at an identical position (section 4.4.2).
- A nearly sinusoidal distribution of the measured axial stresses (compressive towards the inner surface and tensile towards the outer) was found in the HAZ of the small pipe, with a superimposed global compressive bending stress (~–55 MPa) probably caused by the repair weld (section 4.3.2). In the large pipe a parabola type profile was obtained for the through-thickness axial stress in the HAZ, which was found to be tensile at the surfaces with a compressive region in the middle (section 4.4.2).
- The radial stress in both pipes was always relatively low with all values close to zero.
- It was also found from a transverse scan measured at 5 mm away from the inner surface in the large pipe that the tensile hoop stress gradually decreased with distance from the weld centre-line and attained a constant value in the HAZ. But the compressive nature of the axial stress was found to increase within the HAZ and far field relaxation was

apparent from the measurements (figure 4.23). In the small pipe all the stresses were found to be tensile at a depth of 2 mm from the outer surface in the weld centre; the high tensile hoop stress decreased through the weld and the HAZ but maintained its tensile nature, whereas the low tensile axial stress changed its sign as it entered into the HAZ (figure 4.14(a)).

- An impressive agreement was found between the measured through-thickness stresses and finite element predictions for the original girth weld beneath the final capping pass (section 4.5).

6.2.2 Effects of Repair Weld

The effects of a repair treatment on the existing stress fields from an original weld, as measured in the small welded pipe are summarised below.

- The repair treatment generated a sharp rise in the axial stress in the HAZ, particularly over the inner half thickness (*i.e.* beyond the repair depth) where the increase was in the order of 300 MPa (figure 4.30).
- The through-thickness hoop stress was generally reduced except near the inner surface. In effect, the axial and hoop stresses became uniformly tensile through the thickness adjacent to the repair weld. No discernible change was noticed in the radial stress (figures 4.30 and 4.13).
- The measured axial stresses in the repair HAZ displayed a membrane character of average tensile magnitude of about 175 MPa (figure 4.13). The presence of this high tensile membrane stress in the repair region and a compressive one (–55 MPa) in the original weld area suggests that the repair treatment caused an overall bending effect on the pipe.
- In the transverse direction the axial stress measured at 2 mm below the outer surface was found to experience a gradual increase from the weld centre-line up to the parent metal, in contrast to a gradual decrease with a change in sign, as observed in the original weld (figure 4.14).

6.3 MICROLEVEL STRESSES IN THE MMC

6.3.1 Effect of Plasticity on Crack Tip Stresses

A number of conclusions can be drawn from the information revealed by the neutron diffraction measurements of the fatigue cracked MMC specimens. They are listed below.

- The shape misfit stresses in the unstretched specimen (which may also be considered as thermal misfit stresses in the absence of any plastic deformation) in the crack opening (longitudinal) direction were calculated to be about +50 MPa in the matrix and about –250 MPa in the reinforcement (figure 5.21).
- 1% plastic deformation in the specimen reduced the thermal misfit stresses almost to zero in both phases (figure 5.21).
- If it is assumed that the thermal and plastic misfit terms are the only contributors to the total shape misfit stress, then it can be inferred that a 1% plastic deformation by a tensile load along the longitudinal direction in this Al-SiC_p MMC produces a plastic misfit stress of ~–50 MPa in the matrix and ~+250 MPa in the reinforcement in the same direction (section 5.3.3).
- No effect of fatigue cracking or elastic loading on the misfit stresses was observed in this study (section 5.3.3).
- Application of an elastic four point bending load caused the stress field to become increasingly tensile in the crack tip region and compressive at the back face of the specimen, particularly in the longitudinal (crack opening) direction (figures 5.13 – 5.16).
- An overall effect of the plasticity was noticed as the measured total stresses in the plastically deformed specimen became less tensile in the matrix and less compressive in the reinforcement compared to the unstretched specimen. This may produce two opposite effects on the performance of the MMC. In the initial stage of fatigue crack propagation when the crack has a small plastic zone, the presence of a compressive stress in the reinforcement may lead to crack arrest. Any reduction in this compressive stress by the plastic deformation may enhance the initial crack growth and thereby may

reduce the overall fatigue life of the material. If subsequent crack growth is considered, however, the removal of the pre-existing net tensile stress in the matrix by the plastic deformation may reduce the plastic zone size in the Paris régime and thereby reduce the rate of fatigue crack growth.

6.3.2 Effect of Heat Treatment on Misfit Stresses

Various points are listed below as a summary of results and conclusions of the experiments performed with the heat treated MMC specimens that were plastically pre-deformed to ~0.33% by four point bending. They include the effects of heat treatment on the misfit stress and also on the macrostress and the total stress.

- A plastic deformation of about 0.33% reduced the misfit stresses by ~35% in both phases (table 5.4).
- No significant change in the stress values (both the macro and micro stresses) was observed before and after the treatment of the plastically deformed specimen in liquid nitrogen (figures A1.7 and 5.31).
- The macrostress in the specimens was relaxed by heat treatment and the relaxation was found to be proportional to the treatment temperature (and time) (table 5.3).
- A linear relation was found between the initial macrostress in the specimen before heat treatment and the magnitude of relaxation in macrostress caused by heat treatment with a negative slope of about –45° (figure 5.33). This suggests that the more the initial macrostress, the more will be the relaxation, irrespective of the nature of the stress.
- The heat treatment of the specimens regenerated the thermal misfit stress, that was initially reduced by the plastic deformation (table 5.5). The regeneration is caused during the cooling of specimens at the end of each heat treatment and therefore depends on the treatment temperature. However, the treatment time also plays an important role in determining the final value of the regenerated misfit stress.

6.4 SUGGESTIONS FOR FUTURE WORK

This study has emphasised several areas of interest in the study of weld residual stresses and the microstresses in a metal matrix composite material, which was influenced by plasticity and heat treatments.

Although an interesting study on the effect of repair weld has been done here for the small pipe, it will be even more exciting to study the similar effects in the ex-service large pipe. This is already in progress; two repair welds (a short and a long) have been put on the pipe and the residual stresses around these repair welds are being measured at ISIS, UK and at Studsvik, Sweden. It will be interesting to have a comparison of these results with the finite element modelling predictions for the repair weld, which is also being developed by British Energy. It is also recommended to measure at more points, particularly in the areas with high stress gradients, so that a full three dimensional stress profile can be generated for both the original weld and the repair weld.

After obtaining a thorough knowledge about the stress fields in and around the original weld and the repair weld at room temperature, further study on the behaviour of these stress fields at an elevated temperature (~500°C) would be very attractive. This may give better information about the residual stress fields in welded pipes during actual service conditions in a power plant. Another interesting study in this area will be an investigation of the behaviour of residual stress fields around a small reheat crack. Once the proposed new facility at ISIS (*i.e.* ENGIN-X with more versatility and better signal to noise ratio than the existing ENGIN spectrometer) is installed, these types of measurements in welded steels, even for greater thickness will be easier.

Regarding the microstresses in the MMC, there is a scope to continue the present work in studying the effect of heat treatments on the macro and misfit stresses at a fatigue crack tip. This will give more information if heat treatment can produce any beneficial effect on the MMC components having small cracks. All these neutron measurement results can be

correlated with the mechanical properties of the material; studies on the tensile properties, fatigue crack growth and microstructures will be useful.

It appeared from this study that there might be a linear correlation between the amount of plastic deformation and the magnitude of the relaxation in misfit stresses in this Al-SiC_p MMC. This can be further investigated by using several specimens after introducing different amounts of known plastic deformation or a single specimen with a variable plasticity (*e.g.* a cold expanded hole) of known magnitude.

APPENDIX I

A1.1 MEASURED STRAINS: HEAT TREATED SPECIMENS

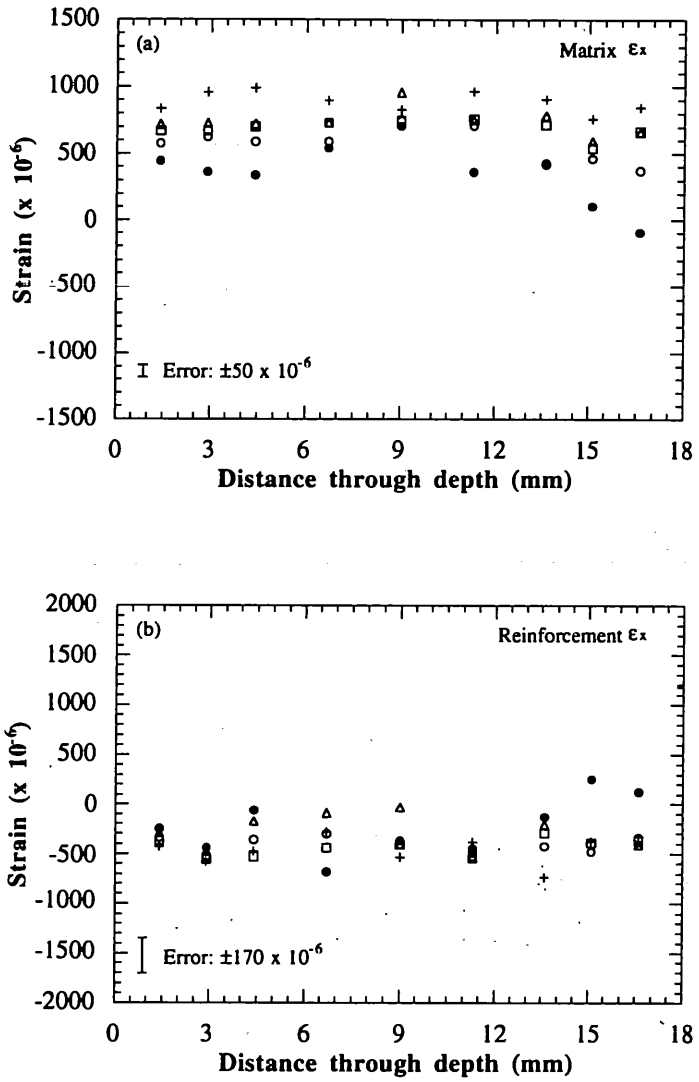

●: as-deformed; ○: 48h @ 180°C; □: 0.5h @ 240°C; △: 2h @ 240°C; +: 0.5h @ 300°C

Figure A1.1: Measured strains in the transverse or *x*-direction in the (a) matrix and (b) reinforcement of as-deformed and heat treated specimens through the depth.

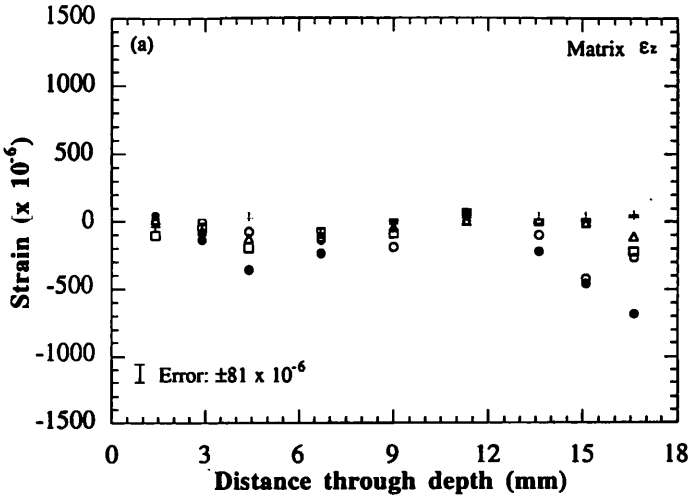

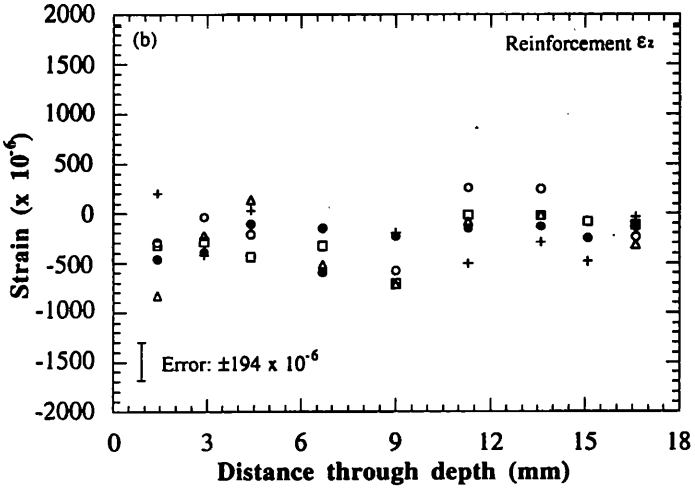

●: as-deformed; ○: 48h @ 180°C; □: 0.5h @ 240°C; △: 2h @ 240°C; +: 0.5h @ 300°C

Figure A1.2: Measured strains in the depth or z-direction in the (a) matrix and (b) reinforcement of as-deformed and heat treated specimens through the depth.

A1.2 CALCULATED STRESSES: HEAT TREATED SPECIMENS

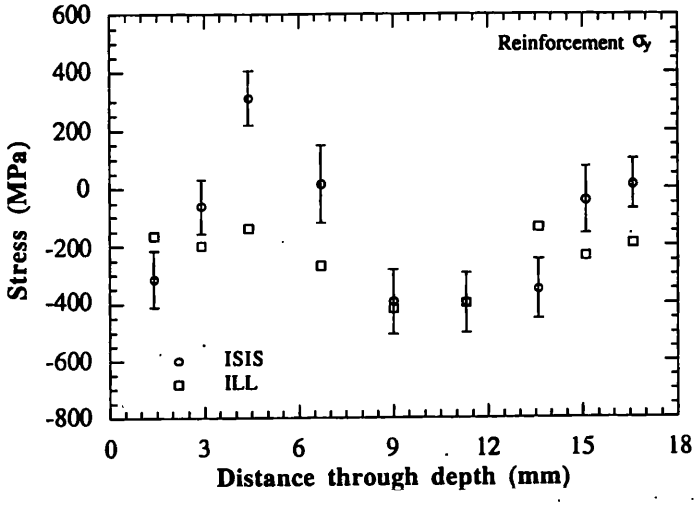

Figure A1.3: Comparison of calculated total stresses in the longitudinal (*y*) direction in the reinforcement of the as-deformed specimen through the depth, measured at ISIS and ILL.

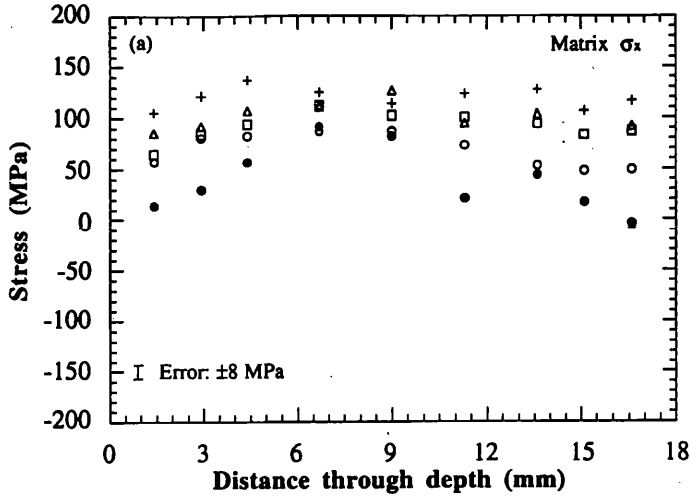

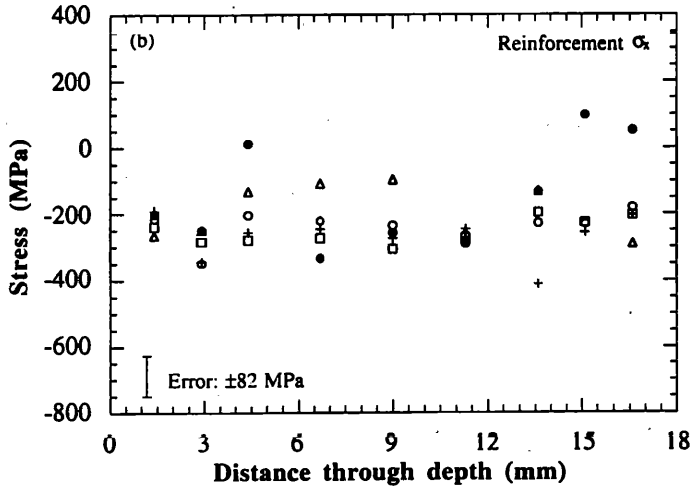

●: as-deformed; ○: 48h @ 180°C; □: 0.5h @ 240°C; ▵: 2h @ 240°C; +: 0.5h @ 300°C

Figure A1.4: Calculated total stresses in the transverse or x-direction in the (a) matrix and (b) reinforcement of as-deformed and heat treated specimens through the depth.

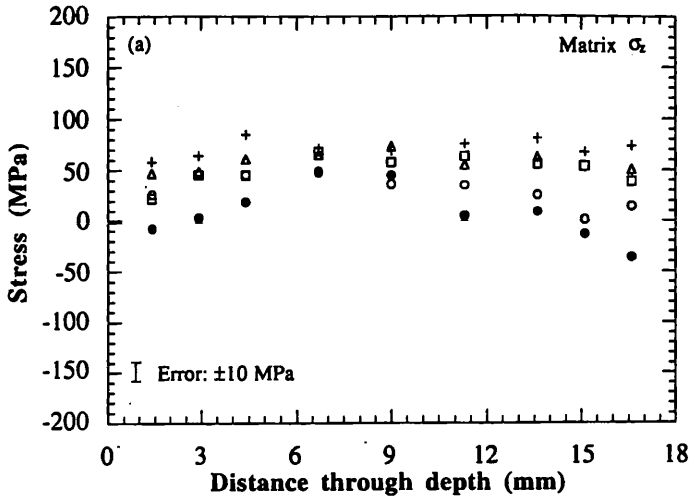

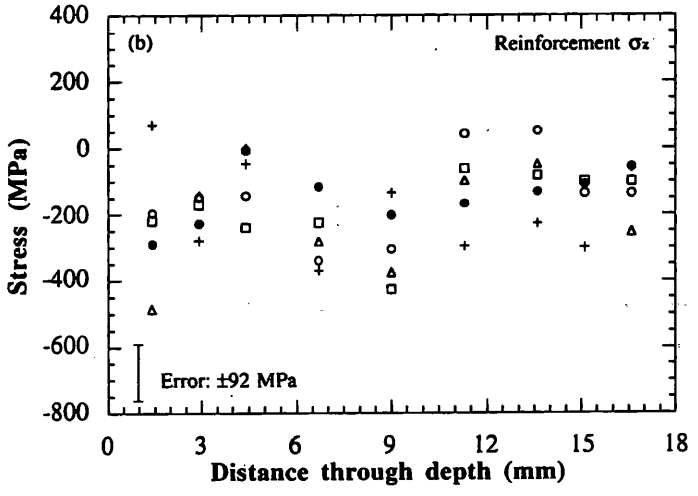

●: as-deformed; ○: 48h @ 180°C; □: 0.5h @ 240°C; △: 2h @ 240°C; +: 0.5h @ 300°C

Figure A1.5: Calculated total stresses in the depth or z-direction in the (a) matrix and (b) reinforcement of as-deformed and heat treated specimens through the depth.

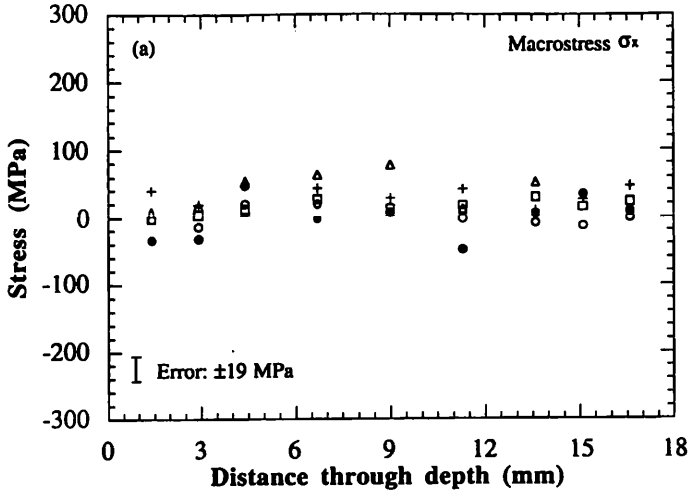

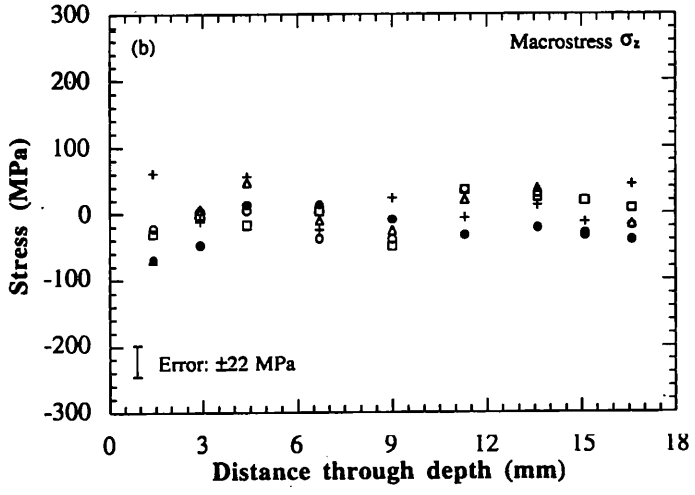

●: as-deformed; ○: 48h @ 180°C; □: 0.5h @ 240°C; △: 2h @ 240°C; +: 0.5h @ 300°C

Figure A1.6: Calculated macrostresses in the (a) transverse or *x*-direction and (b) depth or *z*-direction of as-deformed and heat treated specimens through the depth.

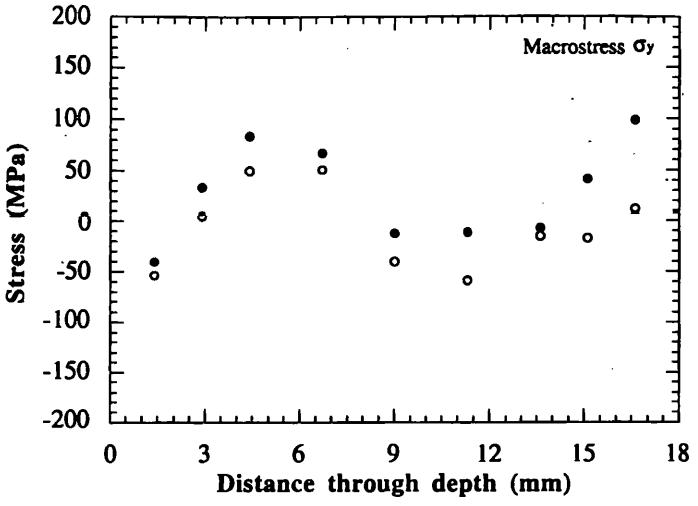

●: as-deformed ○: deformed + treated in liquid N_2

Figure A1.7: Calculated macrostresses through the depth in the longitudinal or *y*-direction in the deformed specimen before (as-deformed) and after the liquid nitrogen treatment. No uncertainty values of fitting results were available from the existing program at ILL; hence no error bars.

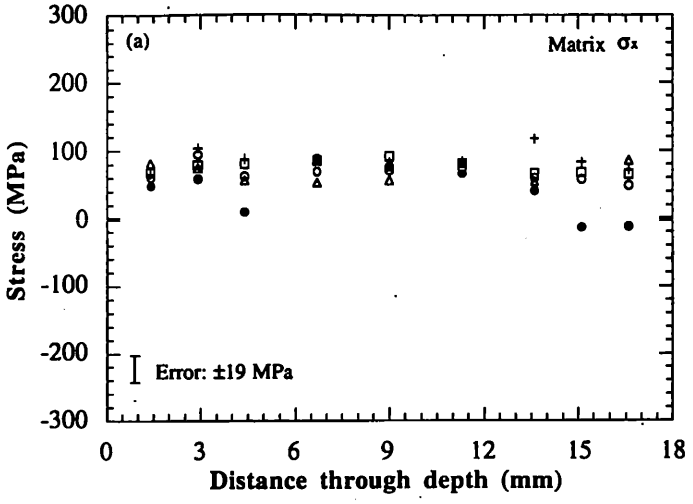

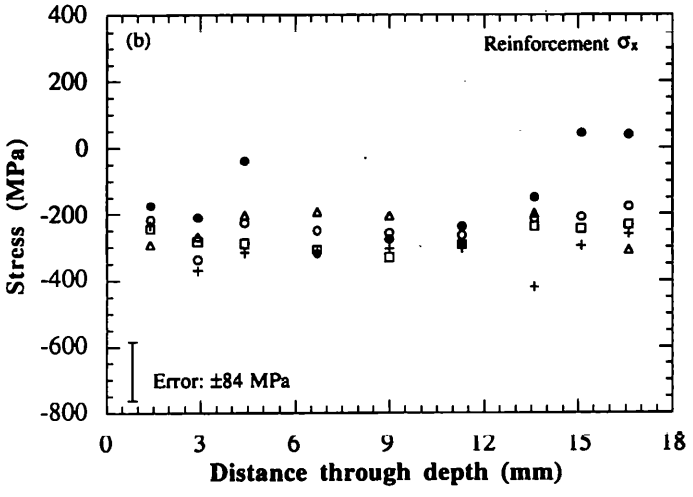

●: as-deformed; ○: 48h @ 180°C; □: 0.5h @ 240°C; △: 2h @ 240°C; +: 0.5h @ 300°C

Figure A1.8: Calculated shape misfit stresses in the transverse or *x*-direction in the (a) matrix and (b) reinforcement of as-deformed and heat treated specimens through the depth.

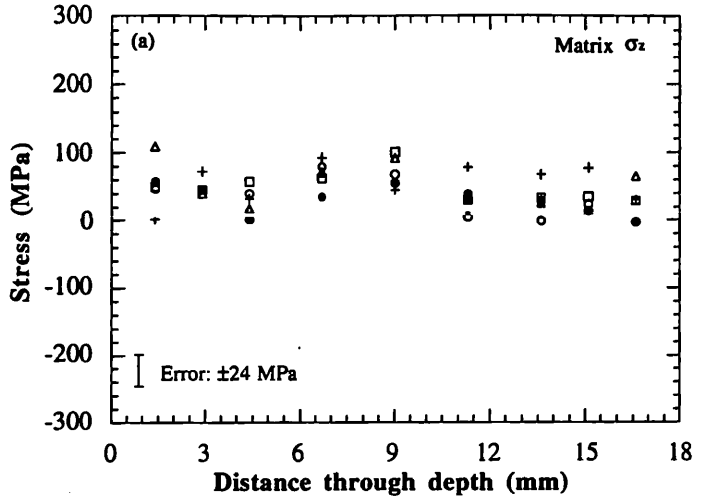

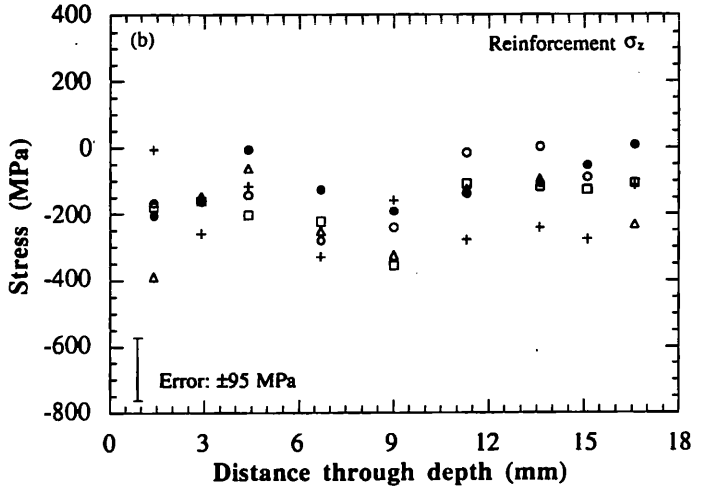

●: as-deformed; ○: 48h @ 180°C; □: 0.5h @ 240°C; △: 2h @ 240°C; +: 0.5h @ 300°C

Figure A1.9: Calculated shape misfit stresses in the depth or z-direction in the (a) matrix and (b) reinforcement of as-deformed and heat treated specimens through the depth.